Liquid Permeability of Ceramic Foam Filters

Kexu Zhang

Liquid Permeability of Ceramic Foam Filters

Kexu Zhang

Supervisor: Prof. Ragnhild E. Aune

Co-Supervisor: Mark W. Kennedy

Norwegian University of Science and Technology

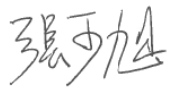Department of Materials Science and Technology

2012

Declaration of Authorship

Jeg erklærer herved at arbeidet har blitt utført selvstendig og i samsvar med "Reglement for Sivilarkitekt- og Sivilingeniøreksamen" ved NTNU.

I hereby declare that this work has been carried out independently and in compliance with the examination regulations of the Norwegian University of Science and Technology, NTNU.

Trondheim, July 2012

Kexu Zhang

Acknowledgements

Trondheim, July 2012

Kexu Zhang

Abstract

This project is in support of the PhD project: 'Removal of Inclusions from Liquid Aluminium using Electromagnetically Modified Filtration'. The purpose of the present project was to measure the tortuosity and permeability of ~50 mm thick 30, 40, 50 and 80 pores per inch (ppi) commercial alumina Ceramic Foam Filters (CFFs). Measurements have been taken of the cell (pore), the window and strut sizes, as well as the porosity, tortuosity and liquid permeability. Water velocities from ~0.015-0.77 m/s have been used to derive both the first order (Darcy) and the second order (Non-Darcy) terms for use with the Forchheimer equation. Experiments were made using 49 *mm* diameter 'straight through' and 101 *mm* diameter 'expanding flow field' designs. Experimental data are compared with simulation results made using COMSOL 4.2a$^{®}$ 2D axial symmetric Finite Element Modelling (FEM). Permeability results are correlated using directly measurable parameters. Development of improved wall sealing (49 *mm*) and elimination of wall effects (101 *mm*), has lead to a high level of agreement between experimental, analytical and FEM methods ($\pm$0-7% on predicted pressure drop) for both types of experiments. The liquid permeability experiments were also used to determine the variability of permeability between different filters of the same ppi, and permeability variation within the same CFF for changes position. Tortuosity has been determined by two inductive methods, one using cold solidified samples at 60 *kHz* and the other using liquid metal at 50 *Hz*, giving comparable results.

Contents

Chapter 1

Introduction

Ceramic Foam Filters (CFFs) have been used commercially in the foundry industry for more than four decades for the production of premium quality aluminium castings for use in such applications as in the aerospace industry.[1] In recent years, CFFs have become more important in the physical purification of metals, for the ferrous and nonferrous industries. The nonferrous industry uses the largest amount of this filtering media, especially the aluminium casting industry. In 1992, Aubrey and Dore[2] reported that eight million metric tons of aluminium was filtered using CFFs, and this means that about 50 percent of all the aluminium produced in the world in that year, was purified through this filtering media. High-temperature alloys also use CFFs. Sutton[3] announced results on the filtration of super-alloys in 1985. In 1993, Garing and Cummings reported the successful filtration of carbon and alloy steels using CFFs.[4] Porous ceramics are now widely applied as materials for filtration of fluid in high-temperature applications.[5,6,7]

It is widely accepted that based on their structural properties, CFFs can remove exogenous and indigenous inclusions in the melts,[8] and moreover, have low flow resistance and high filtration efficiency for particles over 10-20 microns.[9] The structure of the CFF creates a unique, tortuous path for the fluid to flow, which captures inclusions and allows clean, smooth-flowing metal to exit into the mould cavity.[10] CFFs are generally accepted as the best filters for casting. Their main advantages are: high filtration efficiency, turbulence reduction, refractoriness, and erosion resistance, for the most demanding casting applications.[11]

Permeability is an important parameter for the characterization of CFFs, since it is required to predict the flow rate obtainable under a given pressure drop or to be able to predict the pressure drop necessary to achieve a specific flow rate. The relationship between these quantities can be expressed as a function of the fluid flow, and medium properties and is obtained by fitting the experimental data with permeability equations. [12,13]

Chapter 2

Theoretical Background

2.1 CFF

Cellular structures can be found in natural materials, such like wood, bone, coral, etc., significantly, nature has optimized certain mechanical properties, for example: stiffness, strength and mass, in an efficient manner.[14] About 50 years ago, the development of synthetic materials manufacturing methods inspired investigation into the structure and properties of cellular materials.[15,16] For ceramic foam, their good thermal resistance and high porosity characteristics led to use as filters in the purification of liquid metals, which are still the largest application today. Ceramic foam is also used for catalytic combustion, burner enhancers, soot filters for diesel engine exhausts, catalyst supports, and biomedical devices.[17,18,19,20]

It is widely accepted that based on their structural properties, CFFs can remove exogenous and indigenous inclusions in the melts,[21] and moreover, to have low flow resistance and high filtration efficiency.[9] The *Figure.1* shows a ceramic foam filter and bowl for use in the removal of solid inclusions from liquid metal. The filters are integrated into filter boxes and applied to the casting process directly in front of the casting unit.
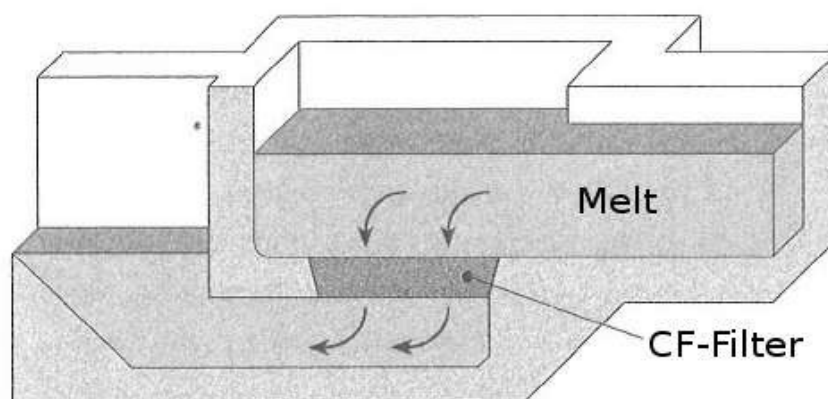
Figure.1 CFF and filter bowl.[22]

The type of filtration occurring in a CFF can be divided into deep bed, cake or mixed filtration. The efficiency is dependent on the pores ppi (pores per inch) of the filter material, as shown in *Figure.2*[23] and also on the size distribution of the particulates to be removed. The

2

ppi refers to the plastic material used to make the ceramic foam and is found from the average number of pore boundaries encountered per inch.[24] More recently the CFFs are 'graded' into different ppi categories according to air permeability.[25] In *Figure.2*, the line between each column of filtration efficiency ranges marks the mean efficiency.
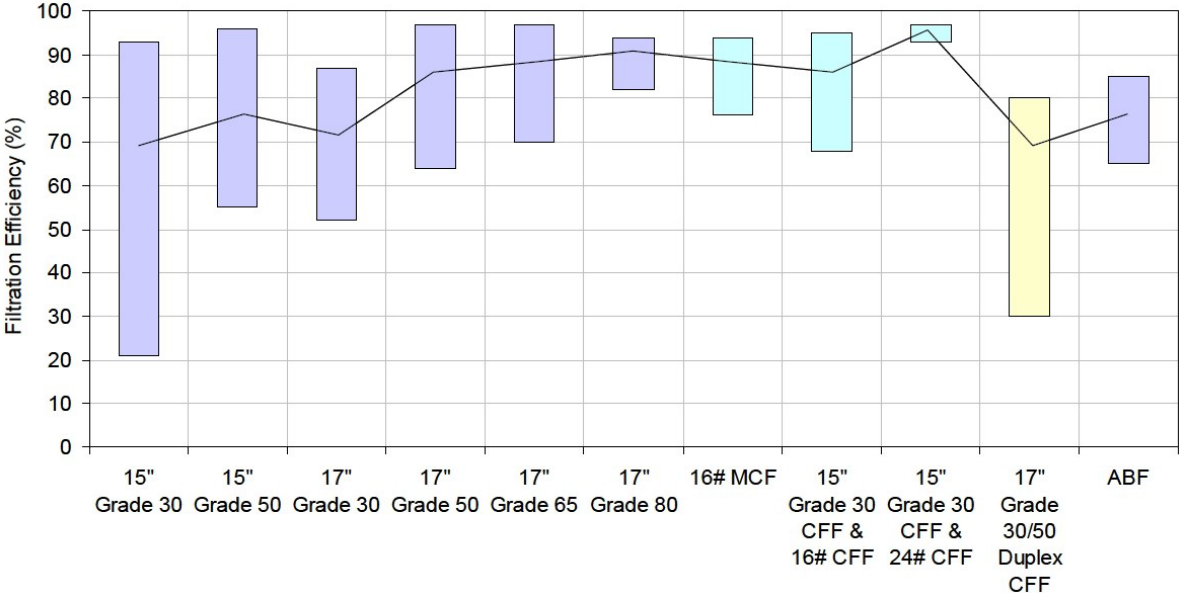
Figure.2 Relative performance of different inline filtration systems measured by the N15 LiMCA.

The size ranges of typical commercial CFFs are 10 to 80 ppi (see *Figure.3*). 20-40 ppi are the most commonly used,[26] for industrial cast houses to reach both the desired casting rate and achieve minimally acceptable filtration efficiency. The 10 to 20 ppi filters have poor particle retention, and are often used for filtration of entrapped bulk, surface borne oxides and other large particulates generated during melting, holding and transport. High pore density filters with 60-80 ppi are only useful for quality sensitive applications, such as surface critical extrusion and sheet products.[27]
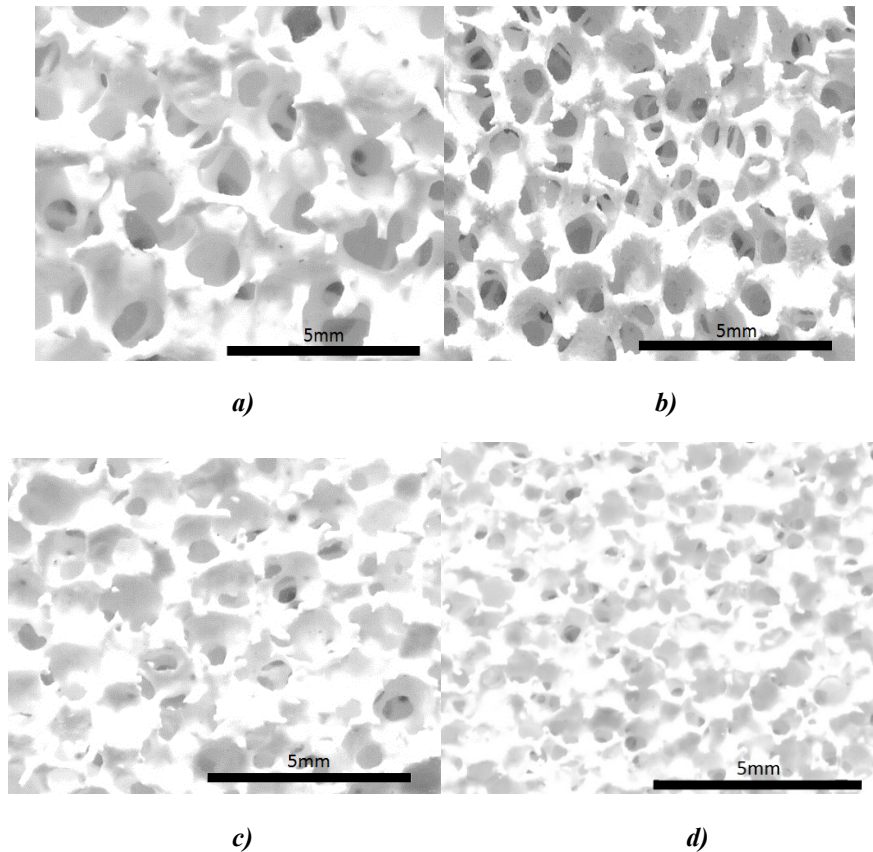
Figure.3 Sivex® CFFs a) 30 ppi, b) 40 ppi, c) 50 ppi, d) 80 ppi.

The structure of the CFF creates a unique, tortuous path for the fluid to flow, which captures inclusions and allows clean, smooth-flowing metal to exit into the mould cavity.[27] The important filter parameters are effective porosity (i.e., the porosity that effectively contributes to the fluid flow), tortuosity, specific surface area and pore diameter.[28] The filtration process is also dependent on: the alloy type, grain refiner, casting rate, metal temperature, etc.[29] Grain refiner added before the filters has a particularly negative impact on filtration efficiency. CFFs are generally accepted as the 'best' filters for casting based on cost, ease of use and acceptable performance characteristics. Their main advantages are: high filtration efficiency, turbulence reduction, refractoriness, and erosion resistance, for the most demanding casting applications. Deep bed particle filters have generally better filtration performance, but are more difficult and costly to operate.

The CFFs used for this research are commercial high alumina filters produced by SIVEX®. The chemical composition of the CFF is mainly alumina (the exact composition is proprietary commercial information), which was phosphate bonded, as indicated in *Figure.4*. **Table I** shows the detailed composition of the alumina CFFs produced by Jiangxi Jintai Special Material Co., Ltd, which are taken as indicative of the alumina CFF material used in this study.   It should be noted that the carbon in *Figure.4* can be ignored, since it originates from the conductive carbon coating added to the sample before analysis. The porosity of the filter is around 85 to 90%. The ceramic particle density is 3.48 ± 0.02 g/cm^3, based on private communication with Norsk Hydro.
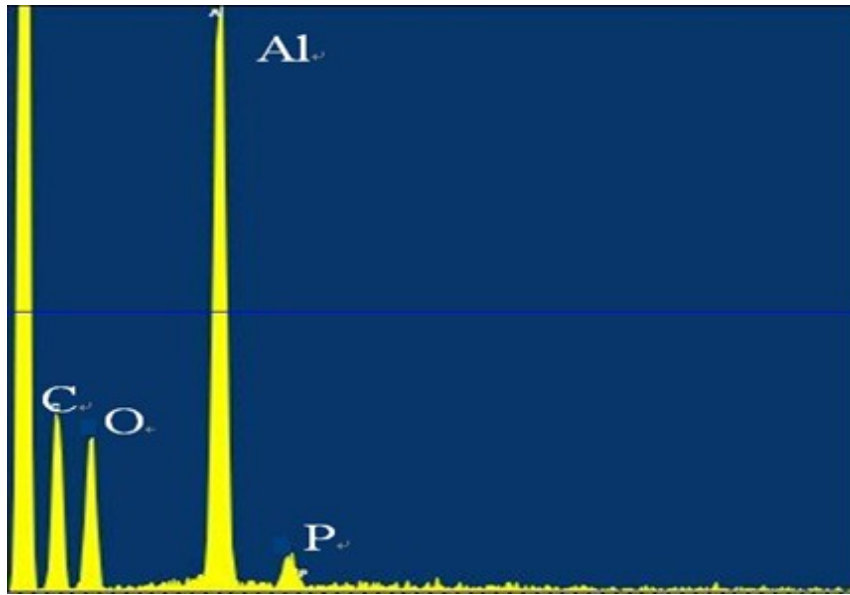
Figure.4 Electron Probe Micro Analysis(EPMA) of CFFs.

Table I Chemical composition for Ceramic Foam Filters (CFF) made from alumina.[30]

Al2O3	SiC	SiO2	ZrO2	Others
80~82%	---	5~6%	---	12~15%

* Others are assumed to be mainly Phosphate (P_2O_5) binders

2.2 Permeability

Permeability is an important parameter for the characterization of CFFs, since it is required to predict the flow rate obtainable under a given pressure drop or to be able to predict the pressure drop necessary to achieve a specific flow rate. The relationship between these quantities can be expressed as a function of the fluid flow, and medium properties and is obtained by fitting the experimental data with permeability equations. [31,32]

There are two main equations used in the literature to represent the permeability of CFFs, Darcy's law and Forchheimer's equation.

Darcy's law[33] is shown as follows:

$$q = \frac{-k_1}{\mu} \nabla P \qquad (1)$$

5

Where q is the flux or discharge per unit area, with units of length per time, [m/s], k_1 is the Darcian permeability constant [m^2], μ is the fluid dynamic viscosity [Pa·s] and ∇P is the pressure gradient vector [Pa/m], ΔP is pressure drop [Pa].

The Darcy's law only accurately describes the pressure flow relationship at low fluid velocities, and becomes increasingly inaccurate at high velocities (i.e. turbulent Reynolds numbers).[34] At high velocity, Forchheimer's equation has been reliably employed in the literature to predict the pressure flow relationship of ceramic filters in a broader velocity range.[35] For an incompressible fluid and a rigid, homogeneous (i.e. isotropic) ceramic filter, Forchheimer's equation can be represented as follows[36]:

$$\frac{\Delta P}{L} = \frac{\mu}{k_1} V_s + \frac{\rho}{k_2} V_s^2 \qquad (2)$$

Where ΔP is pressure drop [Pa], L is the filter thickness [m], μ is the fluid dynamic viscosity [Pa·s], ρ is the fluid density [kg/m^3], the constants k_1 and k_2 are called the Darcian and non-Darcian permeability coefficients respectively and V_s is the superficial fluid velocity [m/s].

The term $\Delta P / L$ is a 'normalised' pressure drop per unit length, i.e. the pressure gradient (see Equation (3)). This assumes a pressure gradient in only one axis, which is essentially true for the 'straight through' design and not strictly true for the 'expanding flow field design', which experiences gradients in both the z and r-axes.

$$\nabla P = \frac{\Delta P}{L} \qquad (3)$$

The term $\mu V_s / k_1$ represents the contribution to flow resistance due to friction between fluid layers and the pore walls (i.e. the viscous loss term). The term $\rho V_s / k_2$ represents the contributions of inertia and turbulence.[32, 37]

One publication[34] reported that computation of k_1 and k_2 using Forchheimer's equation generally worsens when less data are included in the velocity curve, particularly at low flow velocities. The Darcian permeability constant k_1 then varies more than the non-Darcian permeability constant k_2. This is likely due to the effect of the high pressure gradients at higher velocities dominating the output of the regression techniques implemented by the previous investigators.

In 1952, Ergun[38] proposed expressions to describe k_1 and k_2 as follows:

$$k_1 = \frac{\varepsilon^3 d_p^2}{150(1-\varepsilon)^2} \tag{4}$$

$$k_2 = \frac{\varepsilon^3 d_p}{1.75(1-\varepsilon)} \tag{5}$$

Where ε is the fractional porosity [unitless], and d_p is the mean particle diameter of the foam filter [m].

Forchheimer's equation can be modified using the terms of Ergun:

$$\frac{\Delta P}{L} = 150 \frac{(1-\varepsilon)^2 \mu}{\varepsilon^3 d_p^2} V_s + 1.75 \frac{(1-\varepsilon)\rho}{\varepsilon^3 d_p} V_s^2 \tag{6}$$

Although d_p is not ambiguous as a parameter, Ergun's equation was derived for packed beds of solids and there is no precise way to assign a value to this variable for a porous filter media. The major challenge to the application of these equations to a porous media is therefore to define an equivalent mean particle diameter. It is possible to apply the Ergun formula using alternately: the cell (d_c), window (d_w) or strut (d_s) diameters. These diameters are indicated in *Figure.5*. Several attempts have been presented in the literature trying to replace the particle size and possibly the most obvious trial is the use of the pore or cell diameter (d_c)[9,39,40,41], which is usually determined by examining enlarged photographs of cross-sections of foam samples.

Several investigators[41] have indicated that the use of Ergun's equation yields errors in the prediction of permeability of ceramic foams as high as 50%, while the introduction of window size obtained by image analysis into the same equations, seems to give more reasonable results to assess the permeability of ceramic filters.
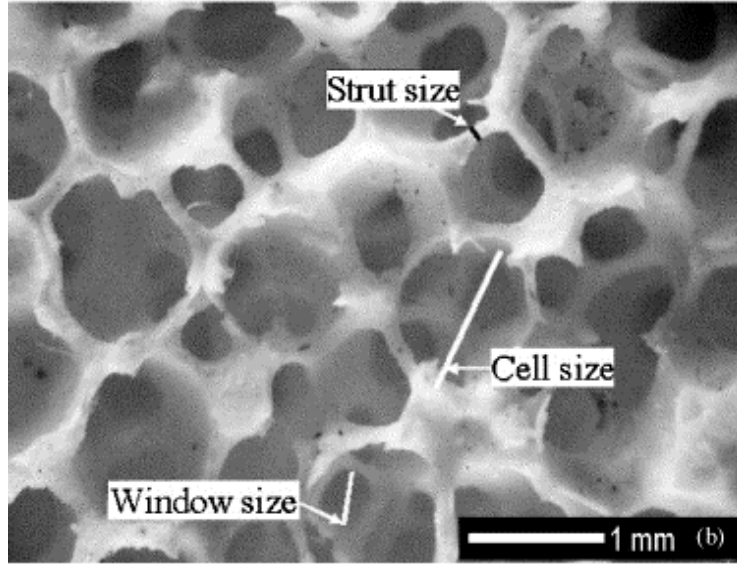
Figure.5 Definition of CFF: cell, window and strut diameters.[42]

Ergun defined the 'equivalent' particle diameter of a non-spherical solid (d_p) as the diameter of the sphere having the same 'outer' specific surface area per unit solid volume (S_v) of the actual material in question (internal porosity, and small projections or cavities were ignored)[38]:

$$d_p = \frac{6}{S_v} \qquad (7)$$

In Equation (7) the nomenclature of Ergun is maintained. There is some confusion in recent literature, where S_v is used to represent the surface area of solid per unit bed volume (i.e. S_B). Equation (6) can be rewritten using Equation (7) as:

$$\frac{\Delta P}{L} = 4.17 \frac{S_v^2 (1-\varepsilon)^2 \mu}{\varepsilon^3} V_s + 0.292 \frac{S_v (1-\varepsilon)\rho}{\varepsilon^3 d_p} V_s^2 \qquad (8)$$

Richardson[24] explored the relationship between S_v and d_w for porous ceramics and suggested applying the hydraulic diameter (d_h) concept. They equated the hydraulic diameter to the measured window diameter:

$$d_w = d_h = 4 \frac{wetted - area}{wetted - perimeter} \qquad (9)$$

Assuming all the pores have the same hydrodynamic diameter, a simple geometric analysis yields:

$$S_v = \frac{4\varepsilon}{d_w(1-\varepsilon)} \qquad (10)$$

Substituting Equation (10) into Equation (8) yields:

$$\frac{\Delta P}{L} = 66.7\frac{\mu V_s}{\varepsilon d_w^2} + 1.17\frac{\rho V_s^2}{\varepsilon^2 d_w} \qquad (11)$$

Recently Dietrich[43,44] proposed the following equation after correlating 2500 separate experimental values from 20 authors:

$$\frac{\Delta P}{L} = 110\frac{\mu V_s}{\varepsilon d_h^2} + 1.45\frac{\rho V_s^2}{\varepsilon^2 d_h} \qquad (12)$$

The Equation (11) and (12) are obviously similar. If one assumes that the hydraulic diameter in Equation (12) is equal to the window diameter, as both empirical constants in Equation (12) are larger than those in Equation (11), it will yield higher estimated pressure drops for any velocity. Equation (12) has recently been independently shown to give excellent results using the optically determined hydraulic diameter, i.e. the equivalent circular window diameter, (d_w).[45]

Other published correlations are all present in **Table II**

Table II Pervious published correlations.[46]

Reference	Pressure drop on foams correlation proposed	
J.T. Richardsom et al.	$\frac{\Delta P}{L} = \frac{\alpha S_v^2 \mu(1-\varepsilon)^2}{\varepsilon^3}V_s + \frac{\beta S_v \rho(1-\varepsilon)}{\varepsilon^3}V_s^2$	; $S_v = \frac{12.979[1-0.971(1-\varepsilon)^{0.5}]}{d_w(1-\varepsilon)^{0.5}}$
	$\alpha = 9.73\times10^2 d_w^{0.743}(1-\varepsilon)^{-0.0982}$	; $\beta = 3.68\times10^2 d_w^{-0.7523}(1-\varepsilon)^{0.07158}$
J.F. Liu et al.	$\frac{\Delta P}{L} = \frac{22(1-\varepsilon)\mu}{\varepsilon^3 D_p^2}V_s + \frac{0.22(1-\varepsilon)\rho}{\varepsilon^3 D_p}V_s^2$	; $D_p = 1.5 d_w \frac{1-\varepsilon}{\varepsilon}$ D_p=equivalent spherical diameter
E.A. Moreira et al.	$\frac{\Delta P}{L} = 1.275\times10^9 \frac{(1-\varepsilon)^2 \mu}{\varepsilon^3 d_w^{-0.05}}V_s + 1.89\times10^4 \frac{(1-\varepsilon)\rho}{\varepsilon^3 d_w^{-0.25}}V_s^2$	
T.J. Lu et al.	$\Delta P = [0.044 + \frac{0.008(d_c/d_s)}{(d_c/d_s-1)^{0.43+1.13(d_s/d_c)}}]\mathrm{Re}^{-0.15}$	; $\mathrm{Re} = \frac{\rho d_s(V_s/1-d_s/d_c)}{\mu}$
L. Tadrist et al.	$\frac{\Delta P}{L} = \alpha \frac{(1-\varepsilon)^2}{\varepsilon^3 d_s^2}\mu V_s + \beta\frac{(1-\varepsilon)}{\varepsilon^3 d_s}\rho V_s^2$	; $100 \le \alpha \le 865, 0.65 \le \beta \le 2.6$
M.D.M Innocentini et al.	$\frac{\Delta P}{L} = 150\frac{(1-\varepsilon)^2 \mu}{\varepsilon^3 d_p^2}V_s + 1.75\frac{(1-\varepsilon)\rho}{\varepsilon^3 d_p}V_s^2$	; $d_p = 1.5\frac{1-\varepsilon}{\varepsilon}d_c$
M. Lacroix et al.	$\frac{\Delta P}{L} = 150\frac{(1-\varepsilon)^2 \mu}{\varepsilon^3 d_p^2}V_s + 1.75\frac{(1-\varepsilon)\rho}{\varepsilon^3 d_p}V_s^2$	; $d_p = 1.5 d_s$

9

2.3 Fluid Mechanics

2.3.1 Viscosity

Viscosity is that property of a fluid by virtue of which it offers resistance to shear.[47] Newton's law (Equation (13)) gives the relationship between shear stress and viscosity.

$$\tau = \mu \frac{du}{dy} \qquad (13)$$

Where τ is the shear stress [Pa], μ is viscosity [Pa·s], and du/dy is the velocity gradient [s^{-1}].

For a given velocity gradient, the shear stress is directly proportional to the viscosity. In everyday terms (and for fluids only), viscosity can be considered 'thickness' or 'internal friction'. Thus, water is 'thin', having a lower viscosity, while honey is 'thick', having a higher viscosity. Put simply, the less viscous the fluid is, the greater its ease of movement (fluidity).[48]

The viscosity of a liquid decreases with temperature, but the viscosity of a gas increases with temperature. This can be explained by examining the causes of viscosity. The fluid's resistance to shear depends on fluid's rate of transfer of molecular momentum and its cohesion. Liquid has cohesive forces much larger than a gas, since liquid molecules are much more closely spaced than in a gas. Therefore, cohesion will be the predominant cause of viscosity in a liquid, so viscosity will decreases with temperature like cohesion, and also be independent of pressure (except at very high pressure).[49]

Viscosity coefficients can be defined in two ways: dynamic and kinematic viscosity. Dynamic viscosity μ, is also called the absolute viscosity, and the typical unit is *Pa·s*. Kinematic viscosity v, is the ratio of viscosity to mass density[47], and the typical unit is [m^2/s]:

$$v = \frac{\mu}{\rho} \qquad (14)$$

2.3.2 Reynolds Number

In fluid mechanics, the Reynolds number (Re) is a dimensionless number that gives a measure of the ratio of inertial forces to viscous forces and consequently quantifies the relative importance of these two types of forces for given flow conditions.[50] The concept was

introduced by George Gabriel Stokes in 1851[51], but the Reynolds number is named after Osborne Reynolds, who popularized its use in 1883.[52]

Since the Reynolds number expresses the ratio of inertial forces to viscous forces, so:

$$\mathrm{Re} = \frac{InertiaForce}{ViscousForce} \qquad (15)$$

$$\mathrm{Re} = \frac{\rho V \dfrac{dV}{dx}}{\mu \dfrac{d^2V}{dx^2}} \qquad (16)$$

$$\mathrm{Re} = \frac{\rho VL}{\mu} = \frac{VL}{v} \qquad (17)$$

Where Re is Reynolds number, V is the mean velocity of the fluid relative to an object like a pipe, a particle or a pore [m/s], L is a characteristic linear dimension, (e.g. pipe, particle or pore diameter) [m], μ is the dynamic viscosity of the fluid [Pa·s or N·s/m² or kg/(m·s)], v is the kinematic viscosity [m²/s] (see Equation (14)), and ρ is the density of the fluid [kg/m³].

For flow in a pipe or tube, the Reynolds number is generally defined as[53]:

$$\mathrm{Re} = \frac{\rho V d_h}{\mu} = \frac{V d_h}{v} = \frac{Q d_h}{vA} \qquad (18)$$

Where d_h is the hydraulic diameter of the pipe [m], Q is the volumetric flow rate [m³/s], and A is the pipe cross-sectional area [m²].

Reynolds numbers are used frequently to characterize different flow regimes, such as laminar or turbulent flow. *Figure.6* shows the area of different flow regimes. At low Reynolds numbers, Re<2300, it is laminar flow, viscous forces are dominant, and characters are smooth and constant fluid motion. Turbulent flow occurs at high Reynolds numbers, e.g. Re>4000, inertial forces are dominant, tend to produce chaotic eddies, vortices and other flow instabilities.[47,54] When 2300 < Re < 4000, the flow is called "transitional". Transitional flow is a mixture of laminar and turbulent flow, with turbulence in the centre of the pipe, and laminar flow near the edges. Each of these flows behaves in different manners in terms of their frictional energy loss while flowing, and have different equations that predict their behaviour.[55] *Figure.7* shows the diagrammatic sketch of laminar and turbulent flow.
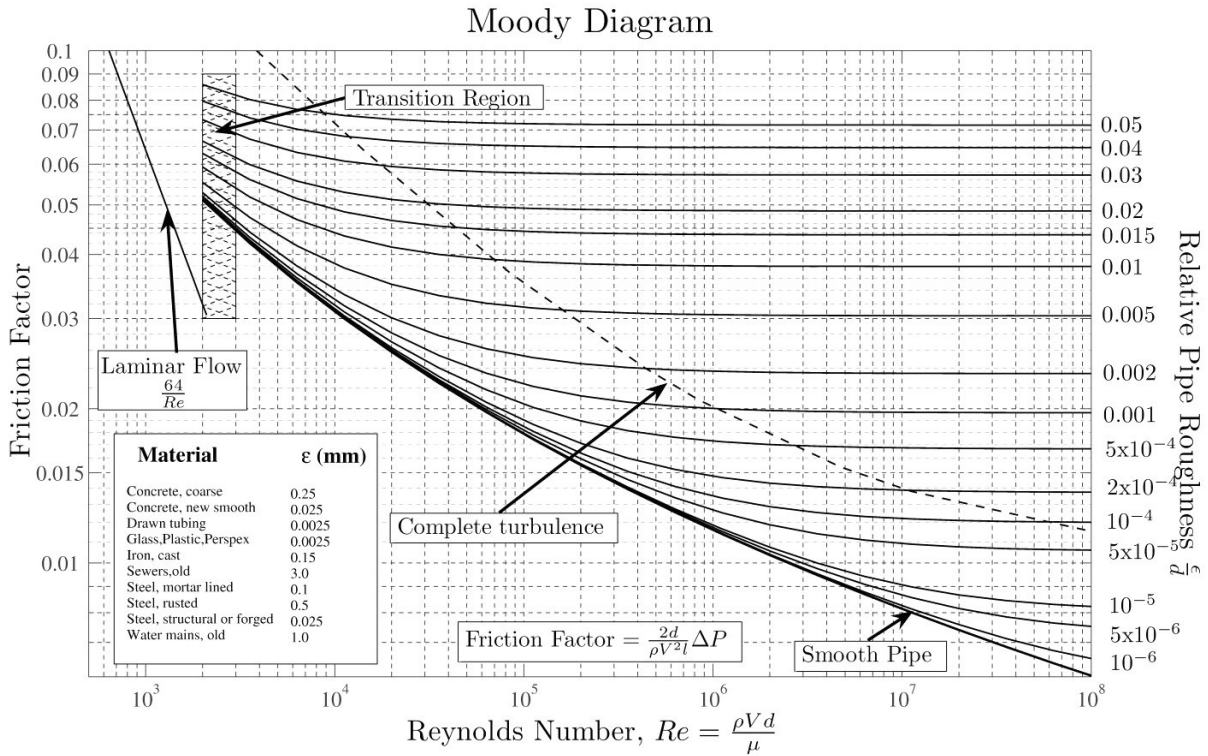
Figure.6 Moody diagram.[56]
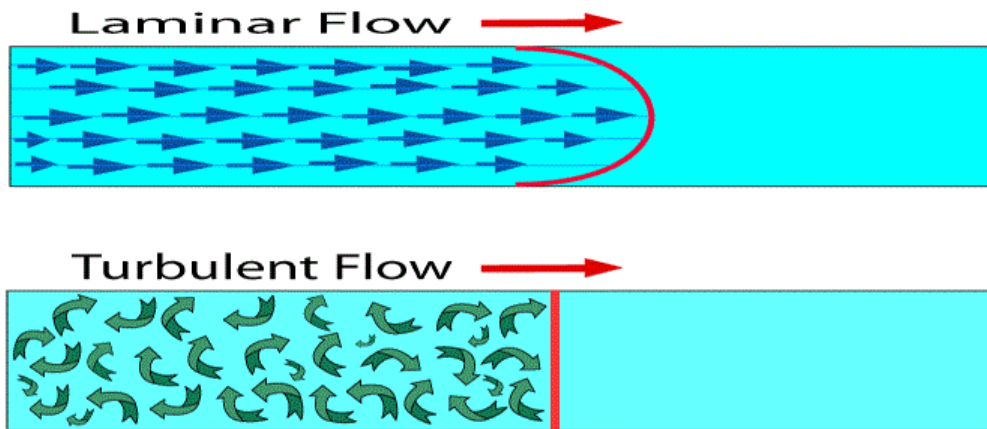
Figure.7—Diagrammatic sketch of laminar flow and turbulent flow.[57]

2.3.3 Entrance Length

A fluid requires some length to develop the velocity profile after entering the pipe or after passing through components such as: bends, valves, pumps, turbines or similar.[58] At a finite distance from the entrance, the boundary layers merge and the in-viscid core disappears. The tube flow is then entirely viscous, and the axial velocity adjusts slightly further until at $x=l_e$ (i.e. the length to fully develop the velocity profile), it no longer changes with x (typically 99% approach is assumed), and the velocity profile is fully developed and constant, the wall shear is constant, and the pressure drops linearly with x, for either laminar or turbulent flow.[59]

These details are shown in *Figure.8*.
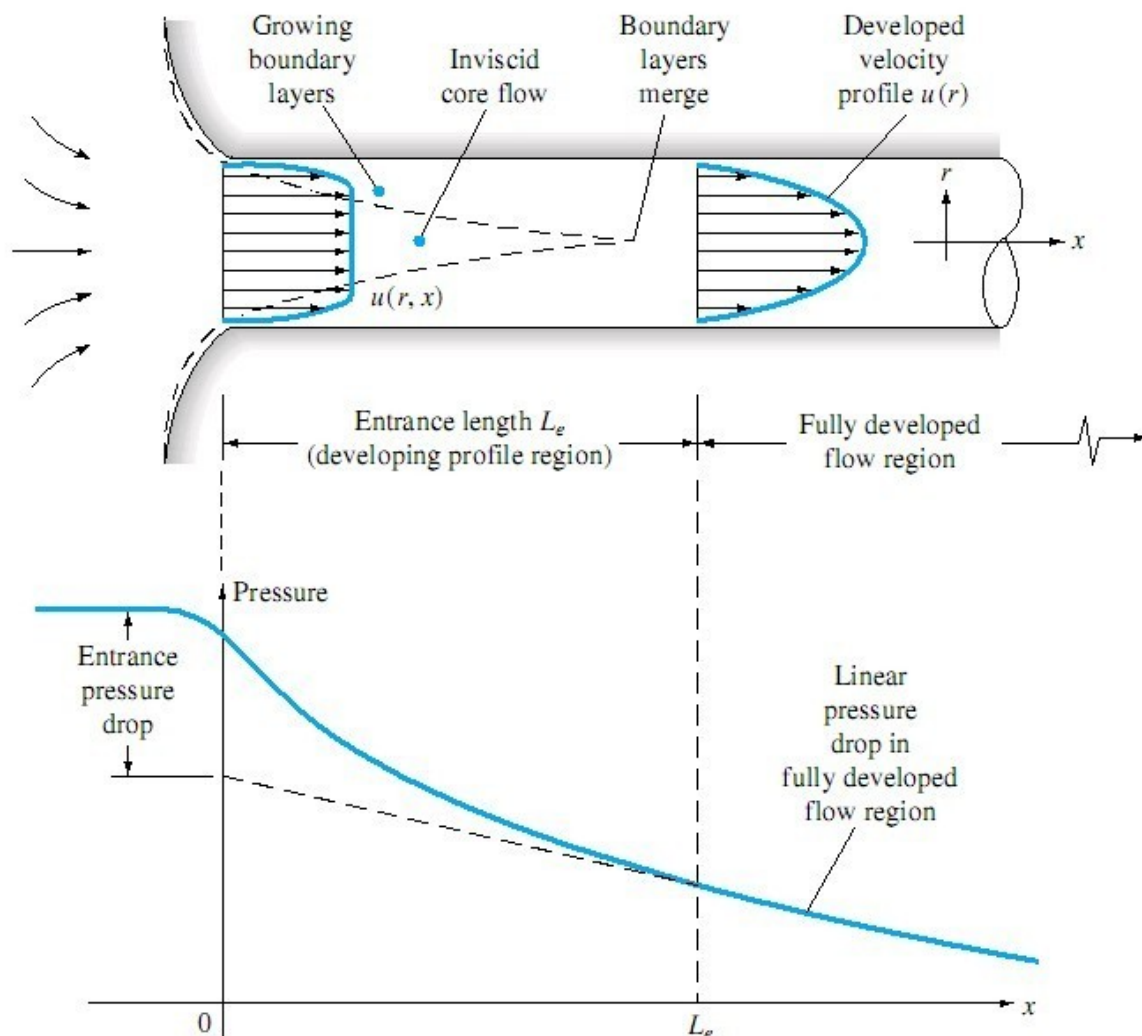
Figure.8—Diagrammatic sketch of developing velocity profiles and pressure changes in the entrance of a duct flow. [53]

The entrance length can be expressed with the dimensionless entrance lengths number expressed as[58]:

$$EL = l_e / d \qquad\qquad (19)$$

Where *EL* is entrance length number, l_e is the length to fully develop the velocity profile [m] and *d* is the pipe diameter [m].

Dimensional analysis shows that the Reynolds number is the only parameter affecting entrance length[59].

13

$$l_e = f(d, V, \rho, \mu) \qquad (20)$$

$$\frac{l_e}{d} = g(\frac{\rho v d}{\mu}) \qquad (21)$$

Substitution of Equation (17) in Equation (21) finally gives,

$$\frac{l_e}{d} = g(\text{Re}) \qquad (22)$$

The entrance length number correlation with the Reynolds number for laminar flow is[60]:

$$EL_{laminar} \approx 0.03\, Re_{pipe} \qquad (23)$$

For turbulent flow one commonly accepted correlation is[61]:

$$EL_{turbulent} = 1.3590\, \text{Re}^{1/4} \qquad (24)$$

2.4 Tortuosity

The tortuosity is typically described as the ratio between the real length of the fluid's path and the actual geometrical length of the sample,[62] as shown in *Figure.9*.
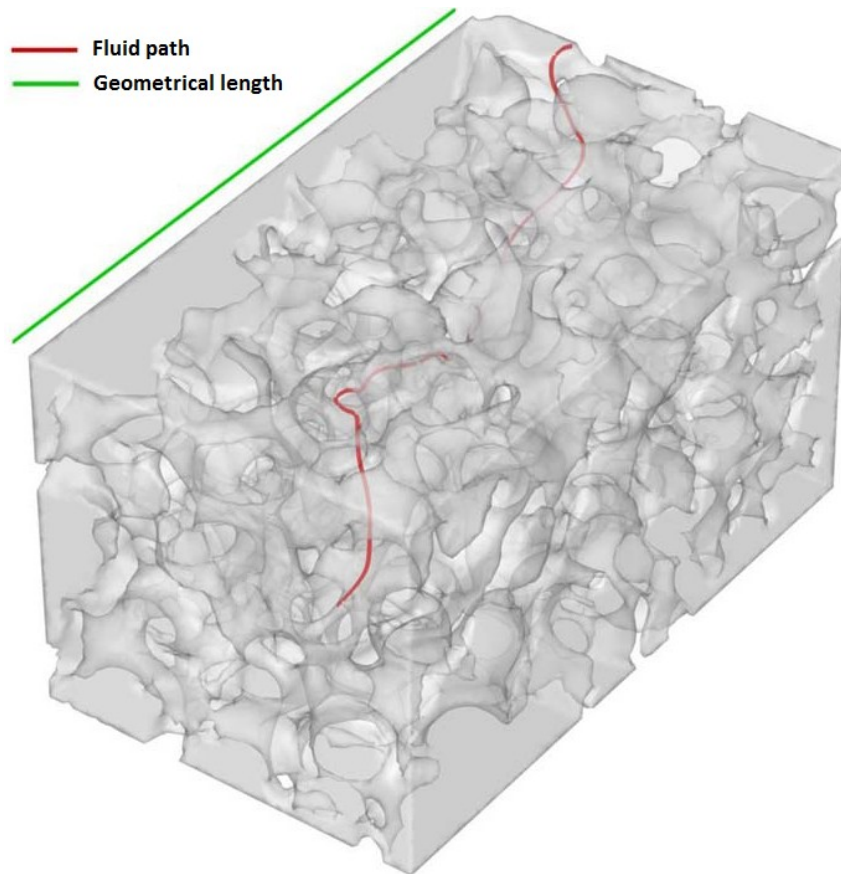
Figure.9 Determination of tortuosity: fluid path and geometrical length.[63]

Figure.10 illustrates porous structures with different flow tortuosities: if both structures have the same volumetric flow rate and porosity, then the residence time of fluid is also identical in both cases. Since the residence time is same and the flow through the 'left' structure passes a significantly longer path, so the structure on the left side has a higher velocity compare to the structure on the right side and all else being equal will exhibit a higher pressure gradient for the same bulk flow.[63] Depending mainly on the pores geometry and not on the contribution of diffusion mechanisms, tortuosity of a low porosity matrix tends to be high and vice versa. The porous solids with high connectivity, should have low tortuosities and vice versa.[64]
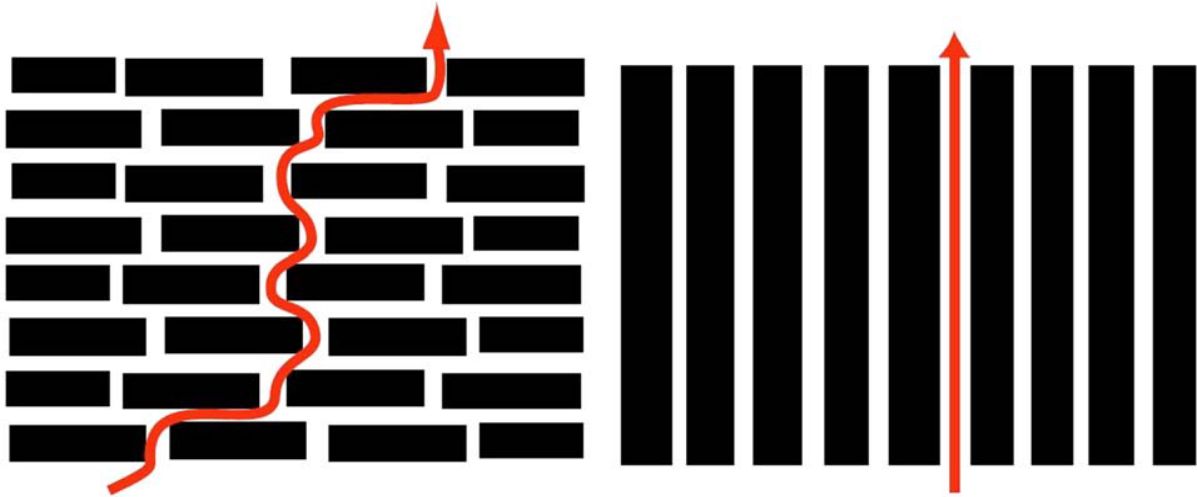
Figure.10 Porous structures with different flow toruosities.[63]

Scheidegger[65] suggested that the tortuosity in sponge structures can be obtained by measuring the electrical resistivity of the structure completely saturated with a conductive solution.

Thus tortuosity can be determined by electromagnetic induction experiments using alloys of known electrical conductivity (σ). The actual resistance of a filter element filled with metal, as shown in *Figure.11* can be compared to the known resistance of an equivalent path length of metal either liquid or solid and the tortuosity determined. The conductivity is related to the path length, are and resistance by[66]:

$$\sigma_m = \frac{l}{aR_m} \tag{25}$$

Where σ_m is the conductivity of the metal [$\Omega^{-1}m^{-1}$] at the measurement temperature, l is the length of the conducting path [m], a is the area of the conducting path [m^2].
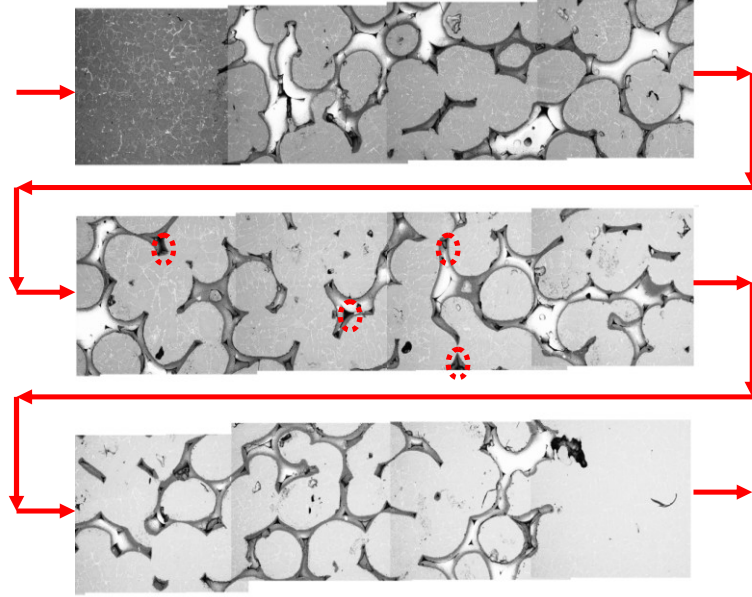
Figure.11 Representative SEM micrograph's showing a full 50 mm thickness vertical profile through of a well primed 50 ppi commercial alumina ceramic foam filter.

Inside of the filter, the available conducting area is reduced by the presence of non-conducting obstructions (e.g. trapped gas or solid and filter media), and the conducting path length is increased due to the tortuosity. Assuming that the filter media is the only significant obstruction, the reduced apparent electrical conductivity can be estimated as follows[66]:

$$\sigma_f = \frac{\sigma_m \varepsilon}{\tau} \qquad (26)$$

Where σ_f is the apparent electrical conductivity of the metal impregnated filter, the unit is $[\Omega^{-1}m^{-1}]$.

Rearranging Equation (26):

$$\tau = \varepsilon \frac{\sigma_m}{\sigma_f} \qquad (27)$$

17

An average temperature was used to estimate the liquid metal conductivity within the filter elements, starting with literature conductivity data for ultra pure metal, and correcting for the actual measured room temperature conductivity of the clean metal after experimentation:[67]

$$\sigma_m = \frac{IACS_m^{293K}}{24.77 \ 10^{-8} \ (1+0.000571 \ [T_m - 933.2]) \ 65} \quad (28)$$

Where IACS means 'International Annealed Copper Standard', $IACS_m^{293K}$ is the average room temperature conductivity of the solidified metal used during the experiment [% IACS] and T_m is the temperature of the liquid alloy under experimental conditions [K].

Chapter 3

Experimental Apparatus and Procedure

3.1 Optical Microscopy

3.1.1 Optical Microscopy - Theory

Initial investigations were carried out using optical microscopy, but the large magnification and small sample size made it necessary to switch to using an optical scanner. The optical microscope, also called the "light microscope", uses visible light and a set of lenses to enlarge the images of small samples. Optical microscopy is based on the principle of the compound microscope, which dates back to the 17th century. The basic optical microscope is very simple. Modern designs can greatly improve its properties, such like resolution and sample contrast. Optical microscopy uses visible light, and samples are directly observed visually by the user. These advantages make it easy to use and popular.

Modern developments allow observation of a sample via a computer by equipping the microscope with a digital camera. The microscope can also be controlled partly by computer. The images captured by the digital camera allow greater analysis, such as measurements of distances and areas. The *Figure.12* shows modern digital microscope.

Figure.12 Modern digital microscope-LEICA MEF4M.

3.1.2 Optical Microscopy - Experimental Procedure

The ceramic foam filters are brittle and fragile, so the grains of foam filter are easily broken off. Sample specimens obtained from the filters are therefore irregularly shaped, as well as porous. So it is necessary to mount the samples before analysis.

Firstly the filters are sectioned by cutting several small pieces from the surface to produce the samples. Samples are then mounted, using Epofix, which is a cold-resin based on two fluid epoxy components, a resin (bisphenol-a-diglycidylether) and a hardener (triethylenetetramine). Because of Epofix's low viscosity, it will penetrate into all the pores of the samples.

Afterwards it is necessary to sand the surface of the specimens using progressively finer SiC sandpapers such as #'s: 320, 400 and 600.

After preparation, the samples can be observed using the optical microscope.

3.2. Optical Scanning

The new procedure of diameter measurements used in this study: scanned filters by Epson Perfection V330 scanner (as shown in *Figure. 13*), and then measured the diameters manually with the help of Imagic ImageAcess easyLab 7 analysis software. The pictures' resolution is 1200 dpi (dots per inch) for 30 ppi, 40 ppi and 50 ppi CFFs, since 80 ppi CFF has much smaller cell, window and strut size, a higher resolution 2400 dpi was used. The pictures got by scanner are shown in *Figure.3*.

Figure. 13 Epson Perfection V330 scanner.[68]

There is no sample preparation for this method, as the CFF can be placed directly onto the scanner. So this new procedure was both easier and faster to use. Compared with optical microscopy, more measurements could be taken in the same amount of time, and a higher level of statistical significance achieved for the obtained averages.

3.3. Energy-Dispersive X-ray Spectroscopy

3.3.1 Energy-Dispersive X-ray Spectroscopy- Theory

Energy-dispersive X-ray spectroscopy is often abbreviated as EDS. It is an analytical technique used for elemental analysis. The working principle is that every element has a unique atomic structure allowing X-rays that are characteristic of an element's atomic structure to be identified uniquely from one another. An EDS system is commonly found on most Scanning Electron Microscopes (SEM). The operating principle of the SEM is that it scans a sample with a high-energy beam of electrons in a raster scan pattern, and the electrons will interact with the atoms that causing the sample to produce signals containing information about surface topography, composition and electrical conductivity.[69]

The elemental analysis obtained from the EDS is not very accurate. There are many factors affecting the accuracy of EDS. Light elements such as: H, He and Li can not be detected by X-ray spectroscopy, because they do not have enough electrons to produce characteristic X-rays. Many elements produce similar or identical signal peaks, for example Ti and V, Mn and Fe, making them difficult to distinguish.

3.3.2 Energy-Dispersive X-ray Spectroscopy - Sample Preparation

The samples must be cut to the correct size to fit in the specimen chamber and must be mounted on specimen stub. Samples also need to be electrically conductive, or at least electrically conductive on the surface. Non-conductive specimens tend to charge when scanned by the electron beam, especially in secondary electron imaging mode, which will causes scanning faults.[69] The CFF samples are embedded in Epofix, such that they are non-conductive. It is therefore necessary to coat them with an ultra-thin electrically conducting material. There are a lot of conductive materials that can be deposited on the samples by low-vacuum sputter coating, such as: gold, gold/palladium alloy, platinum, osmium, iridium, tungsten, chromium or graphite. [25] The author used graphite as the coating material. After the described procedure, the specimens can be used for EDS microanalysis.

3.4 Pressure Drop Experiments

The liquid permeability of 50 *mm* thick commercial foam filters with: 30, 40, 50 and 80 ppi, were measured using water as the working fluid, in a temperature range from 5-8 ^{o}C, typical density is 999.9 kg/m^3, viscosity is 1.3775×10^{-3} *Pa·S*. Mass flow rates from about 0.05 to 2 *kg/s* were used. Eight to ten different velocities were used to measure pressure drop for each filter.

Water is a very good analogue for liquid aluminium as it has a very similar dynamic viscosity to both aluminium and aluminium alloy A356 at normal casting temperatures (e.g. 700-720°C). A356 is a common foundry alloy and was the base alloy for the PhD. thesis to which this work relates. The common composition of A356 is 0.015 wt% Cu, 7.2 wt% Si, 0.38 wt% Mg, 0.120 wt% Fe, 0.032 wt% Ti and 0.0029 wt% B.[70] The dynamic viscosity of these three materials are presented in **Table III.**

Table III Dynamic viscosity of water, pure aluminium and A356 alloy.[71, 72, 73]

	Water	Pure Aluminium	A356
Temperature (^oC)	7	710	710
Dynamic Viscosity (Pa·S)	1.38E-03	1.25E-03	1.03E-03
Density (kg/m^3)	1000	2386	2340
Kinematic Viscosity (m^2/s)	1.38E-06	5.25E-07	4.41E-07

The experimental set-up shown in *Figure.14* was designed by Mark W. Kennedy and the filter housing was constructed by Egil Torsetnes. *Figure.15* shows the close up of the filter housing. The pressure transducer was an AEP DF-2, 0-1 Bar measuring range, 4-20 *mA* output. The pressure was shown by means of electric current, and the transducer was factory calibrated and certified to an error of ±0.04% of reading, over the full scale from 0-1 Bar, using a 6 point calibration, represented the greatest uncertainty in the experimental and defining the experimental uncertainty limits. The transducer was powered using a MANSON, 0-30 *V,* 2.5 *A*, DC power supply. The electric current measurements were taken using a FLUKE 26 III, True RMS Multimeter. During the experiments the current produced by the transducer at zero liquid flow velocity was determined manually using a FLUKE 26 III, True RMS Multimeter (Fluke, USA) to a precision of 0.001 *mA* (6.25 *Pa*), using the lowest available current scale. Current during the flow measuring periods were computer data logged at 100 *mS* intervals by conversion to a 0-5 *V* signal, with a resolution of 0.001 *V* or 0.004 *mA* (i.e. 25 Pa resolution). At higher than 4 *mA*, no bias could be detected between the manual and automated current readings, at the available 0.01 *mA* resolution (the FLUKE switched to a lower resolution at greater than 4.099 *mA*).

The pressure was produced using a Jula 1000 *W* submersible pump and with a maximum pressure of 0.8 *Bar*. Fluid velocity was controlled by the use of a ball valve. Flow rate was computed by the ratio of weight gain in a 100 L tank vs. time, with the help of a computerized data logger (DATASCAN 7220, Analogue Input Measurement Processor), which scanned the scale weight at 100 *ms* intervals.   The scale used had a 4-20 *mA* output over a range of 0-100 *kg*, with a resolution of 10 *g*. The data logging software used was DAS-16, version 1.0.

Figure.14 Photograph of experimental set-up constructed using DN 50 mm x 1.8 mm plastic pipe.
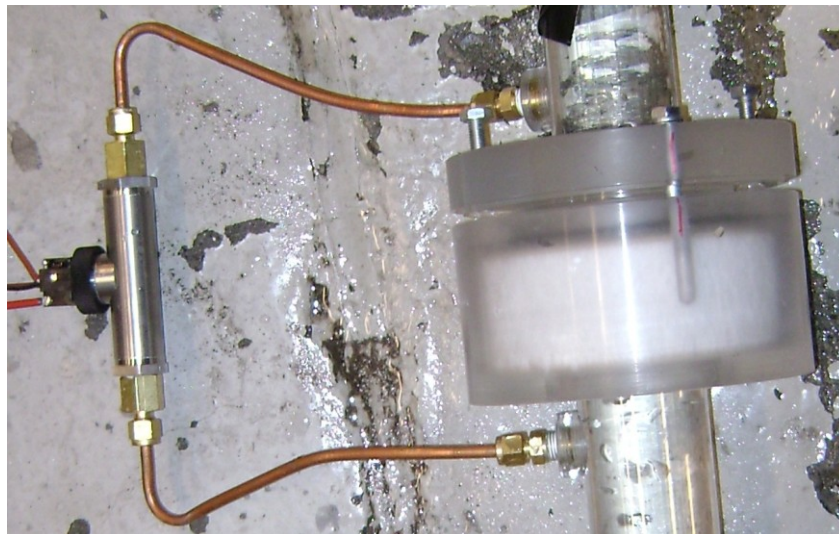
Figure.15 Close up of filter housing.

The water temperature was determined using 1 *mm* diameter Type K, Inconel sheathed thermocouples and a FLUKE 51 II thermocouple reader. Thermocouple readings were also data logged.

These experiments were a continuation of the project "Liquid Permeability of Ceramic Foam Filters", completed as part of course number "TMT 5500". The initial procedure which was used previously was to directly put the large diameter 101 *mm* CFFs into the filter housing without any measures to avoid liquid bypassing at the outer periphery (gaskets were used on

top and bottom). The experiment procedures were sequentially improved during the current set of experiments on two occasions. The modified procedure (Method 1), used silicon grease evenly daubed onto the side surface of the CFFs. The final procedure (Method 2), used paper (cellulose) placed onto the side surface of CFF, which had silicon grease on it. ***Figure.16*** shows these different procedures. Swelling of the cellulose fibres on contact with water provided a negligibly permeable seal along the whole length of the side of the filter media.
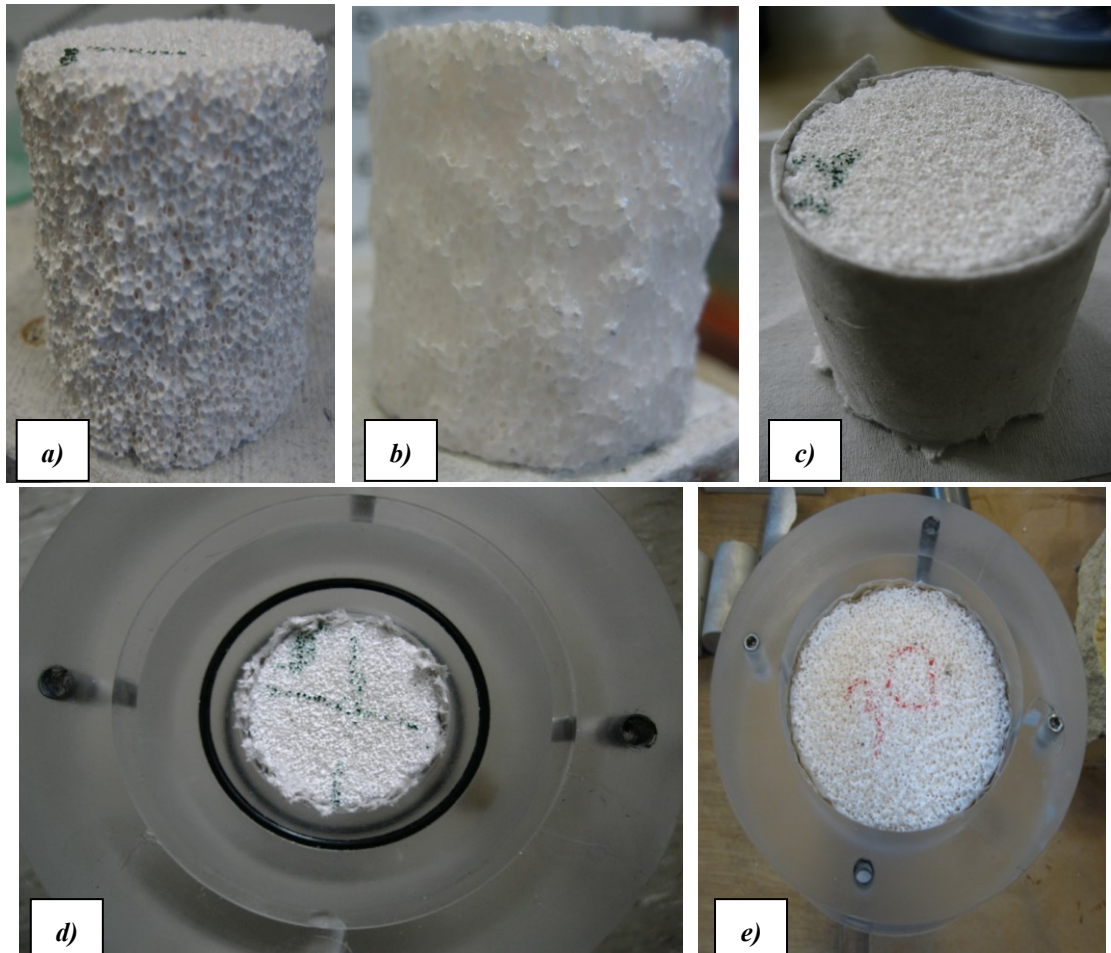
Figure.16   *a) 49 mm(diameter) CFF sample. b) 49 mm CFF, Method 1. c) 49 mm CFF, Method 2.*
d) 49 mm CFF in the filter housing, using Method 2. e) 101 mm CFF in the filter housing,
using Method 2.

There are two different designs of filter housings, one is for the experiment of filters with ~101 *mm* diameter, and the details are shown in ***Figure.17***. A smaller filter housing was designed for testing the ~49mm diameter filters, as shown in ***Figure.18***.
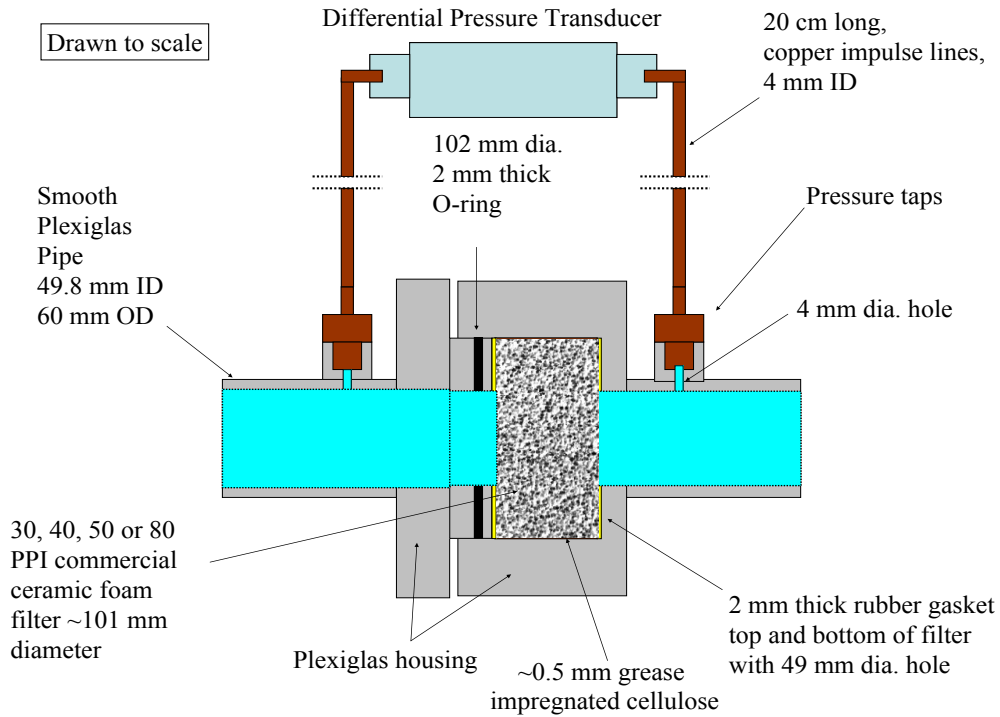
Figure.17 Filter housing for ~101 mm diameter CFFs.
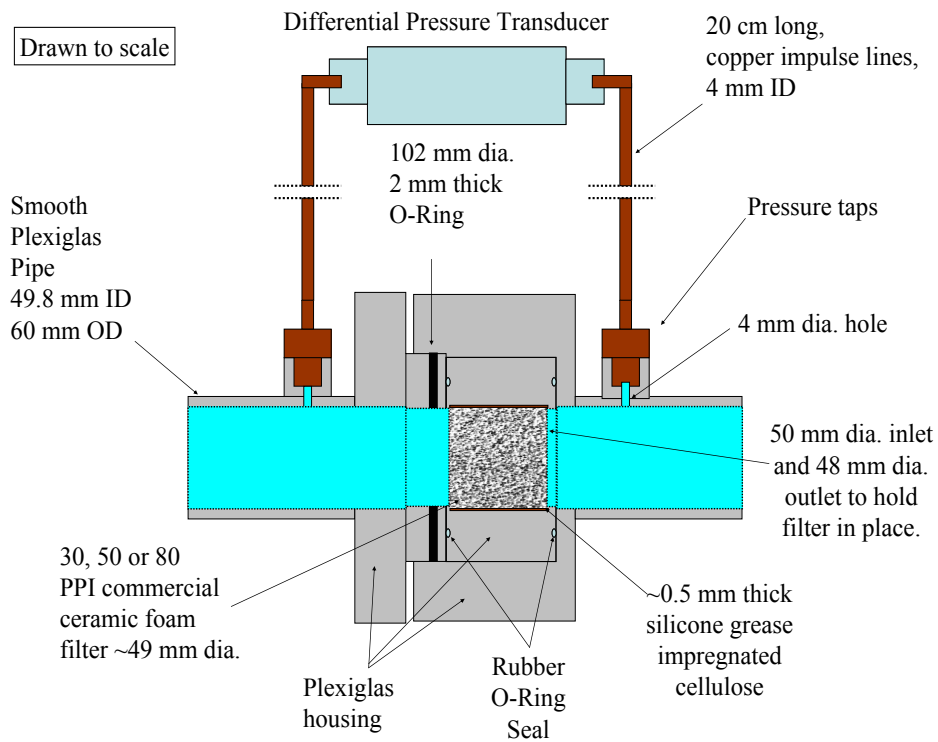
Figure.18 Filter housing for ~49mm diameter CFFs.

3.5 Tortuosity Experiments

As previously mentioned, the tortuosity of the CFFs was obtained by measuring the electrical resistivity when CFFs completely filled with a conductive medium. Aluminium was used in the experimental program.

The CFF was contained for the experiment in a type of filter bowl built using two Bimex® 400 fibre tubes, each 150 *mm* high and with an internal diameter about 100 *mm* (4"). The CFF was mounted in the top of the lower refractory tube with Fibrefrax cement. Fibrefrax mouldable cement was also used to glue the two fibre tubes together. The dimensions of the filters have been standardized to 50 *mm* thick and were sanded to 100 *mm* diameter (see *Figure.19*[22]).

Figure.19 30 ppi Sivex® CFFs (left side) and Bimex® 400 insulated crucibles (right side).

Three filters with same ppi and 50 *mm* thickness were stacked on top of each other in the tube. The last mounting step was to place the 300 *mm* tube on a dense alumina fibre plate, as shown in *Figure.20*. The mounted crucibles were than dried for 12 hours at 60°C in a ventilated oven.

Figure.20 Mounted crucible.

The effective electrical conductivities of the filters were also determined from the same liquid metal electromagnetic induction experiments, using procedures described in detail elsewhere.[74,75,76] A schematic of the apparatus used is shown in ***Figure 21 a)*** and a photograph is shown in ***Figure 21 b)***. The power induced in a tight stack of three 50 *mm* thick, and ~100 *mm* diameter filters of 30, 40, 50 or 80 ppi was determined electrically at a known temperature (and therefore metal electrical conductivity), while filled with 'commercially pure' aluminium alloys with initial electrical conductivity from 61-62% IACS. Temperatures were logged every 100 *ms* by type K thermocouples located under and over the 150 *mm* stack of filters.
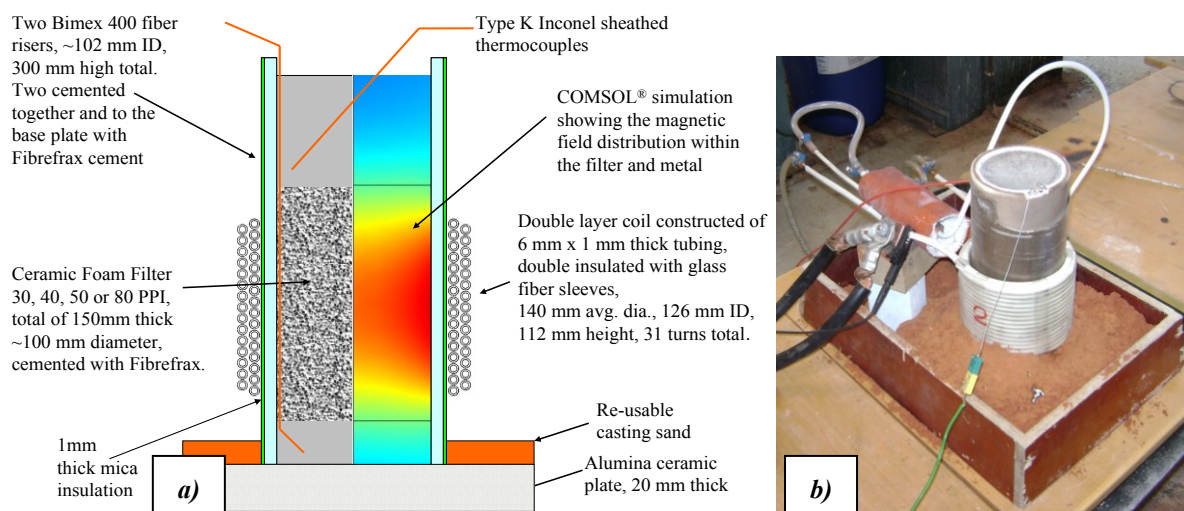
Figure.21 Schematic of the filter tortuosity apparatus (a) and photograph (b), showing a 2 layer, 31 turn (total) induction coil, operated at 371-734 A, using line frequency 50 Hz AC power.

27

Chapter 4

Results and Discussion

4.1 CFF Porosities

There are two types of porosity in CFFs: effective porosity, also called open porosity, it refers to the fraction of the total volume in which fluid flow is effectively taking place; ineffective porosity, also called closed porosity, that refers to the fraction of the total volume in which fluids or gases are present but in which fluid flow cannot effectively take place and includes the closed pores.[77]

It should be noted that the total and open porosity are of very similar magnitude in this study, as shown in *Figure.11*, areas of 'closed' porosity can be seen in black, some of which are highlighted by dotted circles as examples, visual inspection confirms nearly all macroscopic porosity is filled with metal. Previous literature[78,79] have described the morphological characterization of CFFs in detail, by using mercury at up to 4000 *Bar* and found that the difference between the total and the open porosity is <5% of the measured valued, even when metal is forced at very higher pressure into the microscope pores between individual ceramic particles. The convention of Dietrich has therefore been followed in this work, i.e. the equality between total and open porosity.

The total porosity was computed through Equation (29):

$$Porosity = \frac{(TheoreticalWeight - ActualWeight)}{TheoreticalWeight} \qquad (29)$$

The composition of the CFFs was measured by EDS, and it was found that it is mainly alumina, as indicated in *Figure.4*. The maximum theoretical density of alumina, e.g. corundum is 3.9-4.0 g/cm^3 could be used to compute the weight of a given volume of CFF and hence a total porosity estimated. A more precise value of 3.48 (average of 3 readings) ±0.02 g/cm^3 determined by helium pycnometery, for the exact type of ceramic used by Sivex in the construction of their CFF filters, was actually used in the present study, based on private communication with Norsk Hydro.

For the 30, 50 and 80 ppi filters, porosity measurements were taken for complete commercially sized filter elements (23'', 20'' and 23'' square). The porosity and other relevant

information are listed in **Table IV**.

Table IV Porosity and other relevant information

ppi	Filter Number	Volume (cm³)	A.Weight (kg)	T.Weight (kg)	ε
30 ppi	I	16163	6.21	56.57	0.890
30 ppi	II	16132	6.18	56.46	0.891
40 ppi	19	393	0.157	0.137	0.886
50 ppi	I	12023	5.84	42.08	0.861
50 ppi	II	12082	5.62	42.29	0.867
80 ppi	I	16134	7.86	56.47	0.861
80 ppi	II	16022	7.61	56.075	0.861
80 ppi	III	16121	7.96	56.42	0.859
80 ppi	IV	16022	8.16	56.075	0.855

Figure.22 illustrates the relationship between ppi and porosities. It can be found that CFFs with a higher nominal pore count have lower porosity, e.g. for 80 ppi vs. 30 ppi. A constant ceramic thickness deposited on the original polymer substrate is the likely cause of the relationship.
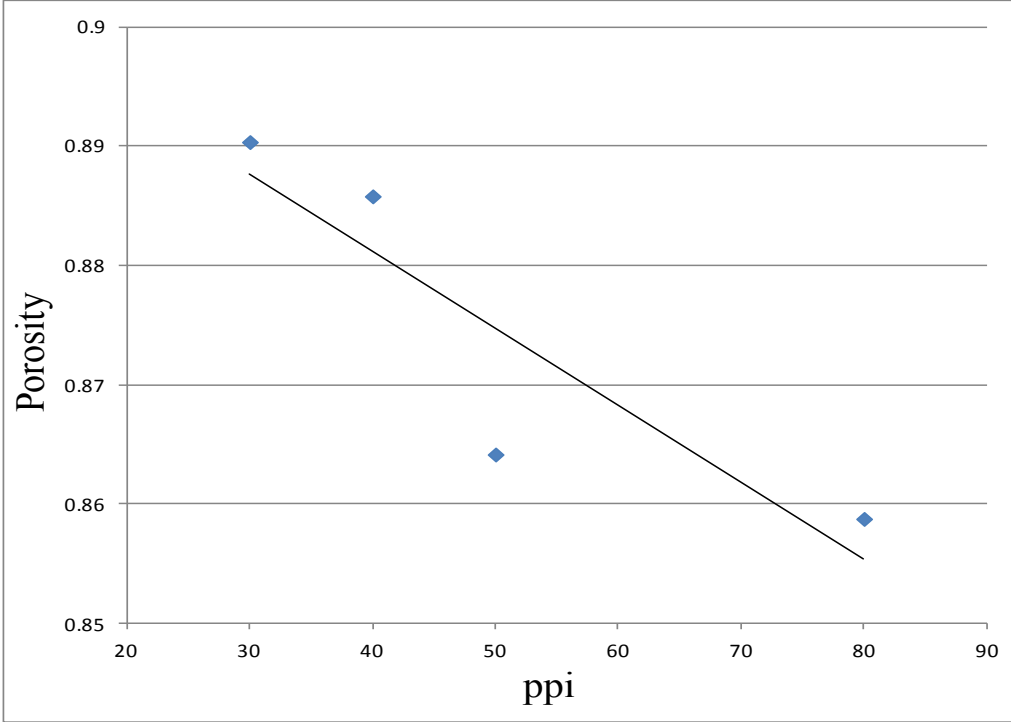
Figure.22 Fractional CFFs porosity versus ppi.

4.2 Cell, Window & Strut Diameter

200 measurements of the cell and window, and 40 measurements of the strut diameters were taken for each filter type. Averages as well as sample standard deviations have been calculated for each filter type. 95% confidence intervals have been estimated for each mean using the students-T distribution, based on the number of actual degrees of freedom, to adjust for the different sizes of the sample populations. These values are listed in **Table V-VII**, and the measured experimental data are plotted as histogram in *Figure.22-24.*

Table V Information of cell size, d_c

	30 ppi	40 ppi	50 ppi	80 ppi
Measurement Times	200	200	200	200
Mean Size (μm)	1668	1306	1131	683
Minimum Size (μm)	720	525	549	392
Median Size (μm)	1730	1345	1181	689
MaxmiumSize (μm)	2722	1975	1667	953
Standard Deviation	417	251	229	122
95%Confidence	57.8	34.8	31.8	16.9

Table VI Information of window size, d_w

	30 ppi	40 ppi	50 ppi	80 ppi
Measurement Times	200	200	200	200
Mean Size (μm)	962	699	623	384
Minimum Size (μm)	443	273	317	212
Median Size (μm)	962	714	597	381
MaxmiumSize (μm)	1878	1050	1308	689
Standard Deviation	190	151	130	87
95%Confidence	26.4	20.9	18.0	12.0

Table VII Information of strut size, d_s

	30 ppi	40 ppi	50 ppi	80 ppi
Measurement Times	40	40	40	40
Mean Size (μm)	185	211	190	119
Minimum Size (μm)	85	127	127	74
Median Size (μm)	191	200	190	117
MaxmiumSize (μm)	254	295	274	170
Standard Deviation	41	46	36	20
95%Confidence	5.7	6.4	5.0	2.8

Histograms have been made of the 200 counts of window diameter (d_w) as can be seen in *Figure.23 a)* through *d)* for the 30-80 ppi filter types. Median values are indicated by dotted lines.
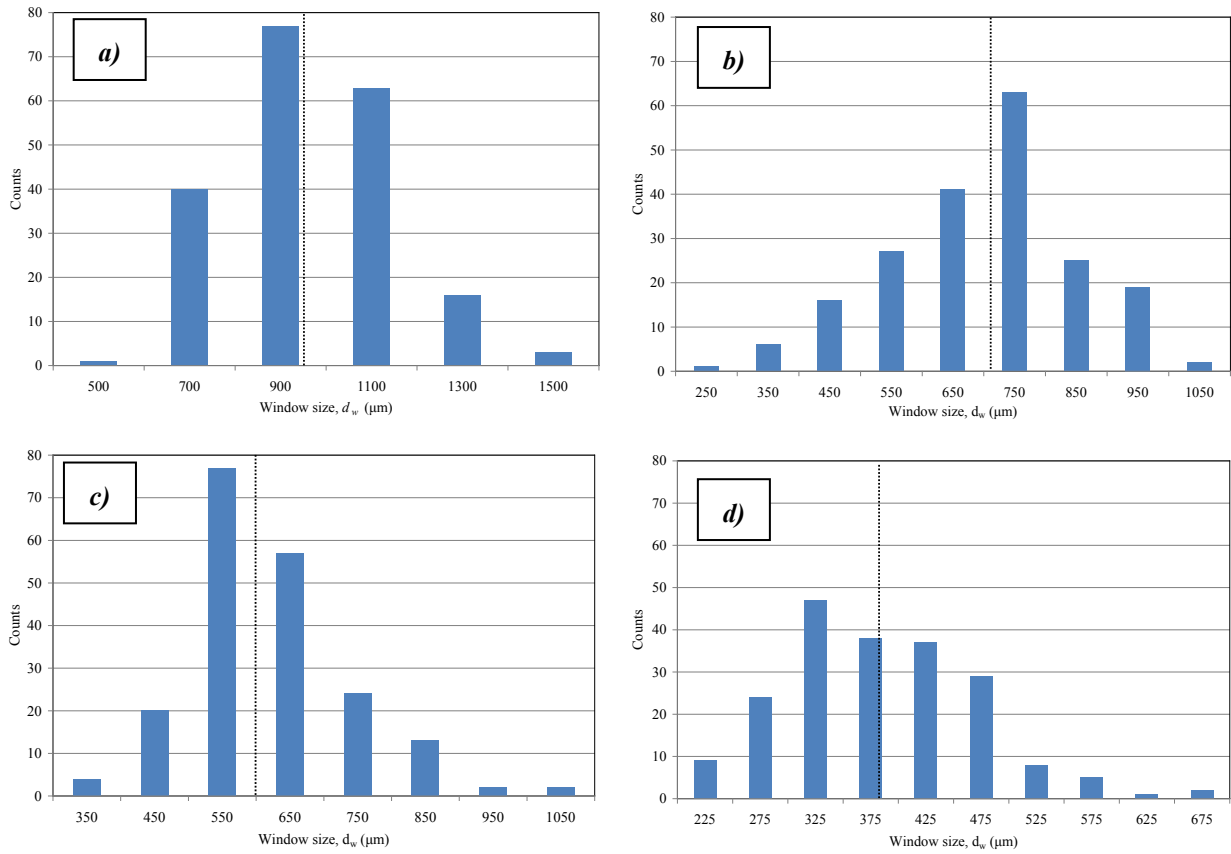
Figure.23 **Histograms of a) 30, b) 40, c) 50 and d) 80 ppi window sizes (d_w) [μm]. Median values are marked with dotted lines.**
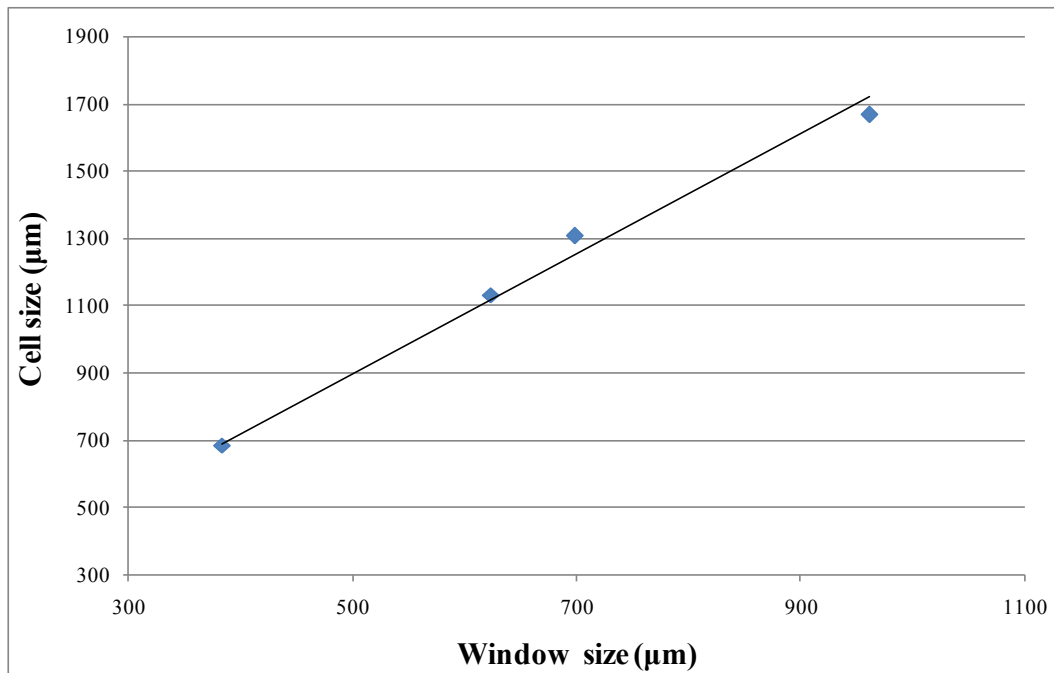
Figure.24 Commercial ceramic foam filters cell size (d_c) versus window size (d_w) [μm].

Average cell diameter (d_c) has been plotted versus the average window diameter (d_w) in **Figure.24** and the results correlated according to the following equation:

$$d_c = 1.787 d_w, \quad R^2 = 0.987 \hspace{3cm} (30)$$

The linear relationship between cell and window diameters implies a simple geometric relationship, likely originating with the original substrate used during the filter fabrication process. Agreement with literature values for both cell and window sizes for similar alumina CFFs is excellent.[80]

4.3 Pressure Drop Results

28 pressure drop experiments were done to achieve the following:

1) Develop and validate an adequate experimental procedure and apparatus.
2) Compare the pressure drop of CFF samples from the same filter and same position, but with different diameters, i.e. the 101 and 49 *mm* filter elements to verify the adequacy of the experimental and modelling procedure.
3) Correlate pressure drop with liquid velocity.
4) Determine the permeability of different types of filters, i.e. obtain k_1 and k_2 for Equation (2).
5) Determine the variability of permeability between different filters of the same ppi.
6) Measure the permeability variation for the same CFF with changes in sample position. (In order to describe the sample's position clearly, different numbers represent different positions. ***Figure.25*** shows the detailed information.)
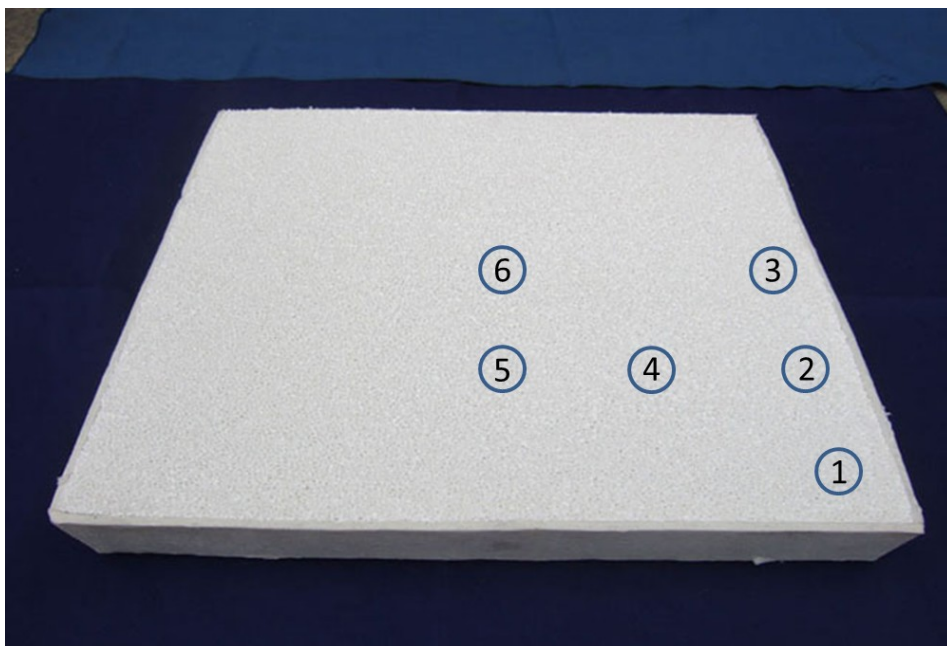
Figure.25 CFF sample position code.

The details describing each experiment are shown in the **Table VIII**. The sections 2-21 were cut from the whole filters (23'', 20'' and 23'' square). Sections 22-24 were cut from the centre of sections 18, 20 and 21.

Table VIII Strut size and relevant information

Test No.	Section No.	ppi	Filter No.	Section Diameter (mm)	Section Thickness (mm)	Method	Inlet Length (mm)	Section Position
1	2	30	I	48.57	50.18	1	106	6
2	15	80	IV	48.97	49.77	1	106	6
3	14	80	II	48.82	50.44	1	106	6
4	2	30	I	48.57	50.18	2	106	6
5	15	80	IV	48.97	49.77	2	106	6
6	14	80	II	48.82	50.44	2	106	6
7	4	50	I	48.61	50.6	2	106	2
8	4	50	I	48.61	50.6	2	306	2
9	20	50	N/A	~101	49.58	2	106	N/A
10	20	50	N/A	~101	49.58	2	306	N/A
11	1	30	I	48.71	50.48	2	106	1
12	3	50	I	48.95	50.37	2	106	1
13	5	50	I	48.65	50.43	2	106	3
14	6	50	I	48.86	50.56	2	106	4
15	7	50	I	48.80	50.26	2	106	6
16	8	50	I	49.37	50.49	2	106	5
17	11	80	I	48.00	50.59	2	106	6
18	12	80	III	48.94	50.07	2	106	6
19	13	50	II	49.39	49.97	2	106	1
20	16	80	N/A	48.84	50.06	2	106	6
21	17	50	N/A	49.12	50.41	2	106	1
22	17	50	N/A	49.12	50.41	2	106	1
23	18	30	N/A	~101	50.67	2	106	N/A
24	19	40	N/A	~101	47.65	2	106	N/A
25	21	80	N/A	~101	50.31	2	106	N/A
26	22	30	N/A	48.67	50.67	2	106	N/A
27	23	50	N/A	49.15	49.58	2	106	N/A
28	24	80	N/A	49.08	50.31	2	106	N/A

The section diameter and section thickness in **Table VIII** were measured by micrometer and the average of 4 and 6 readings, were used respectively. The test number 22 which is marked in yellow used the same filter as test 21, but in the opposite flow direction. The details of the experimental data are presented in Appendix Tables 1-28. The velocity given in the table is the calculated superficial velocity, and the temperature, density and viscosity are the fluid (i.e. water) properties. In order to determine the effective superficial velocity for the 101 *mm* filters, it was necessary to use computational fluid dynamics (CFD) to solve for average diameter of the flow field. An 'effective' flow field diameter was initially guessed for use with Equation (2), the resulting k_1 and k_2 terms were then used with the CFD model and the

pressure gradient determined. If the results were in error, a new 'effective' diameter was guessed and the procedure repeated until convergence was achieved.[66] The details of the CFD model that was used, are introduced in Chapter 5.

4.3.1 Improvement of Procedures

As mentioned previously, this research continues work begun during project "Liquid Permeability of Ceramic Foam Filters" for course TMT 5500. The procedures used to determine the experimental pressure gradient have been modified for these experiments. The first method (e.g. Method 1) used this time was to daub thick high viscosity silicon grease onto the side surface of CFF, in order to avoid bypassing of the fluid flow and obtain more exact, i.e. higher pressure drop data.

The CFF number 2-30 ppi was used for the first test. The data are plot in *Figure.26*. It can be seen that the highest point on the plot deviates significantly from the curve fitting the rest of the data. This may be because the high velocity gave a very high pressure, which acted to push the grease out of the filter housing, creating fluid bypassing, and resulting in a reduced pressure drop.
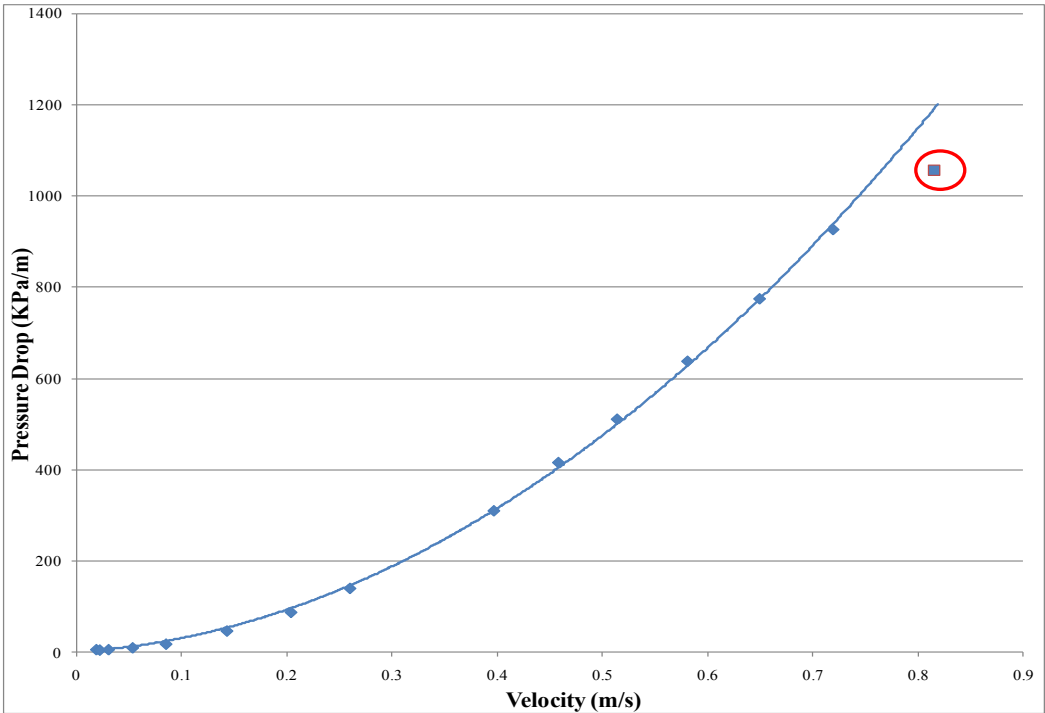
Figure.26 Experiment data of 2-30 ppi by using Method 1.

Two additional tests were done to prove the hypothesis from the first test. Filter numbers 14-80 ppi and 15-80 ppi were used in these tests. *Figure.27* shows the data for 14-80 ppi. The last 5 points, which are marked in the red circle, obviously deviate from the curve. It can be

concluded that operation at high velocity and high pressure caused a loss of the silicone sealant and a reduced reading of the pressure gradient.
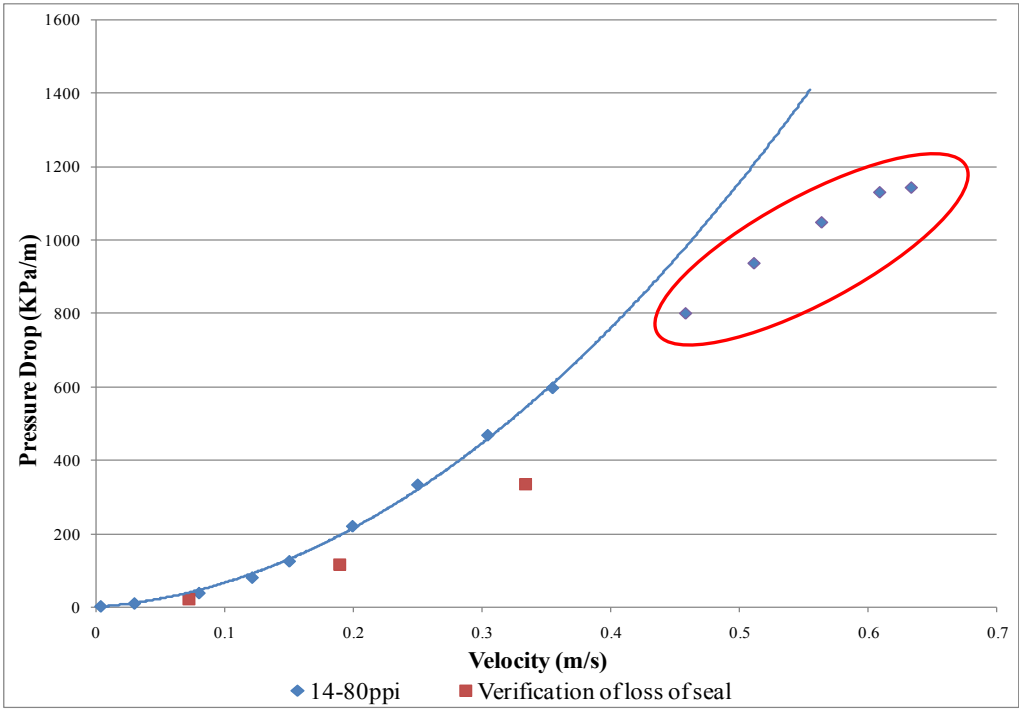
Figure.27 Experiment data of 14-80 ppi by using Method 1.

Visual observation through the Plexiglas housing showed that the sealant was forced out of the channel at the wall, as shown in *Figure.28 b)*. The verification of loss of seal in *Figure.27* was obtained by repeating the measurements, and after the loss of seal, the obtained pressure drop data become smaller than was initially measured. These data indicate that the sealing of the sides of the filter is critically important to obtaining accurate data, and the use of a high viscosity silicone alone is not enough to avoid bypassing.
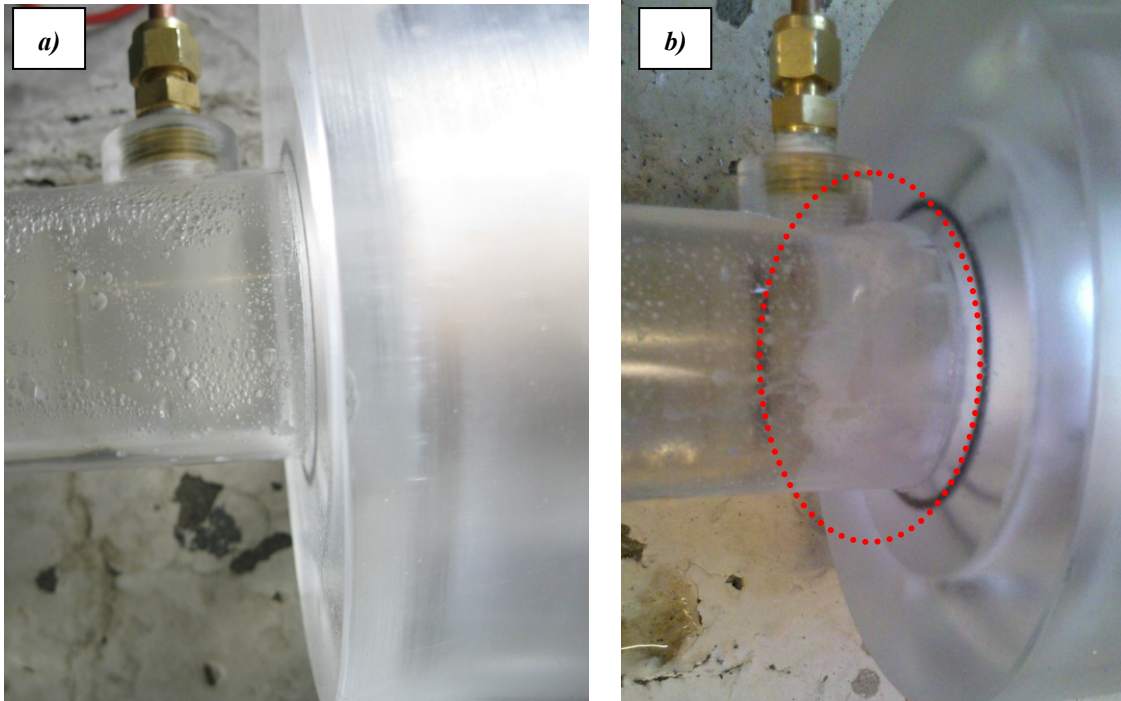
Figure.28   ***a) Filter housing before high velocity experiment.***
b) Filter housing after high velocity experiment.

The final procedure (e.g. Method 2) was suggested by Mark W. Kennedy. Water swollen cellulose and silicone were used to provide a very low permeability seal, which was not subject to physical removal at pressures of up to 0.8 *Bar*. This was verified both visually and by repeated measurements over the whole pressure range with test filters. Comparison of results for the filter using Method 1 and Method 2 is presented in ***Figure.29*** and ***Figure. 30***. From these figures it can be seen that, high flow and tight filters created large driving force for bypassing. Experimental errors will tend to report lower pressure gradients and greater permeability than reality.
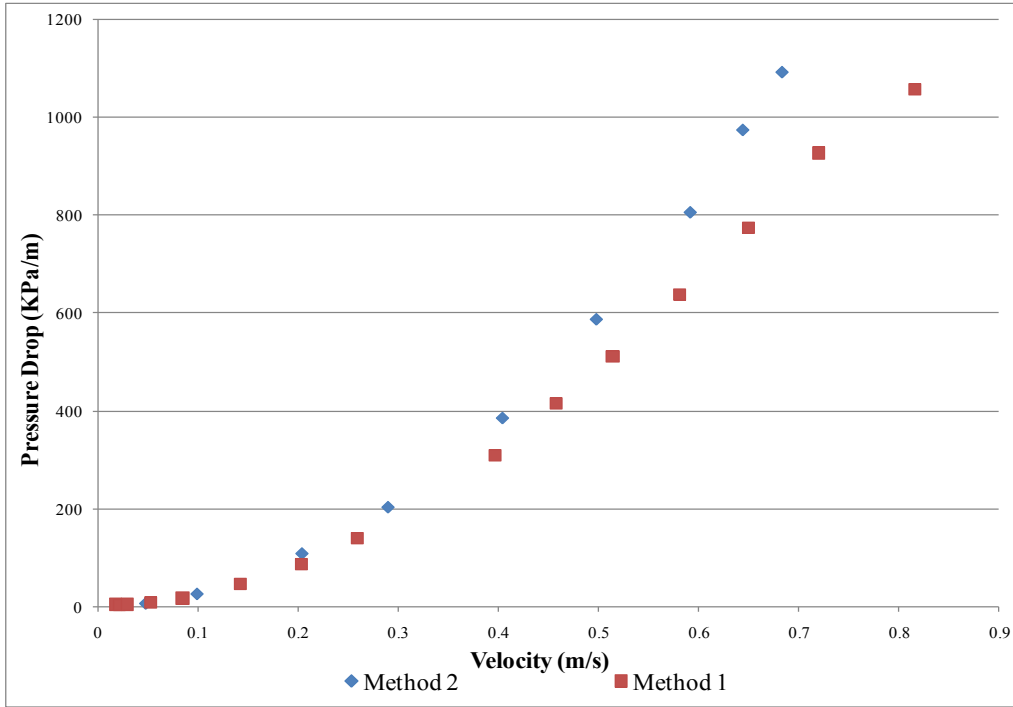
Figure.29 Comparison of results for the 2-30 ppi filter using Method 1 and Method 2.
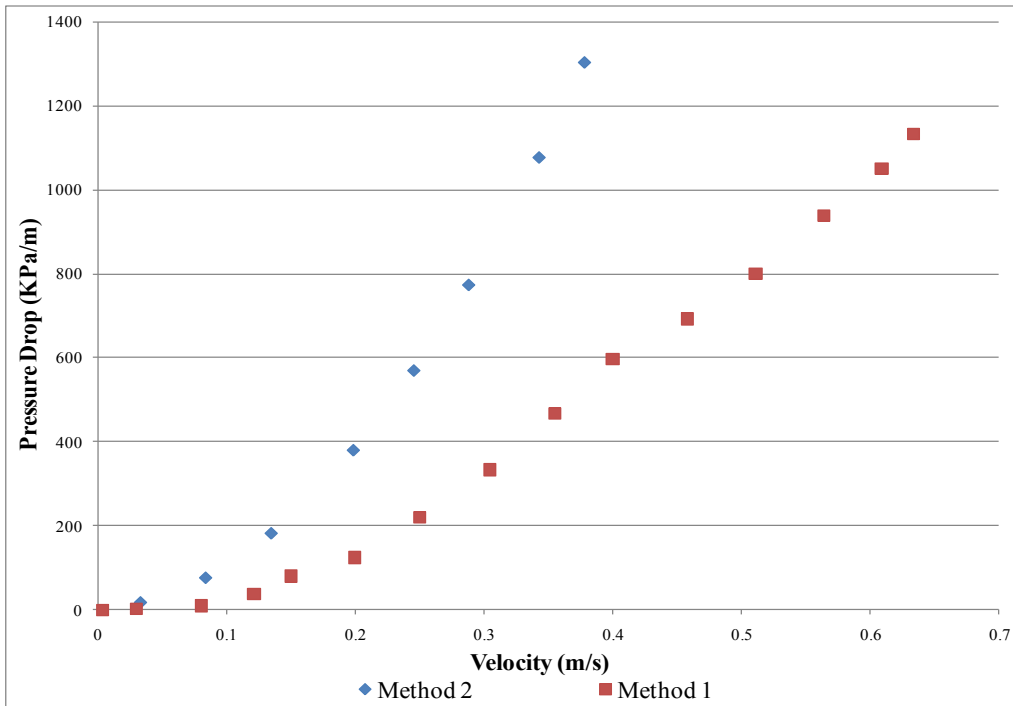
Figure.30 Comparison of results for the 14-80 ppi filter using Method 1 and Method 2.

4.3.2 Required Inlet Length to Fully Develop the Flow Regime

As shown in *Figure.9*. the filter holders were used in a piping circuit containing ten 90° bends, with 5 located before and 5 after the filter holder apparatus. There was a total of 8.3 *m* of piping with a 1.06 *m* straight section before the filter housing, and the pipe inner diameter was 0.0464 *m*.

Using Equation (19), *EL=23*.

Assumping a water temperature of 7°C, a water density of ρ=999.9 *kg/m³*, and a viscosity of μ=1.3775×10⁻³ *Pa·s*, the required entrance length number can be estimated by using Equation (17), (23) and (24),. Details are shown in **Table IX**.

Table IX Required inlet length to fully develop flow as a function of pipe Reynolds number

Velocity (m/s)	Re	L/D inlet Laimanal	L/D Inlet Turbulent	Estimated L/D Inlet
0,03	1010	30	N/A	30
0,05	1680	50	9	29,5
0,1	3370	N/A	10	10
0,2	6740	N/A	12	12
0,4	13470	N/A	15	15
0,8	26940	N/A	17	17
1	33680	N/A	18	18

From **Table IX**, it can be seen that except at very low velocity, the inlet length should be adequate to achieve fully developed flow (i.e. '99% approach'). The impact of back-to-back and out–of –phase 90° bends on the flow, will be to promote turbulence even at low Reynolds numbers.
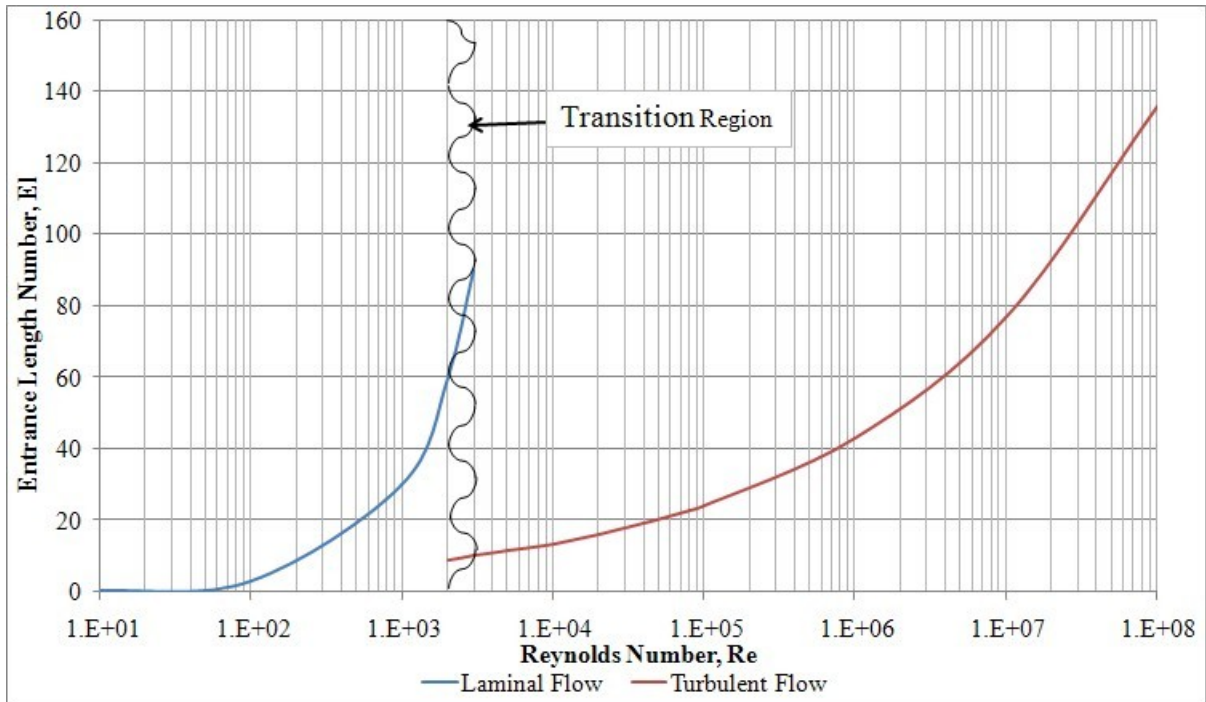
Figure.31 Entrance length number versus Reynolds number.

The flow regimes during the experiments include laminar flow, transitional flow and turbulent flow. As shown in *Figure.31*, it is hard to determine the entrance length number at the transition region, and as a result longer pipes were used in the experiment to verify the computation. The total pipe length was then 12.3 *m*, with 3.06 *m* of straight section before the filter housing. The entrance length number became, *EL=66*. The long configuration should be adequate to achieve fully developed flow at all Reynolds numbers. Filters 4-50 ppi and 18-50 ppi were used to verify this hypothesis. *Figure.32* presents the comparison of the obtained pressure drop data of filter 18-50 ppi using the two different circuit configurations.
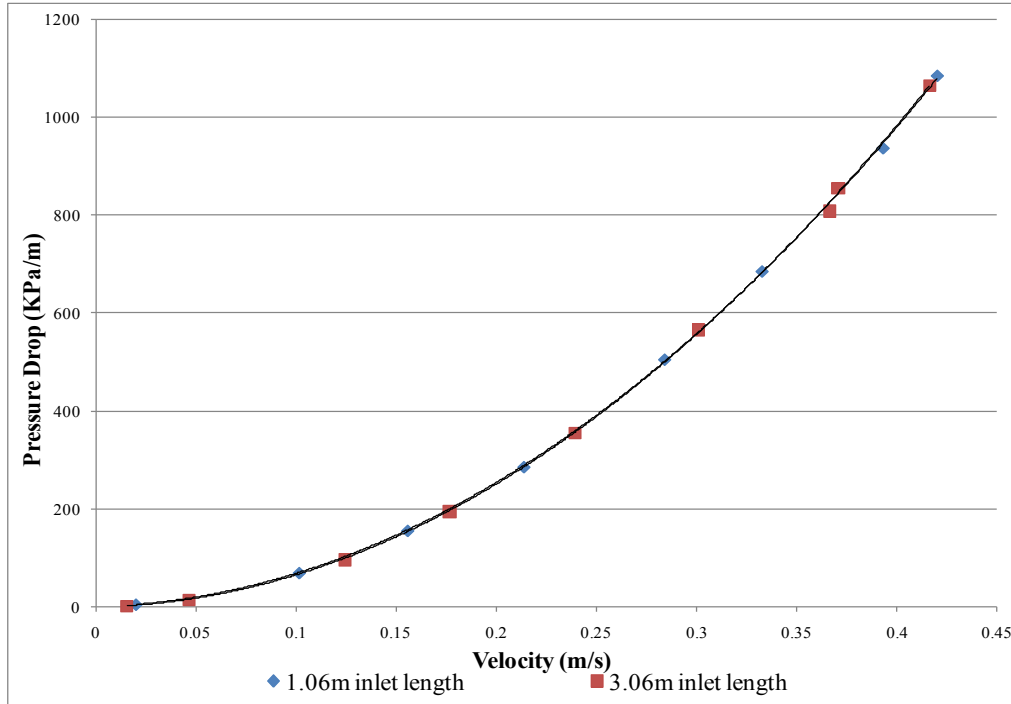
Figure.32 Comparison of results for the 20-50 ppi filter using both the short and long inlet lengths.

The regressions of the experimental data are shown below:

$$1.06 \text{ } m \text{ inlet length: } y = 5917160.66x^2 + 83380x, R^2 = 0.99995 \quad (31)$$

$$3.06 \text{ } m \text{ inlet length: } y = 5837058.41x^2 + 90658x, R^2 = 0.99956 \quad (32)$$

From the ***Figure.32***, it can be seen that two experiments obtained virtually identical results. The second order terms of the Equations (31) and (32) are ~1.35% different. This may be caused by the accuracy of the data logger, different tightness of the filter housing or residual gas bubbles in the pipes or may in fact be the correct impact of inlet length. Since this research has been conducted primarily in order to test the permeability at high velocity, second order effects are much more than the first order. So the difference in the first order of the two regressions is not very significant. During the long configuration test, it was very difficult to empty the gas bubbles from the system, and it was therefore decided to use the short configuration for the remainder of the experiments.

4.3.3 Permeability of Different Types of Filters.

The obtained results from pressure drop experiment for test 23, 24, 9 and 25 are shown in ***Figure.33***. They are all for 101 *mm* diameter filters with 30 ppi, 40 ppi, 50 ppi and 80 ppi. The

'effective' flow field diameters for computing the superficial velocities are 65.5 *mm*, 66 *mm*, 66.1 *mm* and 66.5 *mm* respectively. At higher velocity, the pressure drop increases faster for CFFs with a higher nominal pore count, e.g. for 80 ppi vs. 30 ppi, this apparently causes the effective flow field diameter to also increase, in order to minimize the total pressure drop.
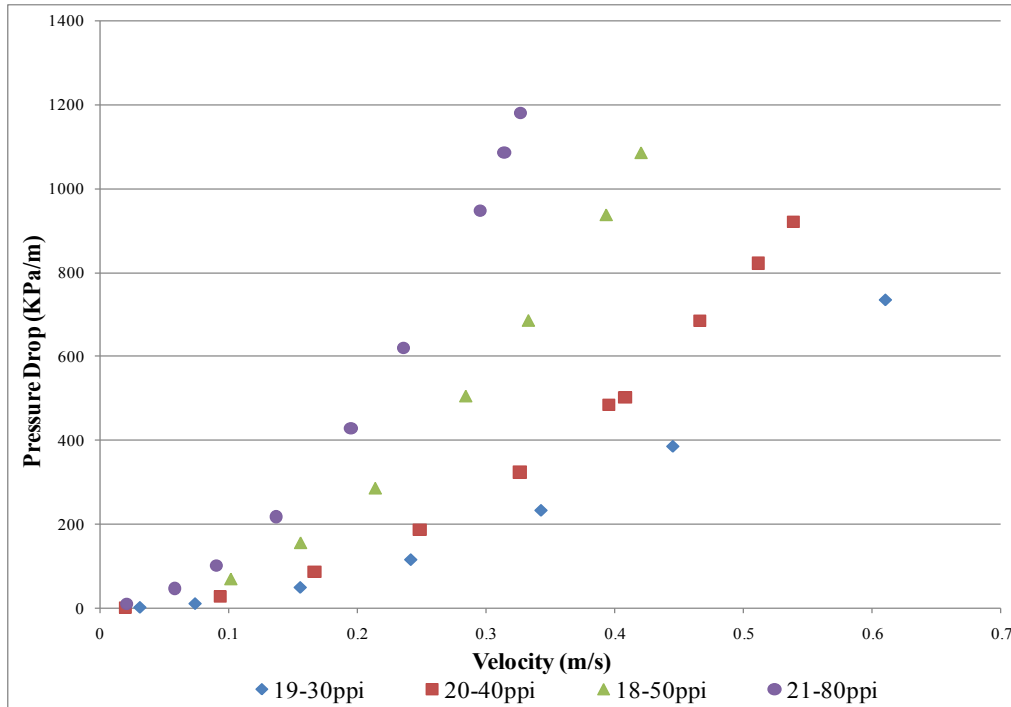
Figure.33 Experimental data for tests 9, 23, 24 and 25.

The regressions of the experimental data are shown below:

$$19\text{-}30 \text{ ppi:} \quad y = 1903861.95x^2 + 24661x, R^2 = 0.99979 \qquad (33)$$

$$20\text{-}40 \text{ ppi:} \quad y = 2959253.57x^2 + 45880x, R^2 = 0.99966 \qquad (34)$$

$$18\text{-}50 \text{ ppi:} \quad y = 5917160.66x^2 + 83380x, R^2 = 0.99995 \qquad (35)$$

$$21\text{-}80 \text{ ppi:} \quad y = 10036001.67x^2 + 248300x, R^2 = 0.99959 \qquad (36)$$

Using the current equipment in this study, the pressure resolution during flow was 62.5 *Pa*, or a gradient uncertainty of ±625 *Pa/m* depending on the sample's thickness. ±625 *Pa/m* represents more than 5% uncertainty at flow rates of <0.03-0.08 *m/s*, depending on filter type (i.e. ppi). It was necessary to determine both k_1 and k_2 from flow conditions, where both terms were simultaneously significant [66], i.e. it was not possible to operate in a purely 'Darcy' regime with this pressure measuring apparatus and obtain 'precise' results.

Three different procedures were explored[66] to derive the Forchheimer coefficients, e.g. k_1 and k_2 in Equation (2):

1) An 'automated' second order regression, with a zero intercept, using Excel 2003.
2) Ergun et al.'s procedure of dividing Equation (2) by the velocity and performing a linear regression. [81]
3) An iterative procedure to first guess k_1 and then correlate the remainder for k_2 using an exponential regression.

The experimental parameters obtained for tests 9, 10, 23, 24, 25, 26, 27 and 28 were calculated by all of the above procedures, and the values summarized in **Table X**.

Table X Comparison of three mathematical procedures to determine k_1 and k_2

Test Number	Filter Number	Excel 2003 Forchheimer k_1 (m)	Excel 2003 Forchheimer k_2 (m^2)	Ergun Method Forchheimer k_1 (m)	Ergun Method Forchheimer k_2 (m^2)	Method 3 Forchheimer k_1 (m)	Method 3 Forchheimer k_2 (m^2)
26	22-30 ppi	2.141E-08	5.827E-04	4.582E-08	5.481E-04	5.084E-08	5.459E-04
23	18-30 ppi	2.463E-07	5.097E-04	7.187E-08	5.177E-04	5.572E-08	5.252E-04
24	19-40 ppi	-2.035E-08	3.047E-04	1.090E-07	3.240E-04	3.099E-08	3.379E-04
27	23-50 ppi	1.836E-08	1.645E-04	1.628E-08	1.653E-04	1.568E-08	1.656E-04
9	20-50 ppi	1.631E-08	1.693E-04	1.244E-08	1.718E-04	1.710E-08	1.690E-04
10	20-50 ppi	4.670E-08	1.638E-04	2.166E-08	1.667E-04	1.525E-08	1.713E-04
28	24-80 ppi	1.897E-08	1.077E-04	8.676E-09	1.111E-04	6.519E-09	1.148E-04
25	21-80 ppi	9.694E-09	9.449E-05	6.583E-09	9.680E-05	5.441E-09	9.963E-05

It should be noted that it is clear that the negative coefficient k_1 for the 19-40 ppi filter obtained from Excel 2003 is physically meaningless. No physically meaningful correlations could be performed on the values of k_1 and k_2 found using Excel, e.g. comparison with total porosity or window size. Better results were obtained following the recommended method of Ergun. The most physically meaningful results were obtained following the 3rd procedure, where k_1 was initially guessed, the first order component of Equation (2) subtracted from the total and an exponential regression performed on the remainder. When the exponent on the velocity became 2.00000, the procedure was deemed converged.

The balance of the experiment parameters were all computed using the 3rd procedure, and the values of k_1 and k_2 are presented in **Table XI.**

Table XI Forchheimer empirical coefficients for Equation (2)

Test Number	Filter Number	Method 3 Forchheimer k_1 (m)	Method 3 Forchheimer k_2 (m^2)	Test Number	Filter Number	Method 3 Forchheimer k_1 (m)	Method 3 Forchheimer k_2 (m^2)
4	2-30 ppi	3.045E-08	4.404E-04	17	11-80 ppi	5.250E-09	8.819E-05
5	15-8 0ppi	6.166E-09	8.773E-05	18	12-80 ppi	7.786E-09	1.143E-04
6	14-80 ppi	6.762E-09	1.170E-04	19	13-50 ppi	1.679E-08	2.101E-04
7	4-50 ppi	1.551E-08	1.967E-04	20	16-80 ppi	6.543E-09	1.442E-04
8	4-50 ppi	2.326E-08	2.007E-04	21	17-50 ppi	2.537E-08	2.120E-04
9	20-50 ppi	1.710E-08	1.690E-04	22	17-50 ppi	1.629E-08	2.155E-04
10	20-50 ppi	1.525E-08	1.713E-04	23	18-30 ppi	5.572E-08	5.252E-04
11	1-30 ppi	3.656E-08	5.230E-04	24	19-40 ppi	3.099E-08	3.379E-04
12	3-50 ppi	1.296E-08	1.751E-04	25	21-80 ppi	5.441E-09	9.963E-05
13	5-50 ppi	1.477E-08	2.327E-04	26	22-30 ppi	5.084E-08	5.459E-04
14	6-50 ppi	1.381E-08	1.790E-04	27	23-50 ppi	1.568E-08	1.656E-04
15	7-50 ppi	1.814E-08	2.058E-04	28	24-80 ppi	6.519E-09	1.148E-04
16	8-50 ppi	2.229E-08	2.142E-04				

The average value of k_1 and k_2 for different types of filters are shown in **Table XII.**

Table XII Average value of k_1 and k_2 for different types of filters

Filter Type	Forchheimer k_1(m)	Forchheimer k_2 (m^2)
30 ppi	4.339E-08	5.086E-04
40 ppi	3.099E-08	3.379E-04
50 ppi	1.748E-08	1.960E-04
80 ppi	6.352E-09	1.094E-04

The k_1 and k_2 values from **Table XII** have been plotted in *Figure.34* and *Figure.35* as functions of the window area, $\pi d_w^2/4$.
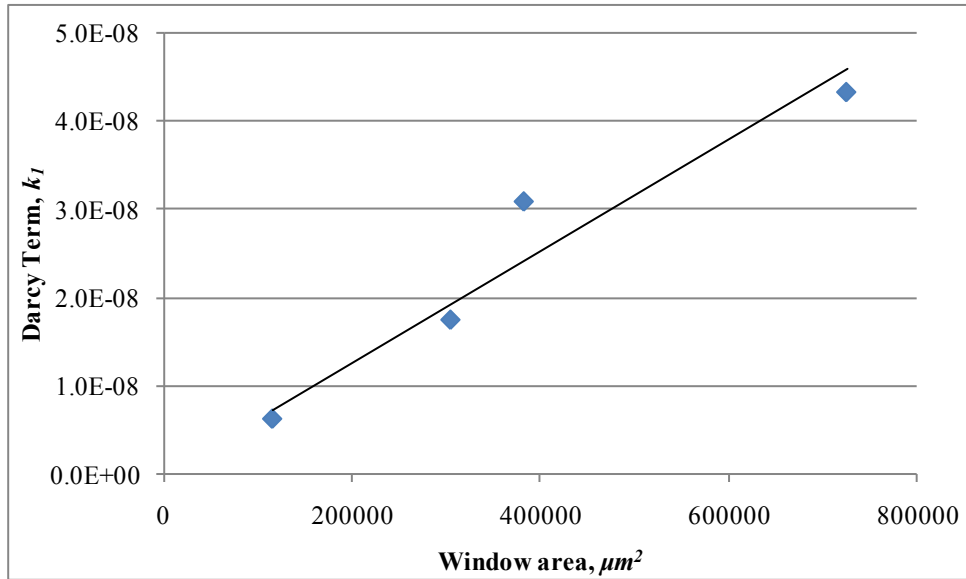
Figure.34 Correlation of Darcy term, k_1 [m^2] with window area.
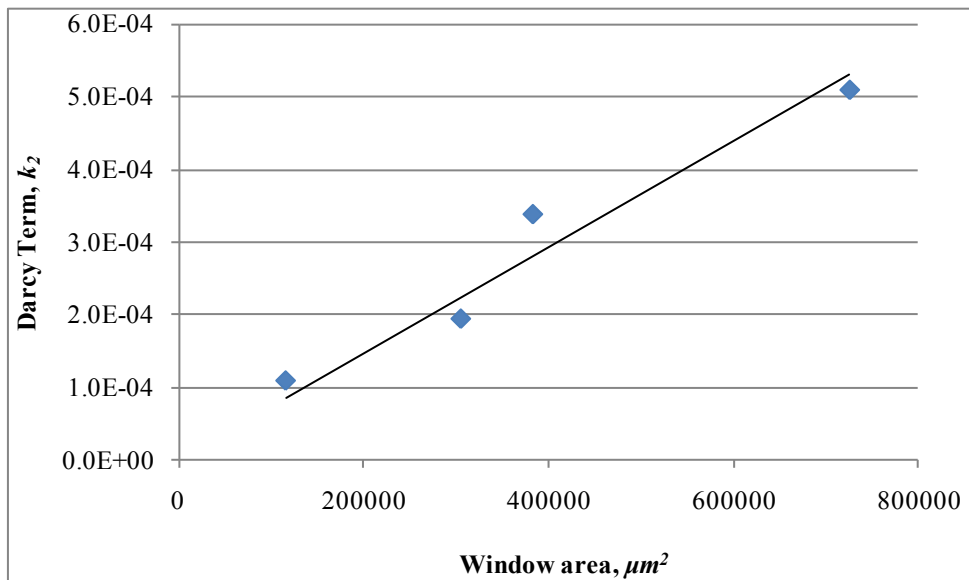
Figure.35 Correlation of Non-Darcy term, k_2 [m] with window area.

Empirical correlations have been developed for k_1 and k_2 as functions of the window diameter:

$$k_1 = \frac{6.34 \times 10^{-14} \pi d_w^2}{4}, \quad R^2 = 0.928 \qquad (37)$$

$$k_2 = \frac{7.31 \times 10^{-10} \pi d_w^2}{4}, \quad R^2 = 0.943 \qquad (38)$$

From *Figure.34*, and *Figure.35*, Equation (37) and (38), it is concluded that the Sivex® CFFs tested in these experiments behave like a series of 'orifices'. An examination of *Figure.36* would seem to support the concept of 'orifices', given the high percentage of closed windows, particularly at higher ppi's.
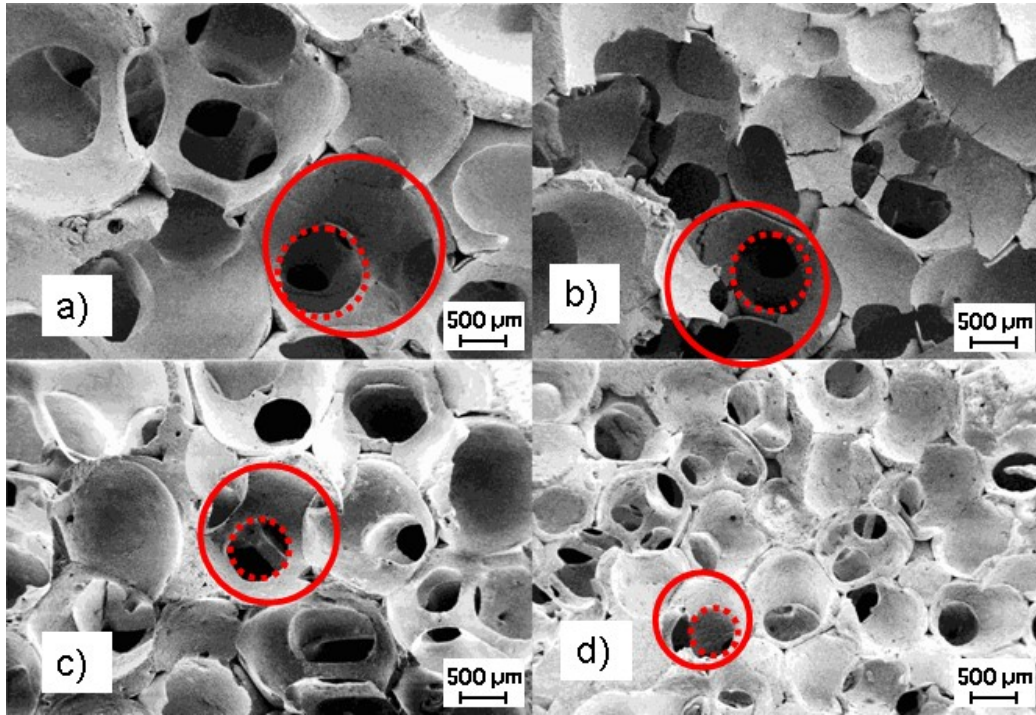
Figure.36 Representative SEM micrographs of 30 (a), 40 (b), 50 (c) and 80 (d) ppi Sivex® CFFs. Cell or pore sizes (d_c) are indicated by solid circles and window sizes (d_w) are indicated by dotted circles.

4.3.4 Correlation of Pressure Drop

Extensive work has been done to correlate the obtained results. All the equations listed in **Table II** were compared, and only Dietrich's equation (Equation 12) was found to adequately describe the data. Agreement is considered adequate being typically within $\pm 50\%$, except at very low velocity.

Other equations result in much lower estimates of pressure drop than the experimental data obtained using the final and well-sealed experimental procedure. Most previously published literature did not describe the details of the experiment procedures used, e.g. did they use a proper wall seal or correct for an expanding flow field? Since sealing arrangements and analysis techniques were generally not explained in sufficient detail, firm conclusions can not be drawn from comparisons with most of the previous studies.

The best empirical correlation obtained was a slightly modified version of Ergun's equation.

$$\frac{\Delta P}{L} = 8.385[150\frac{(1-\varepsilon)^2}{\varepsilon^3}\frac{\mu V_s}{d_w^2} + 1.75\frac{(1-\varepsilon)}{\varepsilon^3}\frac{\rho V_s^2}{d_w}], \;\; R^2 = 0.95 \qquad (39)$$

Equation (39) is plotted in ***Figure.37***, and comparison is made with 181 measurements. The

average absolute error is 10.7 %.
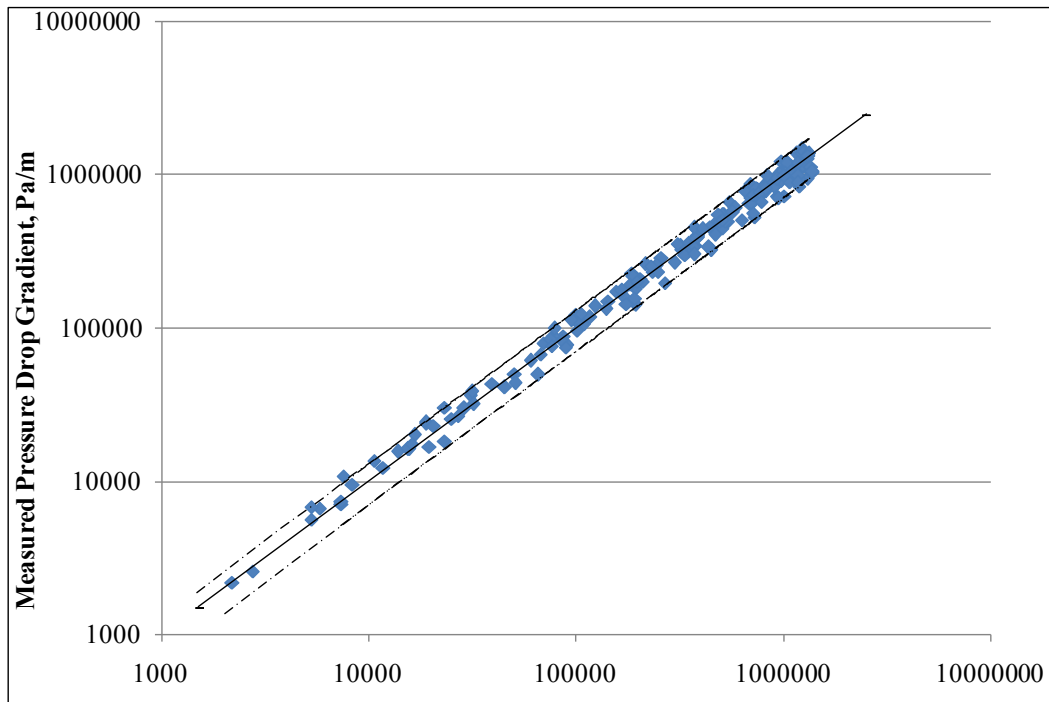
$$\frac{\Delta P}{L} = 8.385[150\frac{(1-\varepsilon)^2}{\varepsilon^3}\frac{\mu V_s}{d_w^2} + 1.75\frac{(1-\varepsilon)}{\varepsilon^3}\frac{\rho V_s^2}{d_w}]$$

Figure.37 Overall correlation Equation (39), comparison to the 181 measured pressure gradients for test 4-8, 11-22 and 26-28, the absolute average error is 10.7%. Dotted lines in the figure indicate a range of ±30%.

The Equation (39) is equivalent to using 23.4 and 2 (based on an average CFFs porosity of 88%), as the empirical constants, instead of the values 110 and 1.45 in Dietrich's Equation (12) or the Ergun equivalent values of 66.7 and 1.17 from Equation (11):

$$\frac{\Delta P}{L} = 23.4\frac{\mu V_s}{\varepsilon d_h^2} + 2\frac{\rho V_s^2}{\varepsilon^3 d_h} \qquad (40)$$

Applying Equation (40) to the obtained data indicates a significant reduction in error compared with the original Equation (11), especially at low velocity. The overall error is reduced from ~40% to ~30%.

Attempts were made to use cell diameter, strut diameter and tortuosity in various correlations; however, no improvement could be made over the accuracy of Equation (39) or (40).

4.3.5 Permeability of Different Filters with the Same ppi.

Experiments 5, 6, 17, 18 and 20 all used 80 ppi filters-15-80 ppi, 14-80 ppi, 11-80 ppi, 12-80 ppi and 16-80 ppi. The filter sections were cut from the middle of 5 different filters, at position No.6, as shown in *Figure.25*. The 3-50 ppi, 13-50 ppi and 17-50 ppi filter sections were all cut from the corners of 3 different filters, at position No.1 as shown in *Figure.25*, and these filters were used in experiments 12, 19 and 21. The pressure drop values obtained from these experiments are plotted in *Figure.38*, and *Figure.39*.
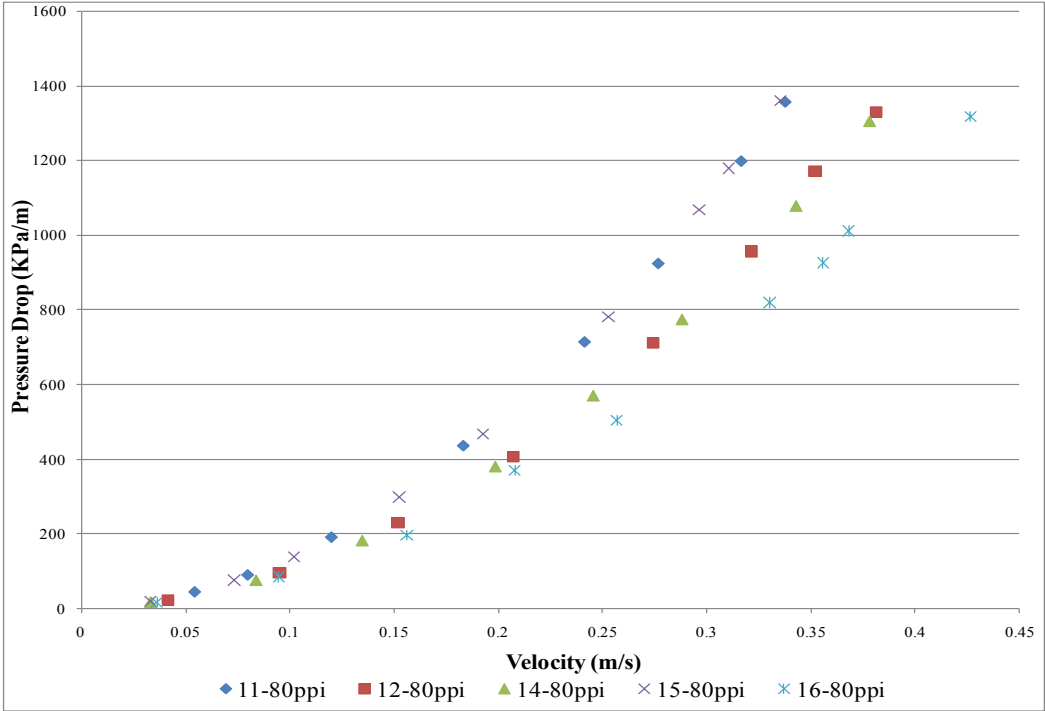
Figure.38 Pressure drop data from experiments 5, 6, 17, 18 and 20, filters were all cut from the middle, at position number: 6.
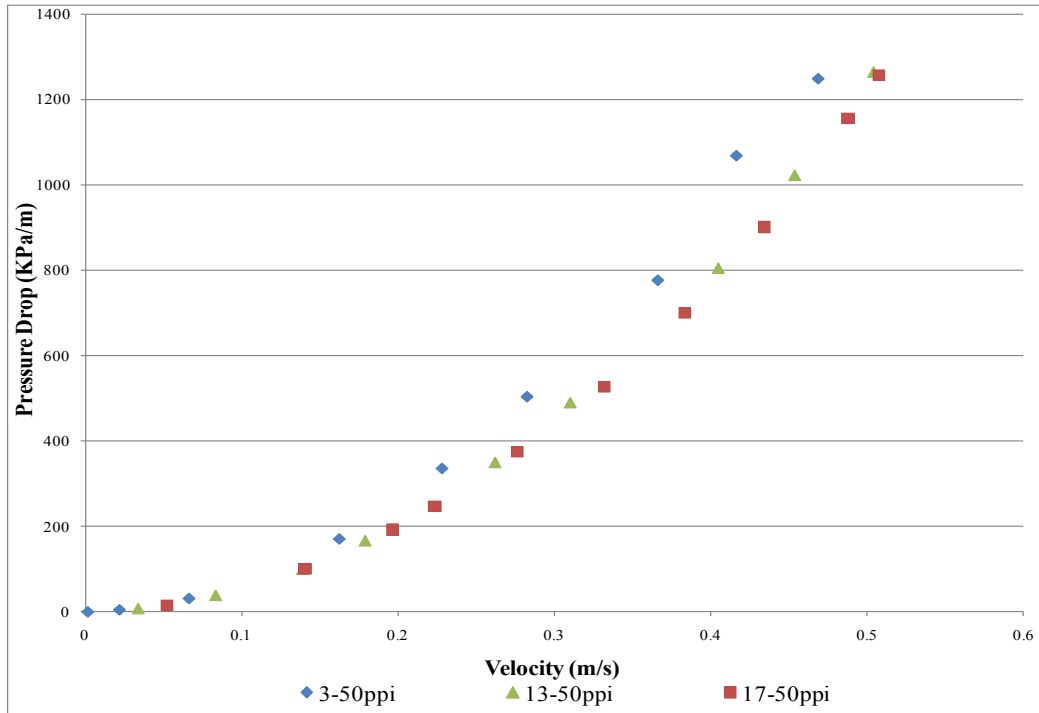
Figure.39 Pressure drop data from experiments 12, 19, and 21, filters were all cut from the middle, at position number 6.

The regressions of the experimental data are shown below:

$$11\text{-}80 \text{ ppi}: y = 11331160.53x^2 + 219330x, R^2 = 0.99984 \qquad (41)$$

$$12\text{-}80 \text{ ppi}: \quad y = 8750834.44x^2 + 176662x, R^2 = 0.99991 \qquad (42)$$

$$14\text{-}80 \text{ ppi}: \quad y = 8549569.55x^2 + 207140x, R^2 = 0.99989 \qquad (43)$$

$$15\text{-}80 \text{ ppi}: y = 11397513.56x^2 + 218830x, R^2 = 0.99991 \qquad (44)$$

$$16\text{-}80 \text{ ppi}: \quad y = 6931935.47x^2 + 203475x, R^2 = 0.99931 \qquad (45)$$

$$3\text{-}50 \text{ ppi}: \quad y = 5709968.14x^2 + 107650x, R^2 = 0.99970 \qquad (46)$$

$$13\text{-}50 \text{ ppi}: \quad y = 4758591.52x^2 + 82210x, R^2 = 0.99991 \qquad (47)$$

$$17\text{-}50 \text{ ppi}: \quad y = 4716067.55x^2 + 48920x, R^2 = 0.99994 \qquad (48)$$

It can be found that the regressions of the same ppi filters are not similar. 11-80 ppi, 15-80 ppi and 3-50 ppi filters gave higher pressure drop than other filters with same ppi during the test, and the pressure drop value of 16-80 ppi filter is much smaller than the rest 80PPI filters.

48

The k_1 and k_2 values in Equation (2) of these filters are shown in **Table XIII**.

Table XIII k_1 and k_2 values

Test Number	Filter Number	k_1 (m)	k_2 (m^2)
17	11-80 ppi	5.250E-09	8.819E-05
18	12-80 ppi	7.786E-09	1.143E-04
6	14-80 ppi	6.762E-09	1.170E-04
5	15-80 ppi	6.166E-09	8.773E-05
20	16-80 ppi	6.543E-09	1.442E-04
12	3-50 ppi	1.296E-08	1.751E-04
19	13-50 ppi	1.679E-08	2.101E-04
21	17-50 ppi	2.537E-08	2.120E-04

It is clear that the 16-80 ppi filter has a significantly higher k_2 value than other 80 ppi filters. The 16-80 ppi filter had the lowest measured pressure drop for this type of filter, since the pressure drop is inversely proportional to the value of k_1 and k_2, and k_2 is dominant at high velocity, i.e. the velocities of primary interest in this study. Filters 11-80 ppi, 15-80 ppi and 3-50 ppi have lower k_2 values and gave higher pressure drops. It should be noted that the difference between 17-80 ppi and 18-80 ppi, 6-80 ppi and 16-80 ppi or 3-50 ppi and 13-50 ppi are much larger than any error that can be attributed to the experiment procedure and are therefore deemed to be caused by variation between the filters themselves.

Results between filters of the same ppi show some variability; however, results from each type of filter are statistically different that other types of filters.   This is shown in **Table XIV** by the comparison of the mean and upper and lower 95% confidence intervals for the 50 and 80 ppi filter types.

Table XIV Average k_1 and k_2 values and 95% confidence area

Filter Type	50 ppi	80 ppi
Average k_1 (m)	1.838E-08	6.501E-09
95% Confidence	5.570E-09	8.078E-10
Upper 95% Confidence	2.395E-08	7.309E-09
Lower 95% Confidence	1.281E-08	5.694E-09
Average k_2 (m^2)	1.991E-04	1.103E-04
95% Confidence	1.820E-05	2.060E-05
Upper 95% Confidence	2.173E-04	1.309E-04
Lower 95% Confidence	1.809E-04	8.967E-05

In conclusion, the permeability of filters with the same ppi are not identical. It is assumed that natural variation during the manufacturing process is responsible, and has resulted in variations in microstructure and tortuosity (e.g. greater or lesser numbers of blocked windows). Visual observation also finds clear differences between the filters, as shown in *Figure.40*.
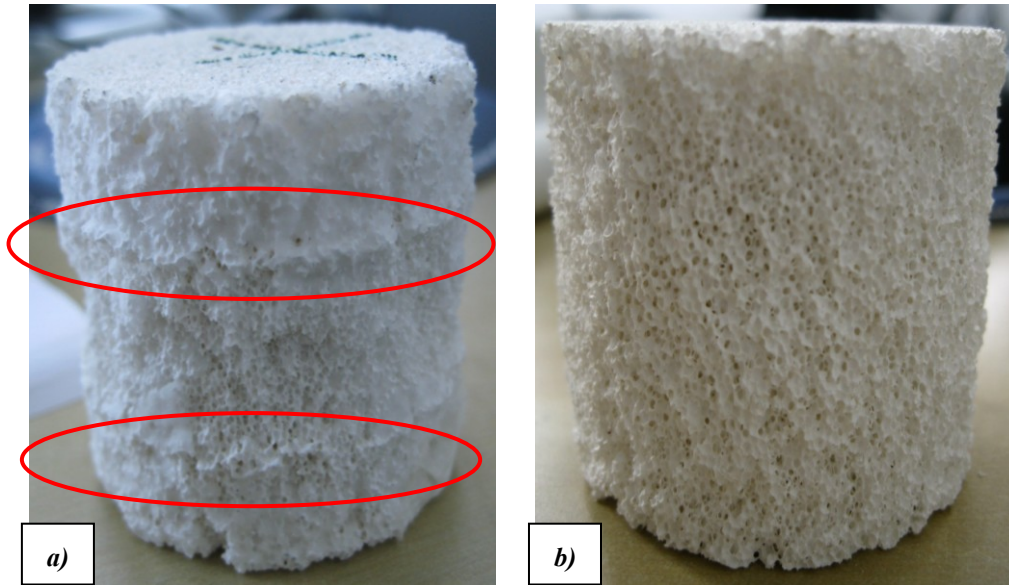
Figure.40 Photo of 11-80 ppi and 12-80 ppi filters

In *Figure.40*, it is clear that two filters look different, 11-80 ppi filter has two layers which are marked in the red circles. *Figure.41* shows the microstructure of the layers.
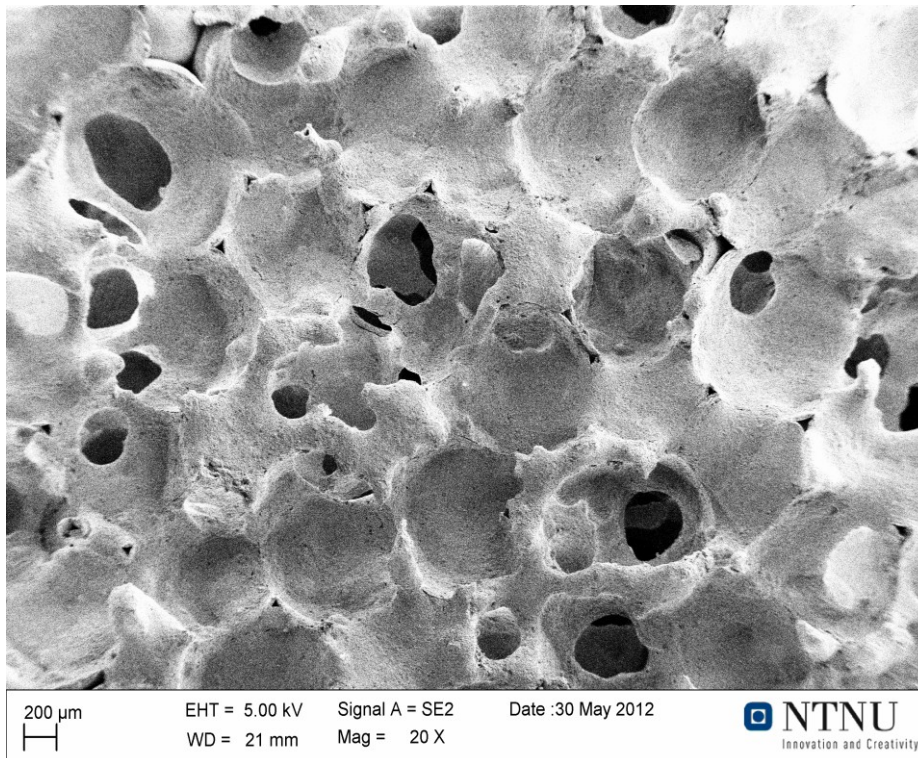
Figure.41 Representative SEM micrographs of 11-80 ppi CFF indicating nearly complete blockage of all windows.

From *Figure.41*, it can be found that in the 'lines' from *Figure.36* that most of the pores are closed, and this makes it difficult for liquid to flow through this region, resulting in a very low permeability and a very high pressure drop.

50

From above information, it is concluded that filters of the same ppi vary and that the permeability for each type of the filter must be defined in a 'statistical' manner, i.e. defined by mean, standard deviation and confidence intervals.

4.3.6 Permeability for Different Sample's taken from the Same Filter.

8 experiments were conducted to determine the relationship between permeability and sample position. These 8 experiment's numbers are 4, 7 and 11 through 16. The filters used are 1-30 ppi, 2-30 ppi, 3-50 ppi, 4-50 ppi, 5-50 ppi, 6-50 ppi, 7-50 ppi and 8-50 ppi. The position information of these filters is presented in **Table VII**. The experiment data are plotted in *Figure.42* and *Figure.43*.
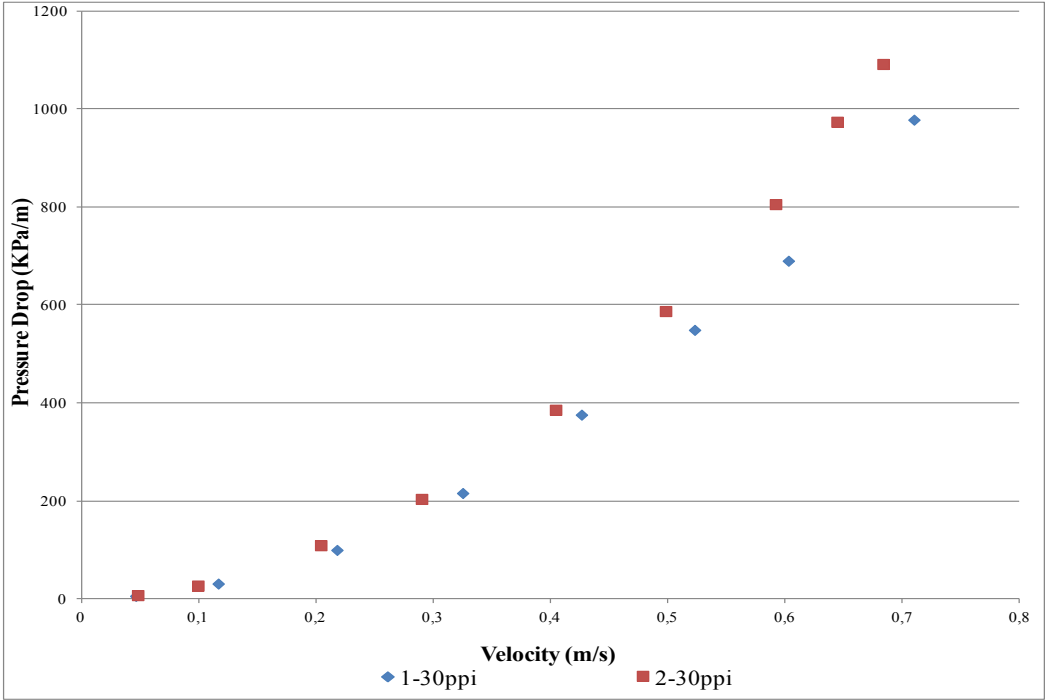
Figure.42 Pressure drop data for experiments 4 and 11, 1-30 ppi: position number 1, 2-30 ppi: position number 2.
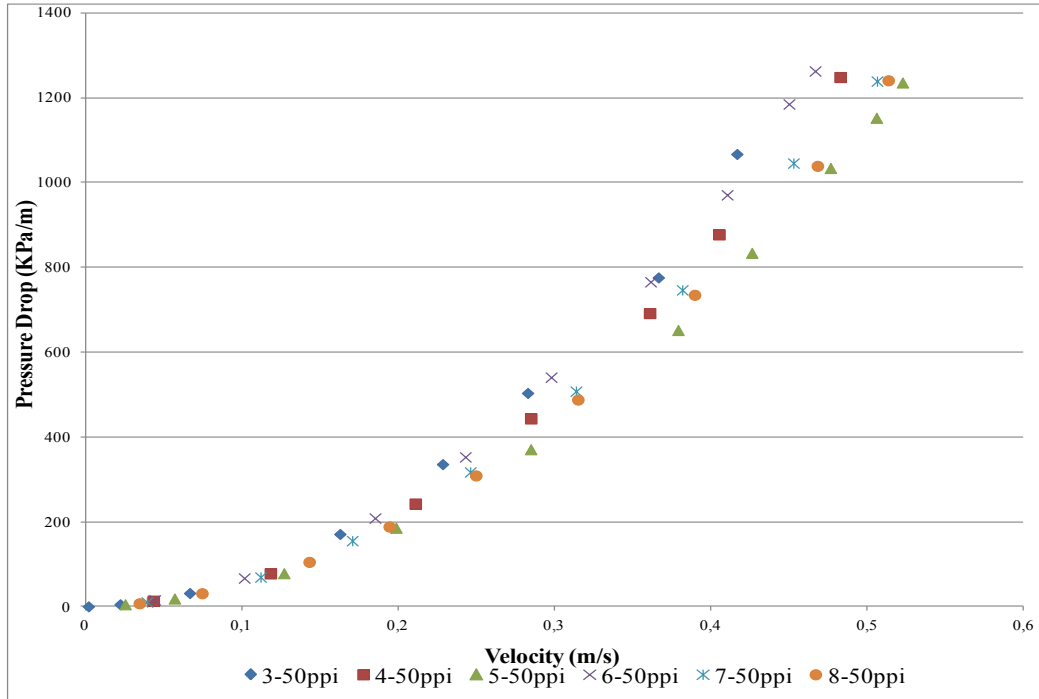
Figure.43 Pressure drop data for experiments 7 and 12-16, 3-50 ppi: position number 1, 4-50 ppi: position number 2, 5-50 ppi: position number 3, 6-50 ppi: position number 4, 7-50 ppi: position number6, 8-50 ppi: position number 5.

The regressions of the experimental data are shown below:

$$1\text{-}30 \text{ ppi: } \quad y = 1911934.44x^2 + 37360x, R^2 = 0.99984 \qquad (49)$$

$$2\text{-}30 \text{ ppi: } \quad y = 2270285.55x^2 + 45114x, R^2 = 0.99985 \qquad (50)$$

$$3\text{-}50 \text{ ppi: } y = 5709968.14x^2 + 107650x, R^2 = 0.99970 \qquad (51)$$

$$4\text{-}50 \text{ ppi: } \quad y = 5084123.17x^2 + 89000x, R^2 = 0.99973 \qquad (52)$$

$$5\text{-}50 \text{ ppi: } \quad y = 4297350.89x^2 + 92060x, R^2 = 0.99988 \qquad (53)$$

$$6\text{-}50 \text{ ppi: } y = 5586066.98x^2 + 100785x, R^2 = 0.99993 \qquad (54)$$

$$7\text{-}50 \text{ ppi: } \quad y = 4858509.54x^2 + 78150x, R^2 = 0.99990 \qquad (55)$$

$$8\text{-}50 \text{ ppi: } \quad y = 4667185.24x^2 + 61325x, R^2 = 0.99992 \qquad (56)$$

It can be found that the regressions of the same ppi filters are not similar. 2-30 ppi which cut from the centre of the filter gave a higher pressure drop than 1-30 ppi cut from the corner. For 50 ppi tests, 3-50 ppi cut from the corner of the filter has the highest pressure drop.

The k_1 and k_2 values in Equation (2) of these filters are shown in **Table XV**.

Table XV k_1 and k_2 values

Test Number	Filter Number	k_1 (m)	k_2 (m^2)
11	1-30 ppi	3.656E-08	5.230E-04
4	2-30 ppi	3.045E-08	4.404E-04
12	3-50 ppi	1.296E-08	1.751E-04
7	4-50 ppi	1.551E-08	1.967E-04
13	5-50 ppi	1.477E-08	2.327E-04
14	6-50 ppi	1.381E-08	1.790E-04
15	7-50 ppi	1.814E-08	2.058E-04
16	8-50 ppi	2.229E-08	2.142E-04

From above information it is concluded that the permeability of the filters vary both within a given filter and even more between filters for a given ppi. There appears to be no correlation between position number and permeability, i.e. the variations appear to be random in nature.

4.3.7 Permeability Changing with Fluid Flow Direction

Acosta[9] tested his filters in both the forward and reverse directions finding identical results. In this study, two experiments were conducted to verify that flow direction would not alter the pressure drop for well sealed filters. These two tests are experiments 21 and 22, and the filter section used was 17-50 ppi. The experimental data is shown in *Figure.44*.
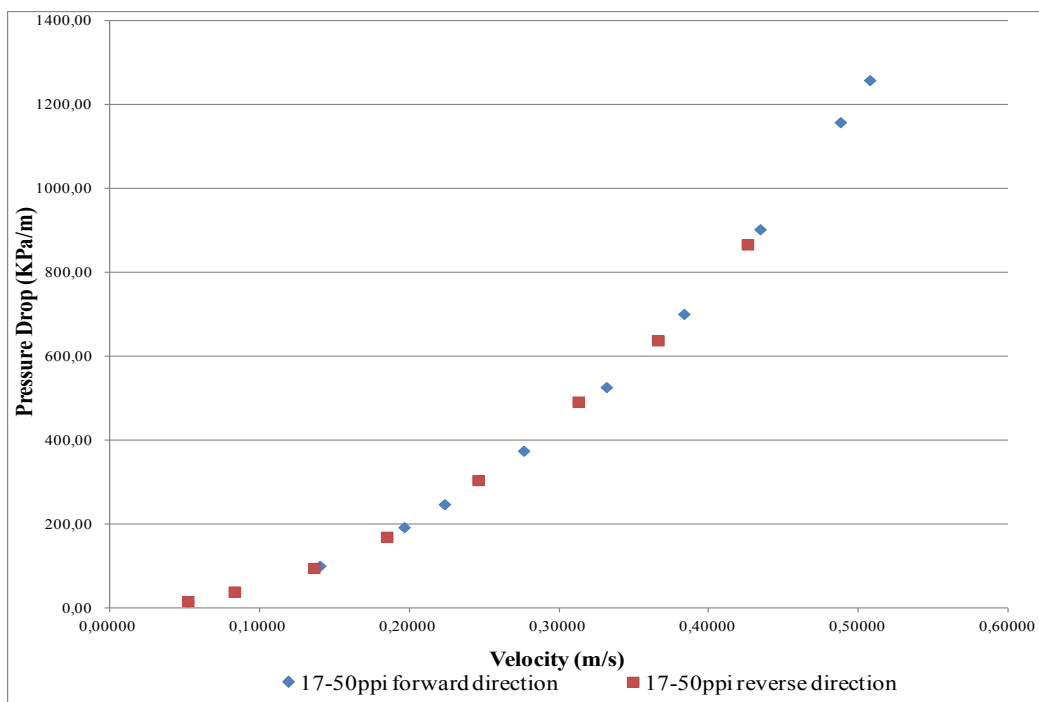
Figure.44 Pressure drop data for experiments 21 and 22, position number: 1.

53

The regressions of the experimental data are:

17-50 ppi forward direction: $y = 4716067.55x^2 + 48920x, R^2 = 0.99994$ (57)

17-50 ppi reverse direction: $y = 4639062.59x^2 + 76410x, R^2 = 0.99982$ (58)

From *Figure.44*, it can be seen that the experimental data of two tests are nearly identical. The Equation (57) is also very similar to Equation (58), especially the second order term. The difference of the second order term is about 1.6%, this different maybe caused by the accuracy of the experiment. Since the error of the pressure drop obtained by the apparatus in this study is ±31.25 *Pa*, thus it will give more errors at very low velocity. This can explain why there is a higher difference in the first order term. **Table XVI** shows the k_1 and k_2 values that calculated by these two tests.

Table XVI k_1 and k_2 values

Test Number	Filter Number	k_1 (m)	k_2 (m^2)
21	17-50 ppi	2.537E-08	2.120E-04
22	17-50 ppi	1.629E-08	2.155E-04

Again, very similar k_2 values were obtained from these two tests. Larger differences were seen in k_1 values, which maybe caused by the precision error of the experimental pressure measuring equipment.

It can be concluded that the permeability of CFF will not change by the changing of fluid flow direction.

4.4 Filter Tortuosity

Filter tortuosity has been determined for metal impregnated 30, 40, 50 and 80 ppi filters. Measurements have been obtained with the metal in both liquid and solid states. The metal used was 'commercially' pure electrical grade aluminium, which was determined to have 61.7±0.1% IACS conductivity (average of 10 readings) prior to melting. After melting, the solidified metal samples were found to have conductivities of 59.7% (30 ppi), 54.0% (40 ppi), 60.0% (50 ppi) and 61.0% (80 ppi). The hot metal experiments were conducted using the apparatus already shown in *Figure. 21*.

Hot liquid metal and cold solid filter section measurements (average, vertical and horizontal cuts) and calculated tortuosity results (using the hot metal data) are summarized in **Table XVII**[66], for all four filter types. Experimental data have also been plotted in *Figure.45*.

Table XVII Summary of key tortuosity experimental results

Filter Type (opi)	Filter Porosity	Filter Tortuosity	FEM Estimate of Conductivity Ratio (σ_m/σ_f)	Cold Average Conductivity Ratio (σ_m/σ_f)	Cold Vertical Conductivity Ratio (σ_m/σ_f)	Cold Horizontal Conductivity Ratio (σ_m/σ_f)
30	0.892	1.30	1.40±0.06	1.70	1.64	1.77
40	0.900	2.29	2.54±0.18	2.15	2.27	2.02
50	0.863	2.19	2.54±0.12	2.70	2.34	3.05
80	0.865	3.20	3.70±0.06	2.79	2.91	2.66
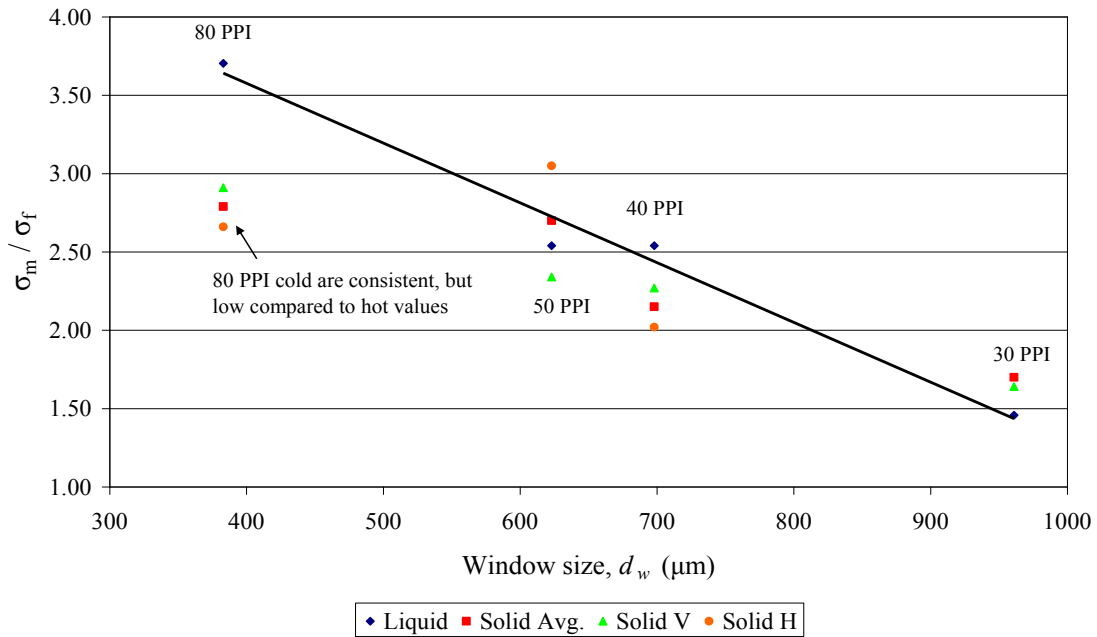
Figure.45 Conductivity ratio of metal (σ_m) and metal impregnated filter (σ_f) versus window size (d_w) [μm]. Comparison is shown between liquid metal values fitted to experimental data using FEM and average, vertical, and horizontally cut solid filter sections (cold readings).[66]

Results show reasonable agreement between hot and average cold conductivity ratio's, given the different equipment, temperatures and frequencies involved in these two sets of measurements. The conductivity ratio between the metal and metal impregnated filters for the liquid metal experiments was correlated according to the following equation:

$$\frac{\sigma_m}{\sigma_f} = 5.10 - 3.8 \ 10^3 d_w, \ R^2 = 0.981 \tag{59}$$

No correlation could be found between the horizontal or vertical cuts. The observed variations may the result of the random location of the sections through the pore structure of the filter elements and the low electromagnetic penetration depth of the high frequency cold method, which is less than one cell diameter.

Few measured values have been published previously for tortuosity. Moreia *et al.* measured tortuosity values using an ionic conduction method equivalent to the induction method described here. Their values for CFFs of 8, 20 and 45 ppi were 1.68, 1.71 and 1.84 respectively.[82] Diedericks *et al.* have theoretically studied tortuosity in some detail, proposing a value of ~1.45 at ε=0.88, for 'foam like' materials.[83] In P. Habisreuther *et al.*, tortuosity has been numerically estimated for high porosity (ε=0.720) 'solid sponges' material to be 1.317.[63] Methods using water and ionic solutes, will likely underestimate the true filter tortuosity, due to penetration of the water and ions into the micro and nano-porosity of the filter structure itself. Liquid metal poorly wets the surface of the ceramic and in the absence of intense pressure (e.g. 4000 Bar) will not penetrate the micro porosity.

Chapter 5

CFD Modelling

5.1 Introduction

Computational fluid dynamics (CFD) was used in this study to verify the experimental data for the 49 *mm* filter design and to compute 'effective' flow field diameter for 101 *mm* design.

To compute the 'effective' flow field diameter for 101 *mm* design, an 'effective' flow field diameter was initially guessed for use with Equation (2), the resulting k_1 and k_2 terms were then used with the CFD model and the pressure gradient determined. If the results were in error, a new 'effective' diameter was guessed and the procedure repeated until convergence was achieved. ***Figure.46*** shows this procedure.

Measure: ΔP, Diameter, *L*, Mass Flow,
Temperature (i.e. μ and ρ)
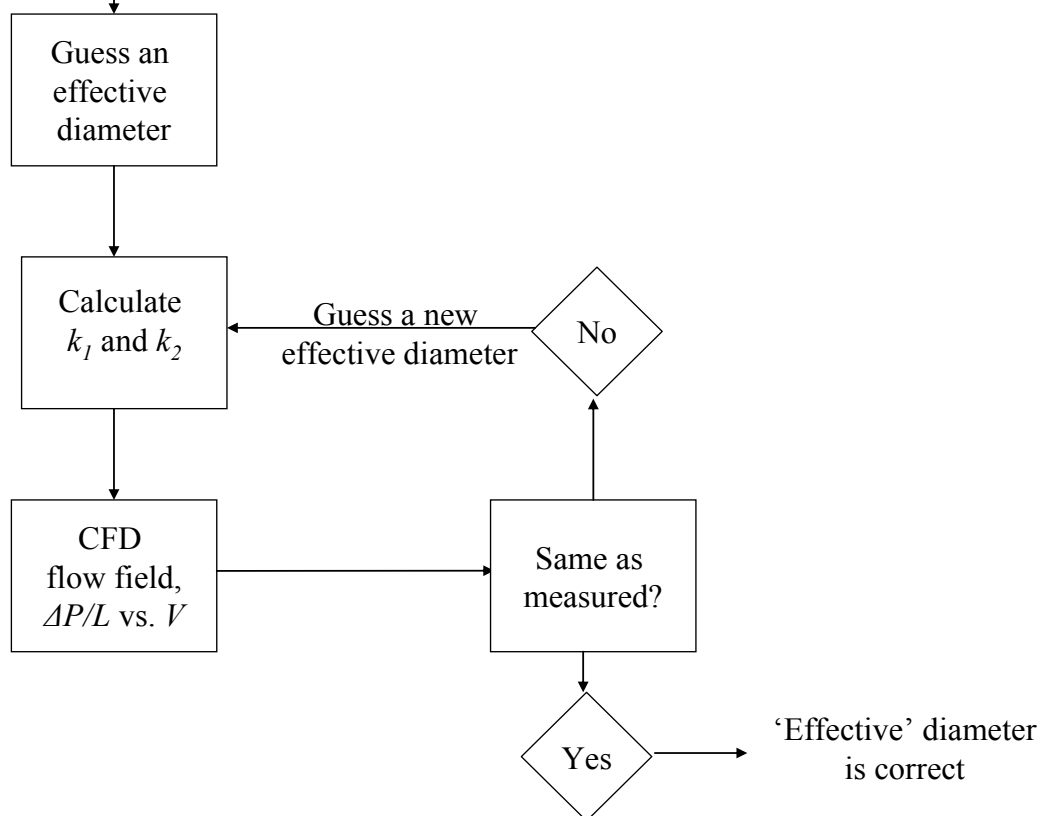
Figure.46 FEM CFD procedure applied to the 101 mm experimental results to determine the Forchheimer, Equation (2), parameters k_1 and k_2.

5.2 Theory

5.2.1 Materials

The COMSOL® material data 'water, liquid' was used for the fluid properties in these simulations. A new material called 'filter' was built in manually for the filter domain, containing the actual Darcy permeability and filter porosity.

The equation used to calculate the water dynamic viscosity in the COMSOL is[84]:

$$\mu = 1.3799566804 - 0.021224019151T + 1.3604562827 \times 10^{-4}T^2 - 4.6454090319 \times 10^{-7}T^3$$
$$+ 8.9042735735 \times 10^{-10}T^4 - 9.0790692686 \times 10^{-13}T^5 + 3.8457331488 \times 10^{-16}T^6 \qquad (60)$$

The equation for water density is:

$$\rho = 838.466135 + 1.40050603T^1 - 0.0030112376T^2 + 3.71822313 \times 10^{-7}T^3 \qquad (61)$$

Temperature for use with Equations (60) and (61) were the actual average temperature measured during each experiment.

The density and dynamic viscosity for the filter was the actual average water density and dynamic viscosity from each experiment, entered manually. The porosities of the filters are present in **Table VIII**.

5.2.2 Physics

This section has been extracted in large part from the documentation supplied by COMSOL® and the associated references.

There are two physics used in the modelling, "Free and Porous Media Flow *(fp)*" for the filter and "Turbulent Flow, k-ε *(spf)*" for the pipe before and after the filter, covering the length of the filter holder apparatus.

- Free and Porous Media Flow

The free and porous media flow interface uses the Navier-Stokes equations for describing the flow in open regions, and the Brinkman equations are used for the flow in porous regions.[84]

The Navier-Stokes equation for incompressible flow is[85]:

$$\rho(\frac{\partial V}{\partial t} + V \cdot \nabla V) = -\nabla P + \mu \nabla^2 V + f \tag{62}$$

Where V is the superficial flow velocity [m/s], P is the pressure [Pa], ∇^2 is the vector Laplacian and f represents 'other' body forces (per unit volume) acting on the fluid, such as gravity or centrifugal force.

The Brinkman equations are:

$$\frac{\partial}{\partial t}(\varepsilon\rho) + \nabla \cdot (\rho V) = Q_{br} \tag{63}$$

$$\frac{\rho}{\varepsilon}[\frac{\partial V}{\partial t} + (V \cdot \nabla)\frac{V}{\varepsilon}] = -\nabla P + \nabla\left\{\frac{1}{\varepsilon}[\mu(\nabla V + (\nabla V)^T - \frac{2}{3}\mu(\nabla \cdot V)I]\right\}$$
$$-(\frac{\mu}{k_1} + Q_{br})V + F \tag{64}$$

$$V_i = \frac{V}{\varepsilon} \tag{65}$$

Where Q_{br} is a mass source or mass sink [kg/m^{3}s], which is zero in case of these experiments and F is the force term [kg/m^{2}s^2], this term is negligible (but non-zero) in this study, due to the experimental equipment being positioned horizontal. V_i is the interstitial velocity within the pores of the filter [m/s].

The Forchheimer drag option was added manually to the model and this option adds a viscous force proportional to the square of fluid velocity, see Equation (2). So Equation (64) can be written as:

$$\frac{\rho}{\varepsilon}[\frac{\partial V}{\partial t} + (V \cdot \nabla)\frac{V}{\varepsilon}] = -\nabla P + \nabla\left\{\frac{1}{\varepsilon}[\mu(\nabla V + (\nabla V)^T - \frac{2}{3}\mu(\nabla \cdot V)I]\right\}$$
$$-(\frac{\mu}{k_1} + \frac{\rho}{k_2}V)V \tag{66}$$

Since the fluid is incompressible, the density is constant, so:

$$\frac{\partial}{\partial t}(\varepsilon \rho) + V \cdot \nabla \rho = 0 \tag{67}$$

Combine Equation (66) with Equation (67) get:

$$\frac{\rho}{\varepsilon}[(V \cdot \nabla)\frac{V}{\varepsilon}] = -\nabla P + \nabla \left\{ \frac{1}{\varepsilon}[\mu(\nabla V + (\nabla V)^T - \frac{2}{3}\mu(\nabla \cdot V)I] \right\}$$
$$-(\frac{\mu}{k_1} + \frac{\rho}{k_2}V)V \tag{68}$$

- Turbulent Flow, k-ε *(spf)*

As mentioned before, the fluid flow regimes experienced during the experiments included laminar flow, transitional flow and complete turbulent flow. The maximum velocity experienced in the filter during the experiment was ~0.8 *m/s*, and the Reynolds number, *Re* is ~26000. Since the *Re* is not large, the "Low Reynolds Number k-ε Turbulence Model" was chose for this modelling.

The flow fluid is incompressible and Newtonian, so Equation (62) can be written as:

$$\rho \frac{\partial V}{\partial t} + \rho V \cdot \nabla V = \nabla[-P + \mu(\nabla V + (\nabla V)^T] + F \tag{69}$$

$$\rho \nabla \cdot V = 0 \tag{70}$$

If the flow is turbulent, then all quantities fluctuate in time and space.[84] It is seldom worth the extreme computational resources required to obtain details about the turbulent fluctuations in time. A time averaged representation often provides sufficient information about the flow.

The Reynolds-averaged representation of turbulent flows divides the flow quantities into an averaged value and a fluctuation part,

$$\phi = \phi + \phi' \tag{71}$$

Where ϕ represent any scalar quantity of the flow. The mean value can vary in space and time generally. An example is shown for the fluid velocity in *Figure.47*[84], shows time averaging of one component of the velocity vector for non-stationary turbulence. The unfiltered flow has a time scale Δt_1. After a time filter with width $\Delta t_2 >> \Delta t_1$ has been applied, there is a fluctuation part, u'_i, and an average part, U_i. Because the flow field also

varies on a time scale longer than Δt_2, U_i is still time dependent but is much smoother than the unfiltered velocity u_i.
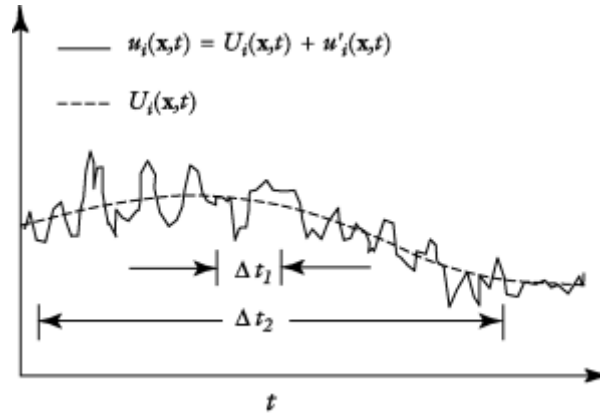
Figure.47 The unfiltered velocity component u_i, with a time scale Δt_1, and the averaged velocity component, U_i, with time scale Δt_2.

With Reynolds-averaging, Equation (69) can be re-written as:

$$\rho\frac{\partial V}{\partial t} + \rho V \cdot \nabla V + \nabla \cdot \overline{(\rho u' \otimes u')} = \nabla[-P + \mu(\nabla V + (\nabla V)^T] + F \quad (72)$$

Where V is the averaged velocity field and $\otimes$ is the outer vector product. Compared with Equation (69), only the last term on the left side is different. This term represents the interaction between the fluctuating velocities, called the Reynolds stress tensor.

Assuming the turbulence to be of a purely diffusive nature, the deviating part of the Reynolds stress is expressed by:

$$\nabla \cdot \overline{(\rho u' \otimes u')} - \frac{\rho}{3} tracc\overline{(u' \otimes u')} = -\mu_T(\nabla V + (\nabla V)^T) \quad (73)$$

Where μ_T is the eddy viscosity, which is also called turbulent viscosity. The spherical part can then be written as:

$$\frac{\rho}{3} tracc\overline{(u' \otimes u')} = \frac{2}{3}\rho k \quad (74)$$

where k is the turbulent kinetic energy. When simulating incompressible flows, this term is included in the pressure, but in compressible flows, this term must be explicitly included.

"The Low Reynolds Number k-ε Turbulence Model" introduces two dependent variables: the turbulent kinetic energy, k, and the dissipation rate of turbulent energy, ε.[86]

The transport equation for k is[86]:

$$\rho\frac{\partial k}{\partial t} + \rho V \cdot \nabla k = \nabla \cdot [(\mu + \frac{\mu_T}{\sigma_k})\nabla k] + P_k - \rho\varepsilon \qquad (75)$$

The transport equation for ε is[87]:

$$\rho\frac{\partial \varepsilon}{\partial t} + \rho V \cdot \nabla \varepsilon = \nabla \cdot [(\mu + \frac{\mu_T}{\sigma_k})\nabla \varepsilon] + C_{\varepsilon 1}\frac{\varepsilon}{k}P_k - f_\varepsilon C_{\varepsilon 2}\rho\frac{\varepsilon^2}{k} \qquad (76)$$

Where:

$$P_k = \mu_T \left\{ \nabla V : [\nabla V + (\nabla V)^T] - \frac{2}{3}(\nabla \cdot V)^2 \right\} - \frac{2}{3}\rho k \nabla \cdot V$$

$$\mu_T = \rho f_\mu C_\mu \frac{k^2}{\varepsilon}$$

$$f_\mu = \left(1 - e^{-l^*/14}\right)^2 \left(1 + \frac{5}{R_t^{3/4}}e^{-(R_t/200)^2}\right)$$

$$f_\varepsilon = \left(1 - e^{-l^*/3.1}\right)^2 \left(1 - 0.3e^{-(R_t/6.5)^2}\right)$$

$$l^* = (\rho V_\varepsilon l_\varepsilon)/\mu$$

$$R_t = \rho k^2 / (\mu\varepsilon)$$

$$V_\varepsilon = (\mu\varepsilon/\rho)^{1/4}$$

$C_{\varepsilon 1}$=1.5, $C_{\varepsilon 2}$=1.9, C_μ=0.09, σ_k=1.4, σ_ε=1.4 and l_w is the distance to the closest wall.

The damping terms in the equations for k and ε allows a no slip condition to be applied to the velocity, so V=0. Since all velocity must disappear on the wall, so k=0 on the wall.

The boundary condition for ε is:

$$\varepsilon = 2\frac{\mu}{\rho}\frac{k}{l_w^2} \qquad (77)$$

5.2.3   Modelling Approach

Some pertinent points to achieving adequate agreement between CFD, analytical models and measured values were:

- Iteration between high quality measurements and FEM to ensure validity of assumptions and accuracy of final models.
- Correct and validated boundary conditions, e.g.:   no-slip walls, contiguous velocity fields between liquid and porous media domains, and the inlet velocity profile.
- Use of the low Reynolds number *k-ε,* Reynolds Averaged Navier Stokes (RANS) model for turbulence ($k_0 = 0.005$ m^2/s^2 and $\varepsilon_0 = 0.005$ m^2/s^3), to adequately cover the difficult range of velocities in the inlet region.
- Use of dense meshes in regions of high velocity gradients (e.g. boundary mesh at the 'no-slip' walls).
- Precise measurement and exact geometric reproduction of the actual apparatus.

5.3 FEM Model Details

5.3.1 49 *mm* Filter Finite Element Modelling

Figure.48 shows the geometry of the model for the 49 *mm* diameter filter holder apparatus.
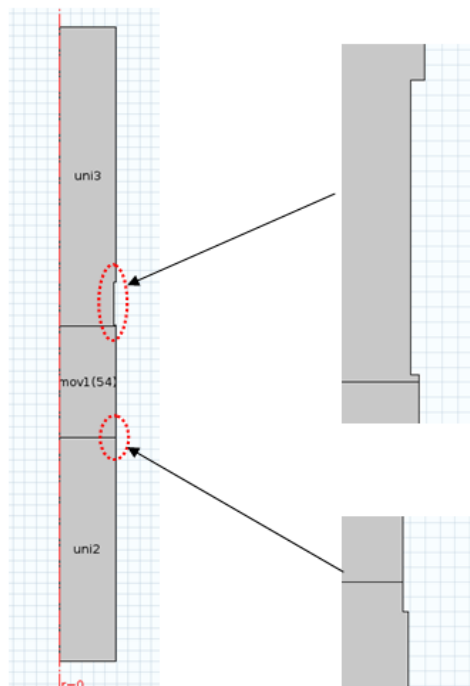
Figure.48 Modelling geometry of 49 mm filter holder apparatus.

The mesh used in the FEM model is shown in *Figure.49*.
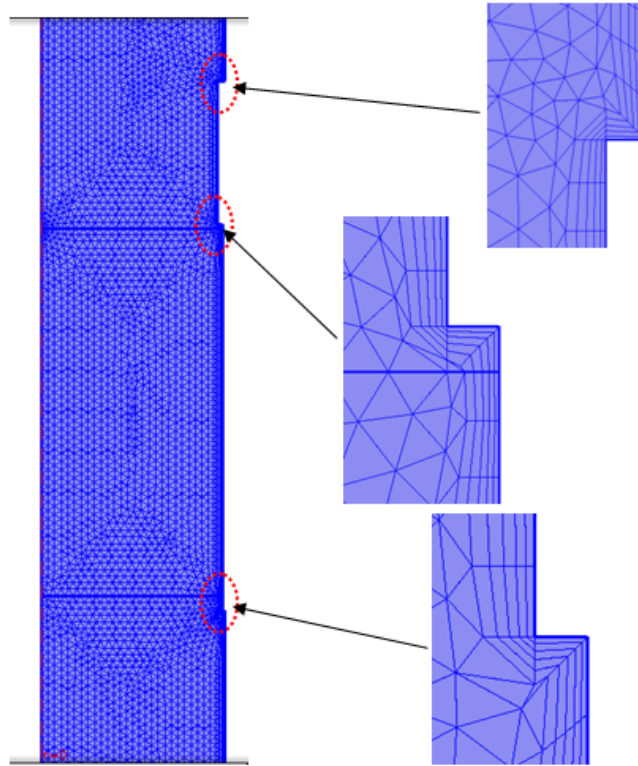
Figure.49 Modelling mesh used for the 49 mm filter apparatus.

Figure.50 and *Figure.51* show the flow fields and the pressure gradients for the 49 *mm* diameter filter apparatus at 7 ^{o}C and 0.054 *m/s* inlet water velocity. The filter properties used in this simulation are those of 23-50 ppi's as shown in **Table VIII**.

Please note in *Figure.50* and *Figure.51* that the flow field is contiguous over the boundary between the turbulent fluid and porous media domains. This required some careful manipulation of the FEM model in COMSOL[®], to force iteration between the inlet and outlet conditions over these boundaries.
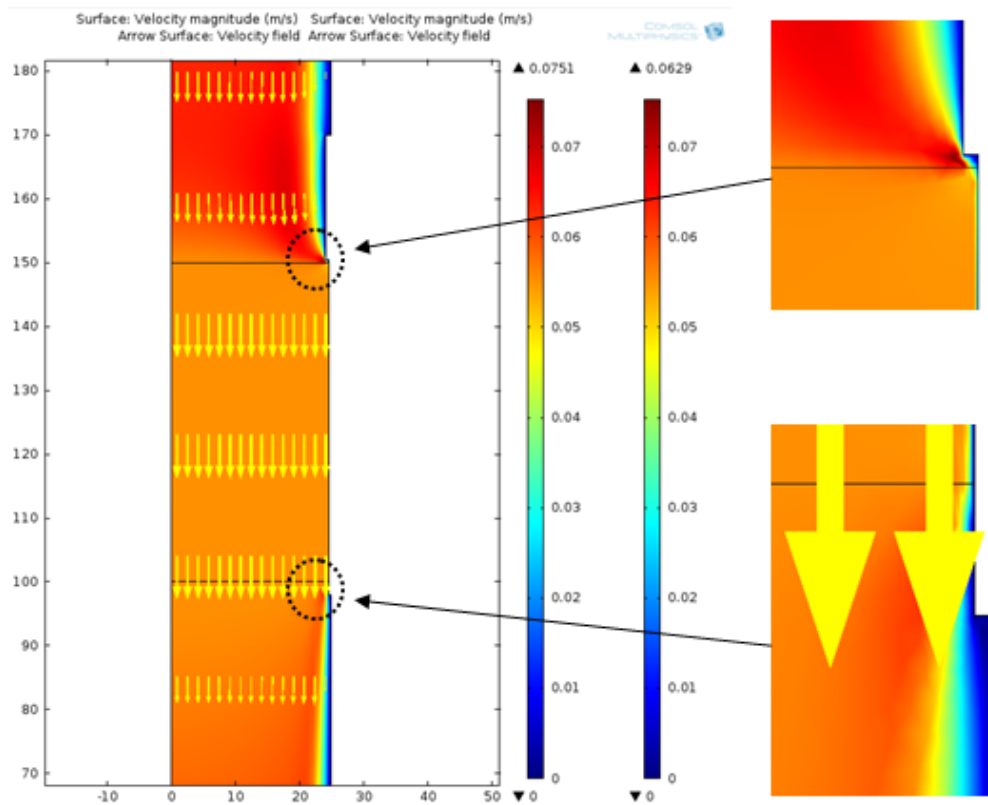
Figure.50 The flow field for the 49 mm diameter filter apparatus. The inlet velocity is 0.054 m/s, filter number is 23-50 ppi.
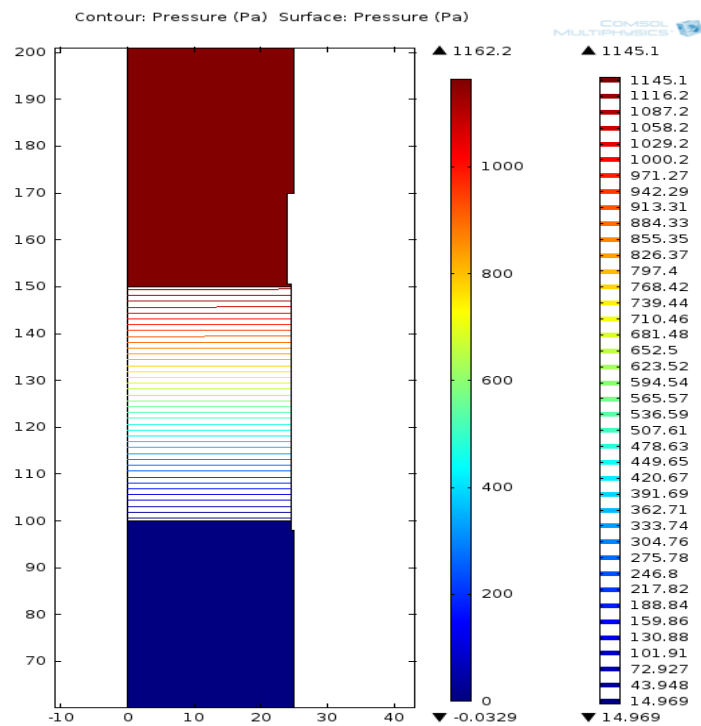
Figure.51 The pressure gradient for the 49 mm diameter filter apparatus. The inlet velocity is 0.054 m/s, filter number is 23-50 ppi.

5.3.2 101*mm* Filter Finite Element Modelling

Figure.52 shows the geometry of the model for the 101 *mm* diameter filter holder apparatus.
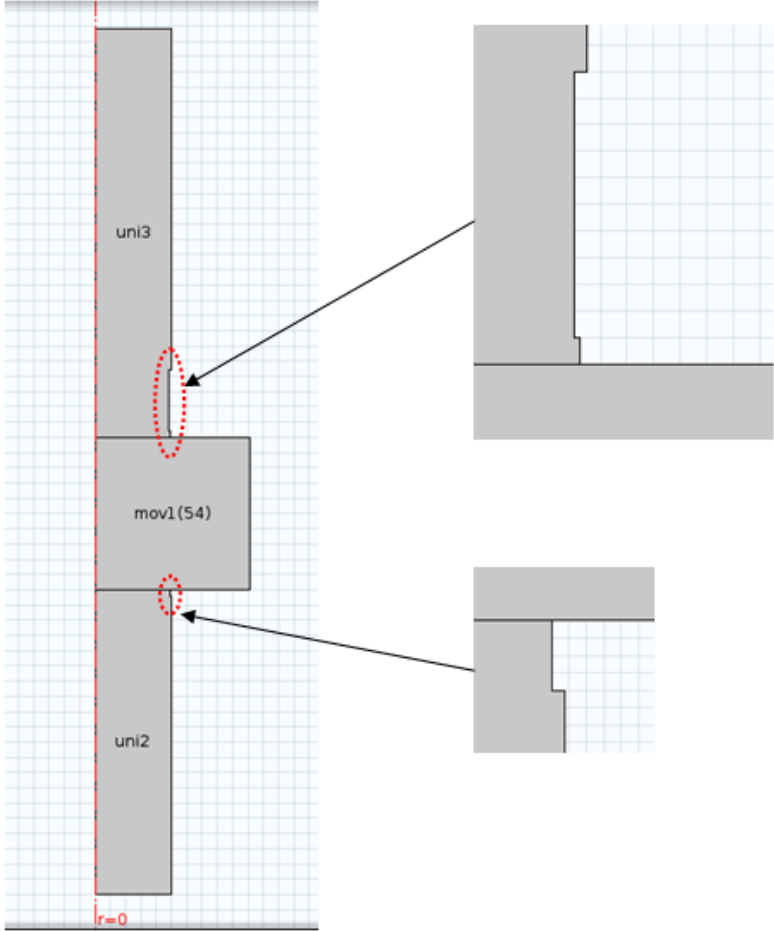
Figure.52 Modelling geometry of 101 mm filter holder apparatus.

The mesh used in the FEM model is shown in *Figure.53*.
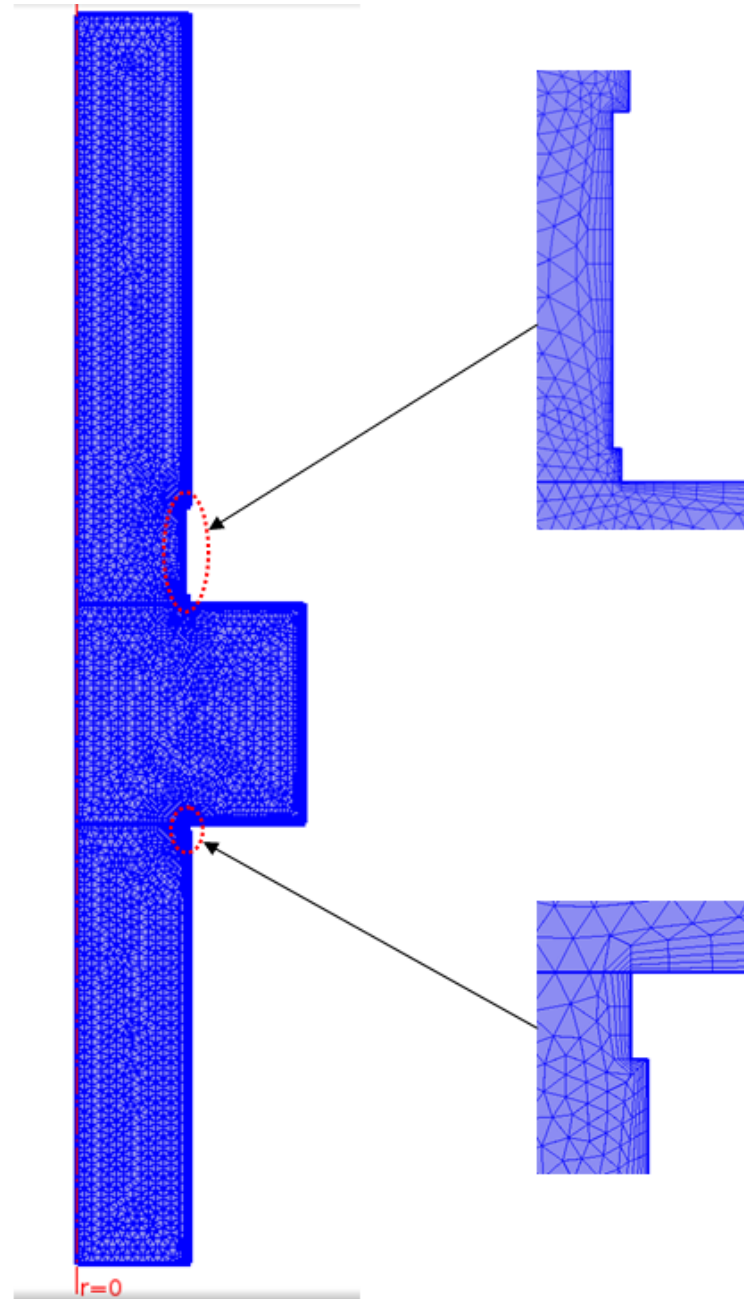
Figure.53 Modelling mesh used for the 101 mm filter apparatus.

Figure.54 and ***Figure.55*** shows the flow fields and the pressure gradient for the 101 *mm* diameter filter apparatus at 7 *°C* and 0.7 *m/s* inlet water velocity. The filter properties used here are those of the 20-50 ppi's.
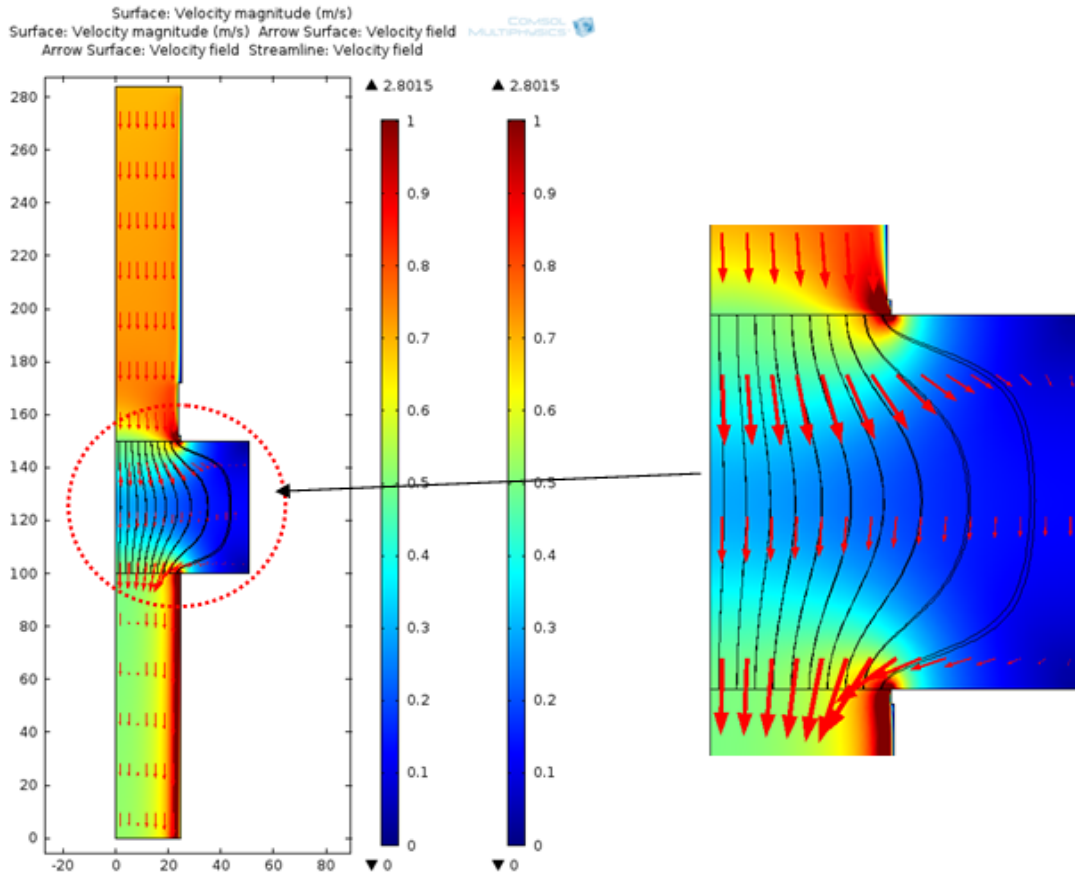
Figure.54 The flow field for the 101 mm diameter filter apparatus. The inlet velocity is 0.7 m/s, filter number is 20-50 ppi.
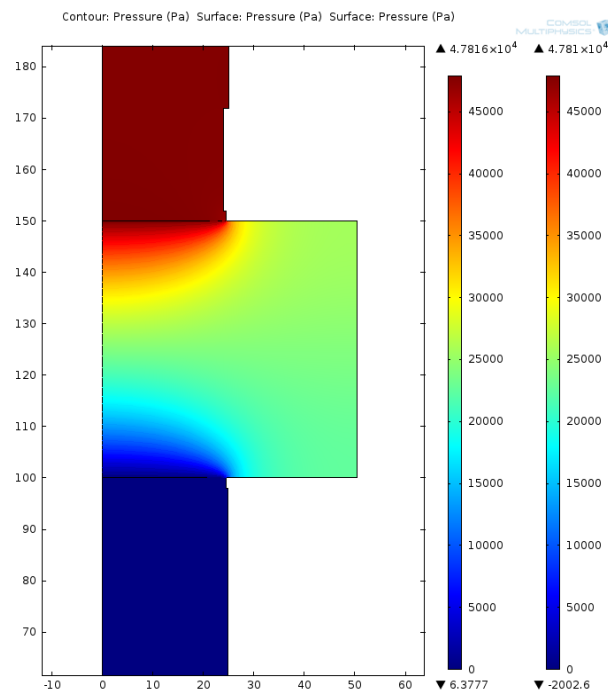
Figure.55 The pressure gradient for the 101 mm diameter filter apparatus. The inlet velocity is 0.7 m/s, filter number is 20-50 ppi.

5.4 Comparison of CFD Results with Experimental Data

The experimental data obtained from tests 26-28 are compared here with the results from CFD modelling. The details of the comparison are shown in **Tables 29 through 31** in the Appendix. *Figure.56* shows CFD results for tests 26-28, compared against the experimental pressure gradients. The average error is ~1.74%
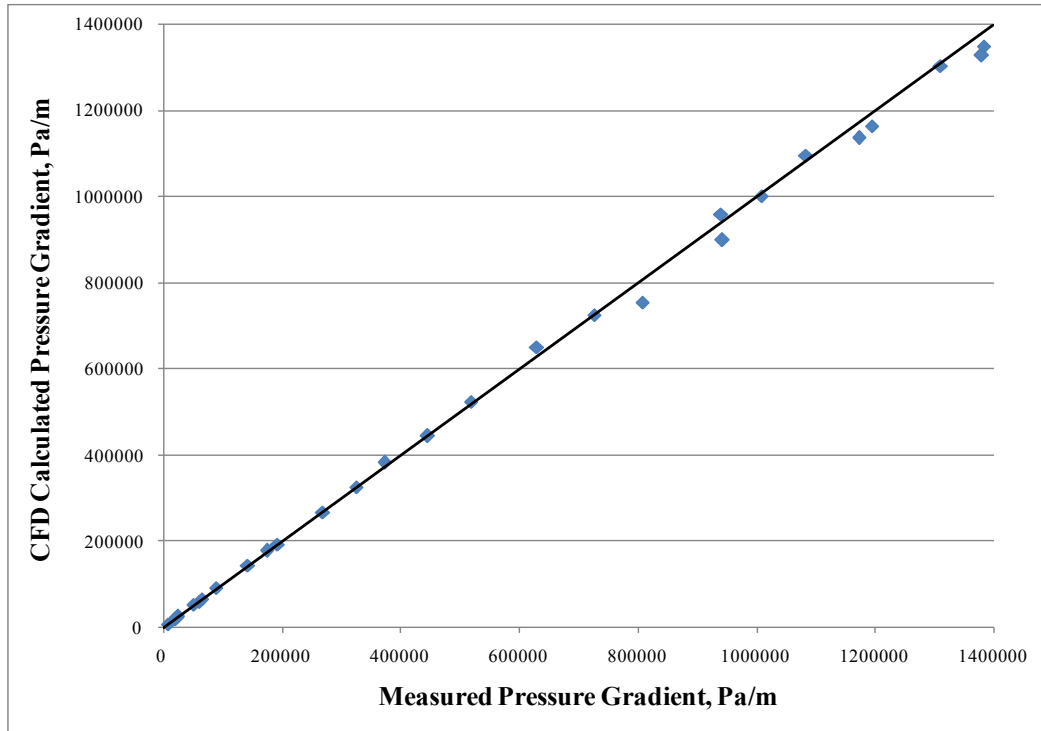
Figure.56 CFD calculated pressure gradients compared against the measured pressure gradients for test 26-28.

From *Figure.56*, it can be found that the CFD modelling results are almost identical with the experimental values. It is important to note, that if significant bypassing had occurred during these experiments, it would not have been possible to achieve agreement between the CFD model and the experimental data for the 49 *mm* filter design, i.e. it would have been necessary to add a 'bypass' channel of finite thickness. The close agreement between experimental and CFD results is thus taken as confirmation that the wall sealing arrangements were in fact of negligible permeability.

For the 101 *mm* filter experiments, the final 'effective' flow field diameters for use with Equation (2) obtained by the CFD modelling were: 65.5 *mm*, 66 *mm*, 66.1 *mm* and 66.5 *mm* for the 30 ppi, 40 ppi, 50 ppi and 80 ppi respectively.

Figure.57 shows the CFD results for test 9 and 23 through 25, compared against the experimental pressure gradients. The average error is about 2.24%. The detailed information

for the comparison of the CFD results and experimental data are shown in **Tables 32 through 35** in the Appendix.
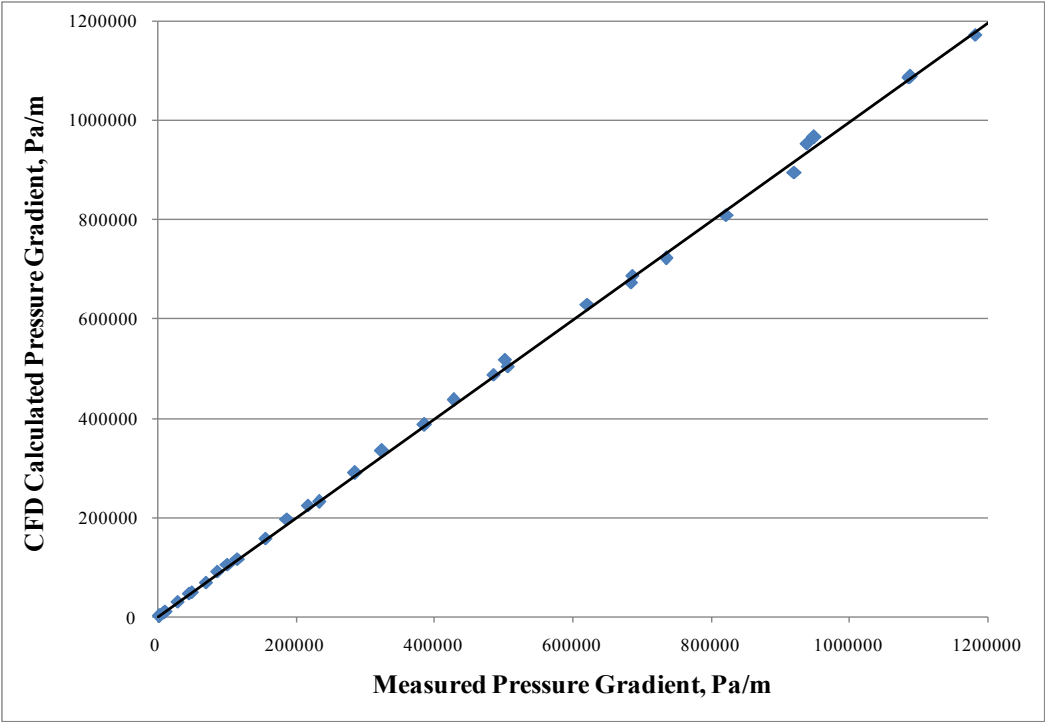
Figure.57 CFD calculated pressure gradient compared against the measured pressure gradient for test 9, and 23 through 25.

The 22-30 ppi, 23-50 ppi and 24-80 ppi filters were cut from the centre of the 18-30 ppi, 20-50 ppi and 21-80 ppi filters. *Figure.58* shows the comparison of test 9 and 27. The superficial velocity values for test 9 were calculated using the 'effective' flow field diameter determined by the CFD modelling.
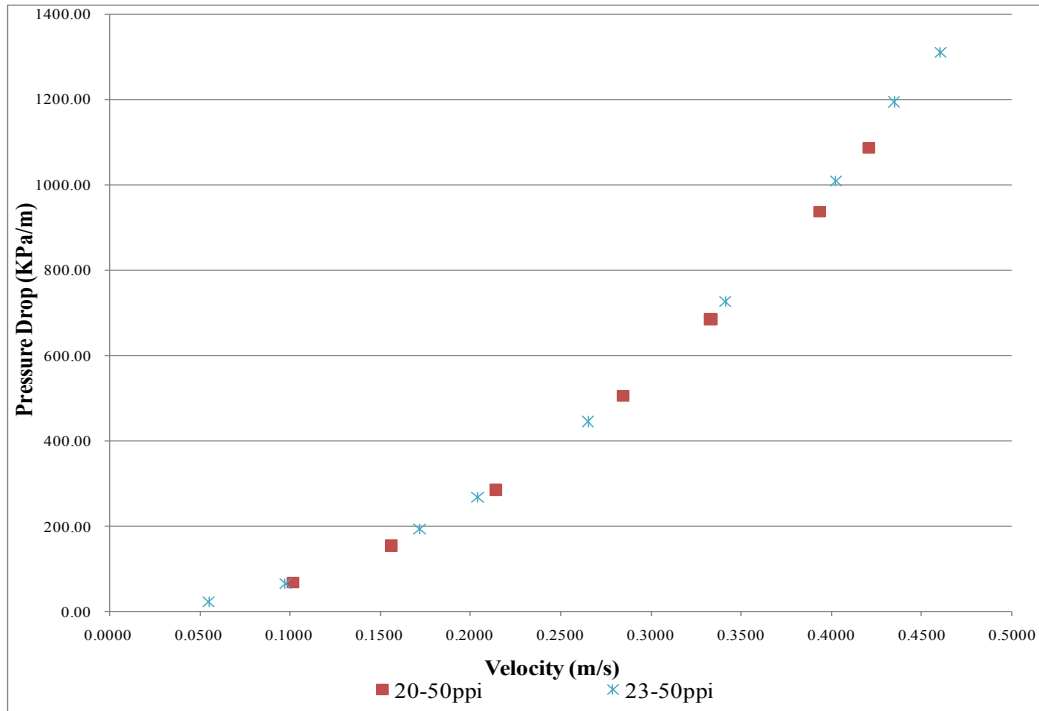
Figure.58 Comparison between the 101 mm and 49 mm filter results.

The regressions are:

20-50 ppi: $y = 5917160.66x^2 + 83380x, R^2 = 0.99995$ (78)

23-50 ppi: $y = 6036686.76x^2 + 87890x, R^2 = 0.99998$ (79)

From ***Figure.58***, Equation (78) and Equation (79), it can be found that the results obtained by these two experiments are nearly identical. In the 'expanding flow field' 101 *mm* apparatus design, the side wall is a stagnant region and bypassing is low (80 ppi) to negligible (30-50 ppi) even in the absence of sealing, as shown in ***Figure.54***. With proper wall sealing (Method 2 using grease and paper), it can be assumed that bypassing in the 101 *mm* design is always negligible. Since there is nearly no bypassing for 101 *mm* filters, the agreement shown in ***Figure.58***, indicates that nearly no bypassing occurred during the 49 *mm* filter experiments as well.

71

Chapter 6

Conclusions

The bypassing during the experiments affects the final results to a critical extent. Only the well-sealed procedure gave meaningful pressure gradients. Two ways were found to avoid bypassing in this study. The first one is use cellulose and silicon grease packed filters, as shown in *Figure. 16*. A second choice is to use filters with a larger size than the inlet and outlet pipes; however, in this case CFD modelling is necessary to compute the 'effective' flow field diameter in order to obtain the real relationship between fluid velocity and the measured pressure gradients.

Different methods of calculating k_1 and k_2 in Equation (2) can give quite different answers. The 'Method 3' was found to give the most physically meaningful mathematical results in this study, i.e. the iterative procedure to first guess k_1 and then correlate the remainder for k_2 using an exponential regression.

It was established that the porosities of the filters decrease consistently with increasing number of ppi, and that when the velocity increased the pressure drop increased even faster with CFF's of higher nominal pore count (e.g. for 80 vs. 30 ppi).

Forchheimer's equation (2) was found to adequately describe the pressure drop for the CFFs used in this study. Both k_1 and k_2 values vary inversely to filter ppi. The filters with lower ppi proved to have lower tortuosities, which in agreement with literature

By testing different filters with the same ppi, it was found that every filter has a slightly different k_1 and k_2 value. Even the filter sections cut from the same filter do not give exactly the same k_1 and k_2 values. Thus there is no specific permeability for each type of filters, only a range and a standard deviation can be obtained.

After modifying the Forchheimer and Ergun equations, Equation (39) was obtained. This equation works well to predicate the pressure gradients in SIVEX$^{®}$ filters. The average absolute error is only 10.7 %.

It was also established that the permeability of a CFF does not change by the changing of fluid flow direction (at least for an incompressible fluid like water or aluminium).

The COMSOL® 2 D axial symmetric CFD model was used in this study to verify the experimental methods. Comparing the CFD results with the experimental data, shows a maximum error of only about 6.5%. It can be concluded that COMSOL® can be accurately used to obtain filter permeability's using the 'expanding flow field' design and can accurately simulate results for either type of apparatus, once the correct k_1 and k_2 values have been determined and programmed.

Chapter 7

Further Work

It is recommended that additional experiments should be executed to explore the change of pressure drop with the filter thickness. This would provide further validation that wall bypassing has been prevented by the current experimental procedure and also help to determine if the filter material is truly isotropic, for example: "Does the original outer surface (top and bottom) possess a different permeability than the balance of the filter?"

Additional experiments should be conducted with filters produced from different suppliers and with the same range of ppi to validate the correlation obtained by this study, or find a more universal correlation suitable for all filters.

Additional experiments could be conducted with a low range, 0-0.1 *Bar* pressure transducer, at low velocity (0-0.05 *m/s*), in order to study the Darcy and transitional regions in the greater detail.

References

1 L.S. Aubrey and R. Schmahl: *Application of Reticulated Silicon Carbide Foam Filters for Iron Casting Applications*, Foundry Trade J., September, 1991, 769-773.

2 L.S. Aubrey and J.E. Dore: *Ceramic Foam- A Deep Bed or Caking Filter in Aluminium Cast Shop Operations,* Light Metals, 1993, 1009-1020.

3 W.H. Sutton, J.C. Palmer, and J.C. Morris: *Development of Ceramic Foam Materials for Filtering High Temperature Alloys*, AFS Trans, 1985, vol. 51, 339-346.

4 R.W. Gairing and M. Cummings: *Operational Experience Using Inclusion Filtration Technology for Continuously Cast Steels Iron*, Stell Maker, vol. 20, 1993, 55-58.

5 M. D. M. Innocentini, P. Sepulveda and F. S. Ortega, In: *Scheffler M Colombo P (eds) Cellular ceramics: structure, manufacturing, properties and application*, Wiley-VCH Verlag GmbH, Weinheim, Germany, 2005, 313.

6 V. P. Rodrigues, L. P. Argiona, R. G. Pilegggi, R. C. Romano, J. R. Coury and M. D. M. Innocentini: *Permeability Optimization of Hot Aerosol Filters Prepared from Foaming of Ceramic Suspensions*. In: 10th International Conference and Exhibition of the European Ceramic Society, Berlin-Alemanha, 2007.

7 N. L. Freitas, J. A. S. Goncalves, M. D. M. Innocentini and J. R. Coury: *Development of a Double-Layered Ceramic Filter for Aerosol Filtration at High-Temperatures: The Filter Collection Efficiency*, Journal of Hazard Mater, Volume 136, Issue 3, 2006, 746-756.

8 V. W. Wang, G. J. Mako and A. L. Matthews: *Pressed Cellular Filter Application in an Aluminum Foundry*, AFS Transact., 1996, 1045-1052.

9 F.A. Acosta G, A.H. Castillejos E., J.M. Almanza R., and A. Flores V: *Analysis of Liquid Flow through Ceramic Porous Media Used for Molten Metal Filtration*, vol. 26B, 1995, 159-171.

10 P. Sandford and S.R. Sibley: *Optimization of Al Casting Productivity Using Foam Filter Technology and Application*, AFS Transact, 1996, 1063-1068.

11 www.lanik.cz, accessed 26.09.2011.

12 A. Montillet, J. Comiti, and J. Legrand: *Determination of Structural Parameters of Metallic Foams from Permeametry Measurements*, J. Mater. Sci., 27, 1992, 4460-4464.

13 M.D.M. Innocentini, P. Sepulveda, V.R. Salvini, J.R. Coury, and V.C. Pandolfelli: *Permeability and Structure of Cellular Ceramics: A Comparison between Two Preparation Techniques*, J. Am. Ceram. Soc., vol. 81, 1998, 3349-52.

14 Martyn V. Twigg and James T. Richardson: *Fundamentals and Applications of Structured Ceramic Foam Catalysts*, Ind. Eng. Chem. Res. vol. 46, 2007, 4166-4177.

15 L.J. Gibson and M.F. Ashby: *Cellular Solids, Structure and Properties*; Pergamon Press: Oxford, U.K., 1988.

16 L.J. Gibson and M.F. Ashby: *Cellular Solids, Structure and Properties*, Second Edition; University of Cambridge Press: Cambridge, U.K., 1999.

17 R. Viskanta, in: J.R. Lloyd, Y. Kurosaki (Eds.): *Enhancement of Heat Transfer in Industrial Combustion Systems: Problems and Future Challenges*, Proceedings of the 3rd ASME/JSME, New York, 1991, 163-173.

18 F. Anderson: *Heat Transport Model for Fibre* Burners, Prog. Energy Combust. sci. 1992 , vol. 18, 1-12.

19 S.B. Bhaduri: *Science and Technology of Ceramic Foams*. Adv. Perform. Mater. vol. 1, 1994, 205-220.

20 T.B. Sweeting, D.A. Norris, L.A. Storm and J.R. Morris: *Reticulated Ceramics for Catalyst Support Applications*. Mater Res. Soc. Symp. Proc. 1995, 309-314.

21 V. W. Wang, G. J. Mako and A. L. Matthews: *Pressed Cellular Filter Application in an Aluminum Foundry*, AFS Transact., 1996, 1045-1052.

22 R. Fritzsch: *Filtration of Aluminium Melts using CF-filters with Electromagnetic Field*, Trondheim: s.n., 2010 .

23 S. Ray, B. Milligan and N. Keegan: *Measurement of Filtration Performance, Filtration Theory and Practical Applications of Ceramic Foam Filters*, Aluminium Cast House Technology, 2005, 1-12.

24 J.T. Richardson, Y. Peng and D. Remue: *Properties of Ceramic Foam Catalyst Supports: Pressure Drop*, Applied Catalysis A: General 204, 2000, 19-32.

25 S.F. Ray: *Recent Improvements in the Measurement and Control of Ceramic Foam Filter Quality*, Presented at the International Melt Quality Workshop, Spain, 2001.

26 Mark W. Kennedy: Detailed PhD plan 2010, Department of Materials Science and Engineering, NTNU, Trondheim, 2010.

27 P. Sandford and S.R. Sibley: *Optimization of Al Casting Productivity Using Foam Filter Technology and Application*, AFS Transact, 1996, 1063-1068.

28 E.A. Moreira and J.R. Coury: *The Influence of Structural Parameters on the Permeability of Ceramic Foam*, Brazilian Journal of Chemical Engineering, vol.21, n. 01, 2004, 23-33.

29 L. Zhang and L.N.W. Damoah: *Removal of Inclusion Rom Aluminium through Filtration*, ASM International, 2010.

30 Jintai, J. Alumina ceramic foam Filter (CFF-Al). Special Material Co. Ltd., 2011.

31 A. Montillet, J. Comiti, and J. Legrand: *Determination of Structural Parameters of Metallic Foams from Permeametry Measurements*, J. Mater. Sci., vol. 27, 1992, 4460-4464.

32 M.D.M. Innocentini, P. Sepulveda, V.R. Salvini, J.R. Coury, and V.C. Pandolfelli: *Permeability and Structure of Cellular Ceramics: A Comparison between Two Preparation Techniques*, J. Am. Ceram. Soc., 1998, 3349-3352.

33 Henry Darcy: *Les Fontaines Publiques de la Ville de Dijon*, Victor Dalmont, Paris, 1856, 647.

34 M.D.M. Innocentini, V.R. Salvini, V.C. Pandolfelli, and J.R. Coury: A*ssessment of Forchheimer's Equation to Predict the Permeability of Ceramic Foams*, J. Am. Ceram. Soc. vol. 82, 1999, 1945-1948.

35 S. Liu, A. Afacan and J.H.Masliyah: *Steady Incompressible Laminar Flow in Porous Media*, Chem. Eng. Science, vol. 49, 1994, 3565-3586.

36 P. Forchheimer: *Wasserbewegungdurch Boden*, Z. Ver. Deutsch. Ing. vol. 45, 1901, 1782-1788.

37 D. Ruth and H. Ma: *On the Derivation of the Forchheimer Equation by Means of the Averaging Theorem*, Transp. Porous Media, vol. 7, 1992, 255-64.

38 S. Ergun: *Flow through Packed Columns*, Chem. Eng. Progress., 1952, vol. 48, n. 2, 89-94.

39 A. P. Philipse, H. L. Schram: *Non- Darcian Airflow through Ceramic Foams*, J. Am. Cer. Soc., vol. 74, n. 4, 1991, 728-732.

40 M. V. Twigg, J. T. Richardson: *Preparation and Properties of Ceramic Foam Catalyst Supports*, Studies in Surface Science and Catalysis, vol. 91, 1995, 345-359.

41 M. D. M. Innocentini, V. R. Salvini, V. C. Pandolfelli and A. Macedo: *Prdiction of Ceramic Foams Permeability Using Ergun's Equation*, Material Research., vol.2 n. 4, Sao Carlos, 1999, 283-289.

42 E. Maire, P. Colombo, J. Adrien, L. Babout and L. Biasetto: *Characterization of the Morphology of Cell Ceramics by 3D Image Processing of X-ray Tomography,* Journal of the European Ceramic Society, vol. 27, issue 4, 2007, 1973-1987.

43 B. Dietrich, W. Schabel, M. Kind, and H. Martin: *Pressure Drop Measurements of Ceramic Sponges-Determining the Hydraulic Diameter*, Chemical Engineering Science, vol. 64, 2009, 3633-3640.

44 B. Dietrich: *Pressure Drop Correlation for Ceramic and Metal Sponges*, Chemical Engineering Science, vol. 74, 2012, 192-199.

45 S. A. Shakiba, R. Ebrahimi and M. Shams: *Experimental Investigation of Pressure Drop through Ceramic Foams: An Empirical Model for Hot and Cold Flo*w, Journal of Fluids Engineering, vol. 133, 2011,.

46 D. Edouard, M. Lacroix, C.P. Huu and F. Luck: *Pressure Drop Modelling on Solid Foam: State-of-the Art Correlation*, Chemical Engineering Journal, vol. 144, 2008, 299-311.

47 V.L. Streeter and E.B. Wylie: *Fluid Mechanics*, McGraw-Hill Ryerson, 1981, ISBN 0-07-548015-8, 8-10.

48 S. Keith: *Mechanics (Third ed.)*, Addison-Wesley, 1971, ISBN 0-201-07392-7.

49 http://en.wikipedia.org/wiki/Viscosity#Types_of_visitscoy, accessed 13.04.2012.

50 http://en.wikipedia.org/wiki/Reynolds_number#cite_note-NASA-4, accessed 13.04.2012.

51 S. George: *On the Effect of the Internal Friction of Fluids on the Motion of Pendulums*, Transactions of the Cambridge Philosophical Society 9, 1851, 8–106.

52 O. Reynolds: *An Experimental Investigation of the Circumstances which Determine whether the Motion of Water shall be Direct or Sinuous, and of the Law of Resistance in Parallel Channels*, Philosophical Transactions of the Royal Society 174 (0),1883, 935–982

53 http://www.engineeringtoolbox.com/reynolds-number-d_237.html, accessed 15.04.2012

54 J.P. Holman: *Heat Transfer*, McGraw-Hill, 2002, 207.

55 http://www.engineeringtoolbox.com/laminar-transitional-turbulent-flow-d_577.html, accessed 15.04.2012

56 L.F. Moody: *Friction Factors for Pipe Flow*, Transactions of the A.S.M.E, 1944, 671-684.

57 http://www.howequipmentworks.com/physics/fluids/flow/flow.html, accessed 16.04.2012.

58 http://www.engineeringtoolbox.com/entrance-length-flow-d_615.html, accessed 16.04.2012.

59 F.M. White: *Fluid Mechanics (Fourth Edition)*, McGraw-Hill, 2010, ISBN 0073529346, 330-331.

60 W. Zhi-qing: *Study on Correction Coefficients of Liminar and Turbulent Entrance Region Effect in Round Pipe*, Applied Mathematics and Mechanics, vol. 3, 1982, 433-446.

61 Z.Q. Wang: *Study on Correction Coefficients of Liminar and Turbulent Entrance Region Effect in Round Pipe*, Applied Mathematics and Mechanics (English Edition, vol. 4, n. 3, 1982, 434-446.

62 M. Matyka, A. Khalili and Z. Koza: *Tortuosity-porosity Relation in the Porous Media Flow*, Phys. Rev. E, vol. 78, 2008.

63 P. Habisreuther, N. Djordjevic and N. Zaralis: *Statistical Distribution of Residence Time and Tortuosity of Flow through Open-cell Foams*, Chemical Engineering Science, vol. 64, 2009, 4943-4954.

64 G.S. Armatas: *Determination of the Effects of the Pore Size Distribution and Pore Connectivity Distribution on the Pore Tortuosity and Diffusive Transport in Mode Porous Networks*, Chemical Engineering Science, vol. 61, 4662-4675.

65 A. Scheidegger: *The Physics of Flow through Porous Media*, University of Toronto, Toronto, 1974.

66 M.W. Kennedy, K. Zhang, R. Fritzitch, S. Akhtar, J.A. Bakken and R.E. Aune: *Characterization of Ceramic Foam Filters used for Liquid Metal Filtration*, to be submitted to Metallurgical Transactions B, 2012, 1-46.

67 P.D. Desai, H.M. James, and C.Y. Ho: *Electrical Resistivity of Aluminum and Magnanese*, Journal of Physical and Chemical Reference Data, vol. 13, n. 4, 1984, 1131-1172.

68 http://www.henrys.com/61271-EPSON-PERFECTION-V330-PHOTO-FLATBED.aspx, accessed 10.07.2012.

69   http://en.wikipedia.org/wiki/Energy-dispersive_X-ray_spectroscopy, accessed 10.10.2011.

70 J.P. Anson, R.A.L. Drew and J.E. Gruzleski: *The Surface Tension of Molten Aluminum and Al-Si-Mg Alloy under Vacuum and Hydrogen Atmospheres*, Metallurgical and Meterials Transacitions B, vol. 30B, 1999, 1027-1032.

71 D. Wang and R.A. Overfelt: *Oscillating Cup Viscosity Measurements of Aluminum Alloys: A201, A319 and A356*, International Jouranal of Thermophysics, vol. 23, n. 4, 2002, 1063-1076.

72 V. Sarou-Kanlan, F. Millot and J.C. Rifflet: *Surface Density of Oxygen-Free Liquid Aluminum at High Temperature*, International Journal of Thermophysics, vol. 24, no. 1, 2003, 277-286.

73 J. Huang, T. Mori and J.G. Conley: *Simulation of Microporosity Formation in Modified and Unmodified A356 Alloy Castings*, Metallugical and Materials Transactions B, vol. 29B, 1998, 1249-1260.

74 M. W. Kennedy, S. Akhtar, J. A. Bakken, and R. E. Aune: *Effect of Electromagnetic Force on the Distribution of Inclusions from Liquid Aluminum by a Ceramic Foam Filter in Continuous Filtration Tests*, submitted to Metallurgical and Materials Transactions B, 2012.

75 M. W. Kennedy, S. Akhtar, J. A. Bakken, and R. E. Aune: *Electromagnetically Enhanced Filtration of Aluminum Melts*, TMS Light Metals 2011, San Diego, California, 2011.

76 R. Fritzsch, M. W. Kennedy, S. Akhtar, J. A. Bakken, and R. E. Aune: *Electromagnetically Modified Filtration of Liquid Aluminium with a Ceramic Foam Filter*, to be presented at the Electromagnetic Processing of Materials, Beijing, China, 2012, 763-768.

77 http://en.wikipedia.org/wiki/Porosity, accessed 19.04.2012.

78 J. Große, B. Dietrich, H. Martin, M. Kind, J. Vicente, and E. H. Hardy: *Chemical Engineering & Technology*, vol. 31, 2008, 307-314.

79 B. Dietrich, G. I. Garrido, P. Habisreuther, N. Zarzalis, H. Martin, M. Kind, and B. Kraushaar-Czarnetzki: *Morphological Characterization of Ceramic Sponges for Applications in Chemical Engineering*, Industrial & Engineering Chemistry Research, vol. 48, 2009, 10395-10401.

80 N. Keegan, W. Schneider, and H. Krug: *Evaluation of the Efficiency of Fine Pore Ceramic Foam Filters*, TMS Light Metals, San Diego, 1999, 1-10.

81 S. Ergun and A.A. Orning: *Fluid Flow through Randomly Packed Columns and Fluidized Beds*, Industrial &Engineering Chemistry, vol. 41, 1949, 1179-1184.

82 E. Moreira, M. Innocentini, and J. Coury: *Permeability of Ceramic Foams to Compressible and Incompressible Flow*, Journal of the European Ceramic Society, vol. 24, 2004, 3209-3218.

83 G. Diedericks and J. Du Plessis: *Electrical Conduction and Formation Factor in Isotropic Porous Media*, Advances in water resources, vol. 19, 1996, 225-239.

84 COMSOL Multiphysics 4.2a documentation.

85 http://en.wikipedia.org/wiki/Navier%E2%80%93Stokes_equations#cite_ref-Ach_14-0, accessed 30.06.2012

86 D.C. Wilcox: T*urbulence Modelling for CFD*, 2nd ed., DCW Industries, 1998.

87 K. Abe, T. Kondoh, and Y. Nagano: *A New Turbulence Model for Predicting Fluid Flow and Heat Transfer in Separating and Reattaching Flows—I. Flow Field Calculations*, International Journal of Heat and Mass Transfer, vol. 37, no. 1, 1994, 139-151.

Appendix

Table 1 Test 1 2-30 ppi, Diameter: 48.57 *mm*, Thickness: 50.18 *mm*

Velocity (m/s)	Pressure Drop (Pa/m)	Temperature (^{o}C)	Density (kg/m^3)	Viscosity (kg/m.s)
0.029	2982	6.4	1000.0	1.401E-03
0.009	823	6.7	999.9	1.388E-03
0.063	12241	7.0	999.9	1.377E-03
0.016	1598	7.3	999.9	1.367E-03
0.084	20299	7.5	999.9	1.358E-03
0.133	46710	7.7	999.9	1.352E-03
0.250	155893	7.8	999.9	1.348E-03
0.334	273426	7.9	999.9	1.344E-03
0.438	493635	7.9	999.9	1.342E-03
0.550	683574	8.6	999.8	1.316E-03
0.654	942796	8.9	999.8	1.307E-03
0.691	1071006	9.0	999.8	1.304E-03
0.425	403214	9.0	999.8	1.302E-03
0.285	191152	9.1	999.8	1.298E-03

Table 2 Test 2 15-80 ppi, Diameter: 48.97 *mm*, Thickness: 49.77 *mm*

Velocity (m/s)	Pressure Drop (Pa/m)	Temperature (^{o}C)	Density (kg/m^3)	Viscosity (kg/m.s)
0.005	1067	6.9	999.9	1.383E-03
0.022	6091	7.3	999.9	1.367E-03
0.042	15132	7.5	999.9	1.357E-03
0.068	35601	7.8	999.9	1.345E-03
0.094	63438	8.1	999.9	1.336E-03
0.116	95251	8.3	999.9	1.328E-03
0.154	165072	8.4	999.9	1.324E-03
0.218	323551	8.6	999.8	1.318E-03
0.271	488434	8.7	999.8	1.314E-03
0.303	614326	8.9	999.8	1.307E-03
0.356	795660	9.0	999.8	1.303E-03
0.392	893485	9.2	999.8	1.296E-03
0.433	988171	9.5	999.8	1.284E-03
0.482	1123292	9.8	999.7	1.275E-03
0.526	1251507	9.9	999.7	1.270E-03
0.012	3893	10.2	999.7	1.261E-03
0.047	16451	10.4	999.7	1.253E-03
0.083	39055	10.5	999.7	1.248E-03
0.133	85937	10.6	999.7	1.247E-03
0.207	202557	10.7	999.7	1.242E-03

Table 3 Test 3 14-80 ppi, Diameter: 48.82 *mm*, Thickness: 50.44 *mm*

Velocity (m/s)	Pressure Drop (Pa/m)	Temperature (^{o}C)	Density (kg/m^3)	Viscosity (kg/m.s)
0.004	2145	6.6	999.9	1.392E-03
0.030	10046	7.1	999.9	1.374E-03
0.080	38283	7.4	999.9	1.363E-03
0.121	80527	7.6	999.9	1.354E-03
0.150	124960	7.8	999.9	1.345E-03
0.199	220398	8.1	999.9	1.337E-03
0.250	333215	8.2	999.9	1.332E-03
0.304	468173	8.4	999.9	1.325E-03
0.355	597009	8.5	999.8	1.320E-03
0.400	692701	8.7	999.8	1.314E-03
0.458	800349	8.8	999.8	1.308E-03
0.511	937777	9.0	999.8	1.302E-03
0.564	1049960	9.2	999.8	1.297E-03
0.609	1132377	9.2	999.8	1.294E-03
0.634	1145321	9.4	999.8	1.286E-03
0.334	334509	9.6	999.8	1.282E-03
0.189	116546	9.7	999.8	1.278E-03
0.072	21478	9.8	999.7	1.273E-03

Table 4 Test 4 2-30 ppi, Diameter: 48.57 *mm*, Thickness: 50.18 *mm*

Velocity (m/s)	Pressure Drop (Pa/m)	Temperature (^{o}C)	Density (kg/m^3)	Viscosity (kg/m.s)
0.684	1092146	6.0	1000.0	1.419E-03
0.048	7335	6.3	1000.0	1.407E-03
0.099	26821	6.5	999.9	1.396E-03
0.204	109275	6.7	999.9	1.389E-03
0.290	203839	7.1	999.9	1.373E-03
0.405	385956	7.5	999.9	1.358E-03
0.498	587554	7.7	999.9	1.350E-03
0.592	805953	8.0	999.9	1.338E-03
0.645	974158	8.2	999.9	1.332E-03

Table 5 Test 5 15-80 ppi, Diameter: 48.97 *mm*, Thickness: 49.77 *mm*

Velocity (m/s)	Pressure Drop (Pa/m)	Temperature (^{o}C)	Density (kg/m^3)	Viscosity (kg/m.s)
0.311	1179700	6.9	999.9	1.381E-03
0.335	1360744	7.3	999.9	1.364E-03
0.297	1069497	7.4	999.9	1.361E-03
0.253	782618	7.6	999.9	1.354E-03
0.193	468132	7.7	999.9	1.350E-03
0.153	299258	7.9	999.9	1.342E-03
0.102	139445	8.0	999.9	1.338E-03
0.074	76229	8.2	999.9	1.331E-03
0.034	20471	8.4	999.9	1.324E-03

Table 6 Test 6 14-80 ppi, Diameter: 48.82 *mm*, Thickness: 50.44 *mm*

Velocity (m/s)	Pressure Drop (Pa/m)	Temperature (°C)	Density (kg/m³)	Viscosity (kg/m.s)
0.378	1305519	5.7	1000.0	1.431E-03
0.343	1078644	5.9	1000.0	1.421E-03
0.288	774394	6.1	1000.0	1.413E-03
0.246	570100	6.3	1000.0	1.404E-03
0.199	379939	6.5	1000.0	1.398E-03
0.135	181663	6.7	999.9	1.390E-03
0.084	75497	7.0	999.9	1.379E-03
0.033	16655	7.2	999.9	1.370E-03

Table 7 Test 7 4-50 ppi, Diameter: 48.61 *mm*, Thickness: 50.60 *mm*

Velocity (m/s)	Pressure Drop (Pa/m)	Temperature (°C)	Density (kg/m³)	Viscosity (kg/m.s)
0.405	877748	6.3	1000.0	1.407E-03
0.043	13810	6.7	999.9	1.391E-03
0.118	78056	6.8	999.9	1.384E-03
0.211	242931	7.0	999.9	1.379E-03
0.285	443618	7.1	999.9	1.374E-03
0.361	692108	7.3	999.9	1.367E-03
0.483	1248950	7.5	999.9	1.360E-03

Table8 Test 8 4-50 ppi, Diameter: 48.61 *mm*, Thickness: 50.60 *mm*

Velocity (m/s)	Pressure Drop (Pa/m)	Temperature (°C)	Density (kg/m³)	Viscosity (kg/m.s)
0.449	1028147	4.5	1000.0	1.483E-03
0.055	18831	5.1	1000.0	1.455E-03
0.152	123763	5.5	1000.0	1.439E-03
0.224	257183	5.7	1000.0	1.430E-03
0.299	474541	5.9	1000.0	1.424E-03
0.370	698184	6.3	1000.0	1.406E-03
0.491	1240875	6.5	1000.0	1.399E-03

Table 9 Test 9 18-50 ppi, Diameter: ~101 *mm*, Thickness: 49.58 *mm*

Velocity (m/s)	Pressure Drop (Pa/m)	Temperature (°C)	Density (kg/m³)	Viscosity (kg/m.s)
0.393	937588	5.1	1000.0	1.454E-03
0.102	69810	5.5	1000.0	1.437E-03
0.156	156059	5.6	1000.0	1.432E-03
0.214	286174	5.8	1000.0	1.425E-03
0.284	505716	5.9	1000.0	1.421E-03
0.333	685889	6.2	1000.0	1.411E-03
0.420	1085478	6.4	1000.0	1.403E-03

Table10 Test 10 18-50 ppi, Diameter: ~101 *mm*, Thickness: 49.58 *mm*

Velocity (m/s)	Pressure Drop (Pa/m)	Temperature (^{o}C)	Density (kg/m^3)	Viscosity (kg/m.s)
0.366	816673	5.9	1000.0	1.422E-03
0.016	2992	6.2	1000.0	1.409E-03
0.047	15790	6.4	1000.0	1.401E-03
0.125	98103	6.6	999.9	1.391E-03
0.177	197459	6.9	999.9	1.383E-03
0.417	1074903	7.3	999.9	1.367E-03
0.372	864438	7.4	999.9	1.362E-03
0.302	572042	7.5	999.9	1.356E-03
0.242	359909	7.8	999.9	1.347E-03

Table11 Test 11 1-30 ppi, Diameter: 48.71 *mm*, Thickness: 50.48 *mm*

Velocity (m/s)	Pressure Drop (Pa/m)	Temperature (^{o}C)	Density (kg/m^3)	Viscosity (kg/m.s)
0.710	978343	6.5	1000.0	1.398E-03
0.046	5771	6.8	999.9	1.387E-03
0.117	30911	7.0	999.9	1.379E-03
0.218	99618	7.1	999.9	1.373E-03
0.325	215863	7.2	999.9	1.368E-03
0.427	375867	7.7	999.9	1.349E-03
0.523	549073	8.0	999.9	1.341E-03
0.603	690255	8.1	999.9	1.334E-03

Table 12 Test 12 3-50 ppi, Diameter: 48.95 *mm*, Thickness: 50.37 *mm*

Velocity (m/s)	Pressure Drop (Pa/m)	Temperature (^{o}C)	Density (kg/m^3)	Viscosity (kg/m.s)
0.367	776197	5.7	1000.0	1.431E-03
0.022	5233	6.3	1000.0	1.406E-03
0.067	31815	6.4	1000.0	1.400E-03
0.163	171054	6.6	999.9	1.394E-03
0.229	335865	6.7	999.9	1.389E-03
0.283	503703	6.8	999.9	1.387E-03
0.417	1067479	6.9	999.9	1.381E-03
0.469	1247505	7.0	999.9	1.377E-03

Table 13 Test 13 5-50 ppi, Diameter: 48.65 *mm*, Thickness: 50.43 *mm*

Velocity (m/s)	Pressure Drop (Pa/m)	Temperature (^{o}C)	Density (kg/m^3)	Viscosity (kg/m.s)
0.506	1152868	6.4	1000.0	1.401E-03
0.025	5251	6.9	999.9	1.383E-03
0.057	18846	7.1	999.9	1.373E-03
0.127	78605	7.3	999.9	1.366E-03
0.199	185871	7.5	999.9	1.359E-03
0.285	370994	7.6	999.9	1.355E-03
0.379	652171	7.7	999.9	1.349E-03
0.426	834240	7.9	999.9	1.343E-03
0.477	1034413	8.0	999.9	1.339E-03
0.523	1236086	8.2	999.9	1.333E-03

Table 14 Test 14 6-50 ppi, Diameter: 48.86 *mm*, Thickness: 50.56 *mm*

Velocity (m/s)	Pressure Drop (Pa/m)	Temperature (^{o}C)	Density (kg/m^3)	Viscosity (kg/m.s)
0.450	1185370	5.7	1000.0	1.428E-03
0.044	15610	6.1	1000.0	1.414E-03
0.102	67181	6.3	1000.0	1.406E-03
0.185	208637	6.4	1000.0	1.400E-03
0.243	352890	6.6	999.9	1.393E-03
0.298	540831	6.8	999.9	1.385E-03
0.362	766017	7.1	999.9	1.374E-03
0.411	971166	7.2	999.9	1.368E-03
0.467	1263214	7.4	999.9	1.361E-03

Table 15 Test 15 7-50 ppi, Diameter: 48.80 *mm*, Thickness: 50.26 *mm*

Velocity (m/s)	Pressure Drop (Pa/m)	Temperature (^{o}C)	Density (kg/m^3)	Viscosity (kg/m.s)
0.453	1045977	4.8	1000.0	1.468E-03
0.039	10604	5.5	1000.0	1.437E-03
0.112	69538	5.8	1000.0	1.428E-03
0.171	155384	6.0	1000.0	1.419E-03
0.246	317343	6.2	1000.0	1.409E-03
0.314	507861	6.4	1000.0	1.401E-03
0.382	746837	6.6	999.9	1.392E-03
0.507	1239343	6.8	999.9	1.386E-03

Table 16 Test 16 8-50 ppi, Diameter: 49.37 *mm*, Thickness: 50.49 *mm*

Velocity (m/s)	Pressure Drop (Pa/m)	Temperature (^{o}C)	Density (kg/m^3)	Viscosity (kg/m.s)
0.468	1039446	6.4	1000.0	1.403E-03
0.035	7550	6.7	999.9	1.389E-03
0.075	31264	6.9	999.9	1.381E-03
0.143	105264	7.2	999.9	1.370E-03
0.194	188586	7.4	999.9	1.363E-03
0.250	309131	7.5	999.9	1.358E-03
0.315	488208	7.7	999.9	1.352E-03
0.390	735226	7.8	999.9	1.348E-03
0.514	1241277	7.9	999.9	1.341E-03

Table 17 Test 17 11-80 ppi, Diameter: ~48.00 *mm*, Thickness: 50.59 *mm*

Velocity (m/s)	Pressure Drop (Pa/m)	Temperature (^{o}C)	Density (kg/m^3)	Viscosity (kg/m.s)
0.338	1355909	13.1	999.4	1.164E-03
0.317	1197566	13.2	999.4	1.160E-03
0.277	923720	13.3	999.4	1.158E-03
0.242	713898	13.4	999.4	1.155E-03
0.184	436260	13.6	999.3	1.151E-03
0.120	191626	13.7	999.3	1.148E-03
0.080	90628	13.9	999.3	1.141E-03
0.055	45271	14.0	999.3	1.136E-03

Table 18 Test 18 12-80 ppi, Diameter: 48.94 *mm*, Thickness: 50.07 *mm*

Velocity (m/s)	Pressure Drop (Pa/m)	Temperature (^{o}C)	Density (kg/m^3)	Viscosity (kg/m.s)
0.338	1355909	13.1	999.4	1.164E-03
0.317	1197566	13.2	999.4	1.160E-03
0.277	923720	13.3	999.4	1.158E-03
0.242	713898	13.4	999.4	1.155E-03
0.184	436260	13.6	999.3	1.151E-03
0.120	191626	13.7	999.3	1.148E-03
0.080	90628	13.9	999.3	1.141E-03
0.055	45271	14.0	999.3	1.136E-03

Table 19 Test 19 13-50 ppi, Diameter: 49.39 *mm*, Thickness: 49.97 *mm*

Velocity (m/s)	Pressure Drop (Pa/m)	Temperature (^{o}C)	Density (kg/m^3)	Viscosity (kg/m.s)
0.504	1264101	6.3	1000.0	1.406E-03
0.454	1022439	6.5	1000.0	1.399E-03
0.405	804974	6.6	999.9	1.395E-03
0.310	490138	6.7	999.9	1.388E-03
0.262	350434	7.0	999.9	1.379E-03
0.179	166969	7.1	999.9	1.375E-03
0.139	100367	7.3	999.9	1.366E-03
0.034	8313	7.4	999.9	1.361E-03
0.083	39380	7.6	999.9	1.355E-03

Table 20 Test 20 16-80 ppi, Diameter: 48.84 *mm*, Thickness: 50.06 *mm*

Velocity (m/s)	Pressure Drop (Pa/m)	Temperature (^{o}C)	Density (kg/m^3)	Viscosity (kg/m.s)
0.356	926569	7.1	999.9	1.376E-03
0.427	1318887	7.8	999.9	1.345E-03
0.368	1012900	8.1	999.9	1.336E-03
0.330	820307	8.2	999.9	1.332E-03
0.257	504143	8.4	999.9	1.326E-03
0.208	369229	8.4	999.8	1.323E-03
0.156	196134	8.5	999.8	1.320E-03
0.095	84645	8.7	999.8	1.312E-03
0.036	16075	8.7	999.8	1.312E-03

Table 21 Test 21 17-50 ppi, Diameter: 49.12 *mm*, Thickness: 50.41 *mm*

Velocity (m/s)	Pressure Drop (Pa/m)	Temperature (^{o}C)	Density (kg/m^3)	Viscosity (kg/m.s)
0.488	1157648	9.9	999.7	1.271E-03
0.507	1257931	10.4	999.7	1.253E-03
0.434	902559	10.5	999.7	1.248E-03
0.383	700781	10.6	999.7	1.246E-03
0.332	526432	10.7	999.7	1.242E-03
0.276	374688	10.8	999.7	1.239E-03
0.224	247365	10.9	999.6	1.235E-03
0.197	192677	11.0	999.6	1.231E-03
0.140	100579	11.2	999.6	1.227E-03
0.052	15443	11.3	999.6	1.222E-03

Table 22 Test 22 17-50 ppi, Diameter: 49.12 *mm*, Thickness: 50.41 *mm* (opposite direction)

Velocity (m/s)	Pressure Drop (Pa/m)	Temperature (°C)	Density (kg/m³)	Viscosity (kg/m.s)
0.313	491832	9.9	999.7	0.00127
0.246	304892	10.1	999.7	0.00126
0.185	169788	10.3	999.7	0.00126
0.136	95532	10.5	999.7	0.00125
0.083	39229	10.6	999.7	0.00125
0.052	16488	10.8	999.7	0.00124
0.426	866361	11.5	999.6	0.00122
0.366	637771	11.6	999.6	0.00121

Table 23 Test 23 19-30 ppi, Diameter: ~101 *mm*, Thickness: 50.65 *mm*

Velocity (m/s)	Pressure Drop (Pa/m)	Temperature (°C)	Density (kg/m³)	Viscosity (kg/m.s)
0.031	2723	6.6	999.9	1.393E-03
0.074	11712	6.7	999.9	1.389E-03
0.156	50272	6.9	999.9	1.380E-03
0.242	116462	7.1	999.9	1.374E-03
0.343	233955	7.3	999.9	1.368E-03
0.445	386486	7.4	999.9	1.362E-03
0.610	735607	7.6	999.9	1.354E-03

Table 24 Test 24 20-40 ppi, Diameter: ~101 *mm*, Thickness: 47.65 *mm*

Velocity (m/s)	Pressure Drop (Pa/m)	Temperature (°C)	Density (kg/m³)	Viscosity (kg/m.s)
0.408	501847	5.1	1000.0	1.456E-03
0.020	2179	5.5	1000.0	1.436E-03
0.093	28841	5.6	1000.0	1.435E-03
0.167	86720	5.8	1000.0	1.428E-03
0.249	187764	5.9	1000.0	1.421E-03
0.326	324686	6.0	1000.0	1.417E-03
0.396	485160	6.2	1000.0	1.411E-03
0.466	684740	6.2	1000.0	1.410E-03
0.511	822209	6.3	1000.0	1.405E-03
0.539	920699	6.5	1000.0	1.399E-03

Table 25 Test 25 21-80 ppi, Diameter: ~101 *mm*, Thickness: 50.31 *mm*

Velocity (m/s)	Pressure Drop (Pa/m)	Temperature (^{o}C)	Density (kg/m^3)	Viscosity (kg/m.s)
0.295	948953	7.0	999.9	1.378E-03
0.021	9916	7.3	999.9	1.365E-03
0.058	46158	7.5	999.9	1.358E-03
0.091	101936	7.7	999.9	1.352E-03
0.137	217300	7.7	999.9	1.349E-03
0.195	428441	7.8	999.9	1.347E-03
0.236	621747	7.9	999.9	1.342E-03
0.314	1088535	8.0	999.9	1.339E-03
0.326	1181713	8.2	999.9	1.331E-03

Table 26 Test 26 18-50 ppi, Diameter: 49.15 *mm*, Thickness: 49.58 *mm*

Velocity (m/s)	Pressure Drop (Pa/m)	Temperature (^{o}C)	Density (kg/m^3)	Viscosity (kg/m.s)
0.434	1194904	6.3	1000.0	1.404E-03
0.460	1310433	6.6	999.9	1.395E-03
0.402	1008834	6.7	999.9	1.389E-03
0.341	726048	6.8	999.9	1.384E-03
0.265	445758	7.0	999.9	1.378E-03
0.204	268844	7.1	999.9	1.375E-03
0.172	193182	7.2	999.9	1.368E-03
0.097	65509	7.5	999.9	1.360E-03
0.055	23185	7.6	999.9	1.352E-03

Table 27 Test 27 19-30 ppi, Diameter: 48.67 *mm*, Thickness: 50.65 *mm*

Velocity (m/s)	Pressure Drop (Pa/m)	Temperature (^{o}C)	Density (kg/m^3)	Viscosity (kg/m.s)
0.637	807100	7.4	999.9	1.361E-03
0.769	1083791	7.9	999.9	1.343E-03
0.719	940447	8.0	999.9	1.338E-03
0.529	519563	8.2	999.9	1.333E-03
0.416	325407	8.3	999.9	1.329E-03
0.273	142851	8.4	999.9	1.324E-03
0.173	60003	8.6	999.8	1.317E-03
0.110	25014	8.7	999.8	1.314E-03
0.057	7345	8.9	999.8	1.307E-03

Table 28 Test 28 21-80 ppi, Diameter: 49.08 *mm*, Thickness: 50.31 *mm*

Velocity (m/s)	Pressure Drop (Pa/m)	Temperature (°C)	Density (kg/m³)	Viscosity (kg/m.s)
0.380	1379323	5.8	1000.0	1.427E-03
0.384	1382511	5.9	1000.0	1.423E-03
0.351	1172774	6.1	1000.0	1.415E-03
0.311	942852	6.1	1000.0	1.414E-03
0.262	629565	5.9	1000.0	1.423E-03
0.198	372652	6.0	1000.0	1.419E-03
0.131	174497	6.1	1000.0	1.414E-03
0.091	88998	6.2	1000.0	1.409E-03
0.036	19485	6.5	1000.0	1.398E-03
0.066	50886	6.8	999.9	1.385E-03

Table 29 Comparison of Experimental Data and CFD Results for Test 26, 22-30 ppi

Velocity (m/s)	Experiment Pressure Drop (Pa/m)	COMSOL Pressure Drop (Pa/m)	Error %
0.637	807100	754821	6.48
0.769	1083791	1095682	1.10
0.719	940447	959122	1.99
0.529	519563	524132	0.88
0.416	325407	326559	0.35
0.273	142851	143441	0.41
0.173	60003	59490	0.85
0.110	25014	25127	0.45
0.057	7345	7413	0.92

Table 30 Comparison of Experimental Data and CFD Results for Test 27, 23-50 ppi

Superficial Velocity (m/s)	Experiment Pressure Drop (Pa/m)	COMSOL Pressure Drop (Pa/m)	Error %
0.434	1194904	1164648	2.53
0.460	1310433	1302957	0.57
0.402	1008834	1001339	0.74
0.341	726048	726148	0.01
0.265	445758	444351	0.32
0.204	268844	267871	0.36
0.172	193182	192433	0.39
0.097	65509	65689	0.27
0.055	23185	23182	0.01

Table 31 Comparison of Experiment Data and CFD Results for Test 28, 24-80 ppi

Superficial Velocity (m/s)	Experiment Pressure Drop (Pa/m)	COMSOL Pressure Drop (Pa/m)	Error %
0.380	1379323	1327725	3.74
0.384	1382511	1349328	2.40
0.351	1172774	1136270	3.11
0.311	942852	898688	4.68
0.262	629565	649598	3.18
0.198	372652	382152	2.55
0.131	174497	178352	2.21
0.091	88998	91165	2.43
0.036	19485	18744	3.80
0.066	50886	51944	2.08

Table 32 Comparison of Experiment Data and CFD Results for Test 23, 18-30 ppi

Superficial Velocity (m/s)	Experiment Pressure Drop (Pa/m)	COMSOL Pressure Drop (Pa/m)	Error %
0.031	2723	2622	3.74
0.074	11712	12253	4.62
0.156	50272	49979	0.58
0.242	116462	116984	0.45
0.343	233955	231887	0.88
0.445	386486	387781	0.34
0.610	735607	722911	1.73

Table 33 Comparison of Experimental Data and CFD Results for Test 24, 19-40 ppi

Superficial Velocity (m/s)	Experiment Pressure Drop (Pa/m)	COMSOL Pressure Drop (Pa/m)	Error %
0.408	501847	519931	3.60
0.020	2179	2110	3.17
0.093	28841	30466	5.63
0.167	86720	91433	5.44
0.249	187764	197494	5.18
0.326	324686	335006	3.18
0.396	485160	488576	0.70
0.466	684740	674114	1.55
0.511	822209	809295	1.57
0.539	920699	896728	2.60

Table 34 Comparison of Experimental Data and CFD Results for Test 9, 20-50 ppi

Superficial Velocity (m/s)	Experiment Pressure Drop (Pa/m)	COMSOL Pressure Drop (Pa/m)	Error %
0.393	937588	953351	1.68
0.102	69810	70079	0.39
0.156	156059	157832	1.14
0.214	286174	290568	1.54
0.284	505716	504841	0.17
0.333	685889	687470	0.23
0.420	1085478	1086506	0.09

Table 35 Comparison of Experimental Data and CFD Results for Test 25, 21-80 ppi

Superficial Velocity (m/s)	Experiment Pressure Drop (Pa/m)	COMSOL Pressure Drop (Pa/m)	Error %
0.295	948953	966568	1.86
0.021	9916	9539	3.80
0.058	46158	48690	5.49
0.091	101936	106651	4.63
0.137	217300	225474	3.76
0.195	428441	437538	2.12
0.236	621747	629214	1.20
0.314	1088535	1088436	0.01
0.326	1181713	1173106	0.73